A DENSITY FUNCTIONAL THEORY STUDY OF A NICKEL-BASED ANODE CATALYST FOR APPLICATION IN A DIRECT PROPANE FUEL CELL

Shadi Vafaeyan

Thesis Submitted to the
Faculty of Graduate and Postdoctoral Studies
In partial fulfillment of the requirement for the degree of

Doctor of Philosophy

in

Department of Chemical and Biological Engineering
Faculty of Engineering
UNIVERSITY OF OTTAWA

ABSTRACT

The maximum theoretical energy efficiency of fuel cells is much larger than those of the steam-power-turbine cycles that are currently used for generating electrical power. Similarly, direct hydrocarbon fuel cells, DHFCs, can theoretically be much more efficient than hydrogen fuel cells. Unfortunately the current densities (overall reaction rates) of DHFCs are substantially smaller than those of hydrogen fuel cells. The problem is that the exchange current density (catalytic reaction rate) is orders of magnitude smaller for DHFCs. Other work at the University of Ottawa has been directed toward the development of polymer electrolytes for DHFCs that operate above the boiling point of water, making corrosion rates much slower so that precious metal catalysts are not required. Propane (liquefied petroleum gas, LPG) was the hydrocarbon chosen for this research partly because infrastructure for its transportation and storage in rural areas already exists. In this work nickel based catalysts, an inexpensive replacement for the platinum based catalysts used in conventional fuel cells, were examined using density functional theory, DFT. The heats of propane adsorption for 3d metals, when plotted as a function of the number of 3d electrons in the metal atom, had the shape of a volcano plot, with the value for nickel being the peak value of the volcano plot. Also the C-H bond of the central carbon atom was longer for propane adsorbed on nickel than when adsorbed on any of the other metals, suggesting that the species adsorbed on nickel was less likely to desorb than those on other metals. The selectivity of the propyl radical reaction was examined. It was found that propyl radicals were more likely to dehydrogenate to form allyl radicals that remain on the surface (desired reaction) than react with hydroxyl

groups to form propanol that would become a partially oxidized final product (undesired reaction). Intermediate reaction products that stay on the surface are desired because they have the possibility of reacting further and eventually forming CO_2, which is the complete combustion product, indicating that the maximum amount of chemical energy has been transformed to electrical energy. Alloy catalysts were investigated in which either Fe or Cu was added to the nickel. Fe addition caused a decrease in the adsorption energies of both water and propane. In contrast Cu addition caused the opposite, an increase in the adsorption energies of both water and propane. The addition of Fe promoted the water dissociation reaction (a decrease in activation energy) and inhibited the propane dehydrogenation reaction (an increase in activation energy). Decreases in activation energy are desirable because they increase the exchange current density (catalytic reaction rate).

RÉSUMÉ

L’efficacité théorique énergétique maximale des piles à combustible est beaucoup plus grande que celles des turbines à vapeur qui sont actuellement utilisées pour produire de l'énergie électrique. De plus, les piles à combustible d'hydrocarbures (DHFC) peuvent théoriquement être beaucoup plus efficaces que les piles à combustible d'hydrogène. Malheureusement les densités de courant des DHFCs sont sensiblement plus petites que celles de piles à combustible à hydrogène. D'autres travaux à l'Université d'Ottawa ont été dirigés vers le développement des électrolytes polymères pour DHFCs qui opèrent au-dessus du point d'ébullition de l'eau, ce qui rend les taux de corrosion beaucoup plus bas de sorte que les catalyseurs de métaux précieux ne sont pas nécessaires. Le propane (gaz de pétrole liquéfié, GPL) était l'hydrocarbure choisi pour cette recherche, en partie parce que les infrastructures pour le transport et le stockage dans les zones rurales existent déjà. Dans ce travail, des catalyseurs au nickel, un remplacement peu coûteux pour les catalyseurs à base de platine utilisés dans les piles à combustible conventionnelles, ont été examinés en utilisant la théorie de la fonctionnelle de la densité, DFT. Les chaleurs d'adsorption du propane sur les métaux 3d, lorsqu'elle est donnée en fonction du nombre d'électrons 3d dans l'atome de métal, avaient la forme d'un graphique de type "volcan", avec la valeur pour le nickel au sommet. Aussi la liaison CH de l'atome de carbone central était plus longue pour le propane adsorbé sur le nickel que lorsqu'il est adsorbé sur tout autre métal, ce qui suggère que les espèces adsorbées sur le nickel étaient moins susceptibles de désorber que celles sur d'autres métaux. La sélectivité de la réaction propyle a été examinée. Il a été constaté que les radicaux propyle étaient plus susceptibles

à se déshydrogéner pour former des radicaux allyliques qui restent sur la surface (réaction souhaitée) que de réagir avec les groupes hydroxyles pour former le propanol qui allait devenir un produit partiellement oxydé final (réaction indésirable). Les produits de réaction intermédiaires qui restent sur la surface sont désirables parce qu'ils ont la possibilité de réagir plus loin et finissent par former du CO_2, le produit de la combustion complète, ce qui indique que le montant maximum d'énergie chimique a été transformé en énergie électrique. Des alliages catalyseurs ont été étudiés dans laquelle soit Fe ou Cu ont été ajoutés à du nickel. Le Fe a entraîné une diminution dans les énergies d'adsorption de l'eau et du propane. Par contre, le Cu a entraîné l'effet opposé, soit une augmentation de l'énergie d'adsorption de l'eau et du propane. L'ajout de Fe promut la réaction dissociation de l'eau (une diminution de l'énergie d'activation) et inhibe la réaction de déshydrogénation du propane (une augmentation de l'énergie d'activation). Des diminutions de l'énergie d'activation sont souhaitables, car ils augmentent la densité de charge actuelle (vitesse de la réaction catalytique).

Dedication

I dedicate this work to the two most significant people in my life, my dearest uncle "Farough" who has believed in me and my success at all times, even when I seriously doubted myself; and my belated beloved father who taught me, very early in life, to be self-confident, strong and independent regardless of what life brings my way.

Statement of Contributions of Collaborators

I hereby declare that I am the sole author of this thesis. I have performed all the computational work and data analysis and I have written all the materials included in this thesis.

Throughout the course of my Ph.D. studies, my supervisor, Dr. Marten Ternan has provided me with continual support and guidance. Also, my co-supervisor Dr. Alain St. Amant has guided me in understanding and resolving computational difficulties in regards to the program (SIESTA) and the method (DFT) used for the computational work done for this thesis.

Acknowledgement

I like to express my sincere appreciation to my supervisor Dr. Marten Ternan, for providing me with the opportunity to peruse my studies as a Ph.D. candidate learning and exploring original knowledge towards innovation of a completely redesigned "Direct Propane Fuel Cell". I am truly grateful for his support and mentoring throughout the course of my Ph.D. studies. I have looked up to him and counted on his advice in difficult professional and at times, personal situations. I feel very fortunate to have known and worked with such caring and understanding individual with enormous pool of hands on knowledge as my supervisor.

I would also like to thank my co-supervisors Dr. Alain St. Amant for guiding me throughout all my computational difficulties, and providing me with significant methodology knowledge and effective directions.

I am very appreciative of the National Science and Engineering Research Council (NSERC) and Ontario Fuel Cell Research and Innovation Network (OFCRIN) for their financial assistance without which this accomplishment would not have been possible.

I am forever grateful and truly thankful to my uncle Farough for being by my side in every major decision I have made stepping forward in life. His unconditional love and support have been the only constants in my life. I am a better person everyday being inspired and guided by his enormous senses of compassion, thoughtfulness, integrity and

forgiveness.

Finally I am forever thankful to God for blessing me with the gift of my father without whom I would not be the person that I am today. Even though he is not with me anymore, he has always watched over me and his loving powerful words of wisdom have guided me in overcoming all obstacles and challenges I have confronted all my life.

I am honored and feel extremely privileged to have had such great role models and inspirations in my life to whom I am forever grateful.

Table of Contents

List of Figures

List of Tables

List of Equations

Nomenclature

ΔG: The change in Gibbs free energy of the reaction ($J\ mol^{-1}$)

ΔH: The molar heat of combustion of the fuel ($J\ mol^{-1}$ *or* $J\ molecule^{-1}$)

$\hat{H}$: Hamiltonian

Ψ: Wave function

Ψ_0: Ground state wave function

E: Energy ($J\ mol^{-1}$)

$\hbar$: Reduced Planck's constant ($J\ s$)

m_i: Mass of electron *i (kg)*

m_A: Mass of nucleus *i (kg)*

q_i: Charge of electron i (*C (coulomb) = s A)*

q_j: Charge of electron j (*C (coulomb) = s A)*

q_A: Charge of nucleus A (*C (coulomb) = s A)*

ε_0: Permittivity $(F/m = kg^{-1}\ m^{-3}\ s^4\ A^2)$

r_{iA}: Electron-nucleus distance $(A° = 1^{-10}\ m)$

q_B: Charge of nucleus B (*C (coulomb) = s A)*

$\mathbf{r_{ij}}$: Electron-electron distance $(A° = 1^{-10}\ m)$

r_{AB}: nuclei distance $(A° = 1^{-10}\ m)$

$\hat{H}_{el}$: Electronic Hamiltonian

Ψ_{el}: Wave function of the electronic Schrödinger equation

***1s(1)*:** is the molecular orbital (the space function) associated with electron 1

***α(1)*:** is the spin coordinate of electron 1

1s(1)α(1): spin orbital

E_0 :ground state energy ($J\ mol^{-1}$)

$\rho_0(r)$: Ground-state electron density function

$v(r)$: External potential $(V = m^2\ kg\ s^{-3}\ A^{-1})$

$E_{ki}(\rho(r))$: Kinetic energy functional

$E_{xc}(\rho(r))$: exchange-correlation energy functional

$E_{col}(\rho(r))$: Columbic energy functional

$E(\rho_0(r))$: Energy functional for ground state density function

$E(\rho(r))$: Energy functional for any density

$\rho(r)$: Density function

θ_i^{KS}: Kohn-Sham orbitals

G: Reciprocal lattice vector space

E_{cutoff}: Cut off enrgy ($J\ mol^{-1}$)

N_{pw}: Number of planewaves

r: Represents the point in space where the function is evaluated at

$\varphi_j(r)$: planewave basis function

$C_{j\alpha}$: Constant (Eq. 2.11)

N: Normalization constant (Eq. 2.12)

h: Direct lattice vector space matrix (Eq. 2.13)

$2\pi(h^t)^{-1}$: Reciprocal lattice vector space matrix

T: Position vector in the direct lattice (Eq. 2.14)

Ω: Volume of the lattice (nm^3)

a_i: Unit vectors of the direct lattice vectors

b_i: Unit vectors of the reciprocal lattice vectors

n_i: integers

$f(r)$: Planewave function

k: arbitrary fixed vector in reciprocal lattice G

k-point: Special points in reciprocal lattice G

$V(r)$: Periodic Potential (V) (Eq. 2.21)

$\Psi_\alpha(r)$: Periodic wave function (Eq. 2.22)

K_{prs}: Reciprocal lattice vector space in directions p, r and s

u_r, u_p **and** u_s: Integers in r, p and s directions respectively

p, r **and** s: Directions

r_c: Core radius

q_r: Determines the number of k-pints in r direction

$E_{adsorbate+slab}$: Total electronic energies for the absorbate plus metal slab ($J\ mol^{-1}$)

$E_{gadsorbate(gas)}$: Electronic energy of isolated adsorbate molecule in the gas phase (J/mol)

$(E_{adsorbate+slab})_{MIN}$: Total electronic energy for the configuration of the adsorbate plus metal slab that has the minimum energy (initial state of the reaction) ($J\ mol^{-1}$)

E_{slab}: Electronic energy for a metal slab ($J\ mol^{-1}$)

$(E_{adsorbate+slab})_{MAX}$: Total electronic energy for the reactant molecule(s) on the metal slab at the reaction transition state (maximum adsorbate+slab energy) ($J\ mol^{-1}$)

j: Current density (Eq 5.3) in mA/cm^2

j_0: Exchange current density (mA/cm^2)

n_c: moles of charged species per mole of molecular species

F: Faraday constant (96485 *C/mole* of charged species)

η: Overpotential (V)

k_F: Overall rate constant for a first order reaction (s^{-1})

T: Temperature (*K*) (Equation 5.3-5.4)

α: Transfer coefficient (Eq.5.4)

R: Gas constant ($J\ K^{-1}\ mol^{-1}$)

$\Delta\phi_{EQ}$: Anode half cell potential at equilibrium

E_{act}: Activation energy or energy barrier of the reaction $(J\ mol^{-1})$

Abbreviations

ADPACK: Atomic Density functional program PACKage

AFC: Alkaline Fuel Cell

B3LYP: P.14 Becke 3 parameter-Lee-Yang-Par) (hybrid exchange correlation density functional)

B88LYP: Becke-Lee-Yang-Par (88 stands for special parameters)

bcc: Body-Centered Cubic

BOA: Born-Oppenheimer Approximation

BZ: Brillioun Zone

ca: Ceperley-Alder

CG: Conjugate Gradient

DAM: Dipped Adcluster Model

DFT: Density Functional Theory

DHFC: Direct Hydrocarbon Fuel Cell

DM: Density Matrix

DPFC: Direct Propane Fuel Cell

ECP: Effective Core Potentials

FC: Fuel Cell

fcc: Face-Centered Cubic

FDF: Flexible Data Format

FFT: Fast Fourier Transforms

GAMESS: General Atomic and Molecular Electronic Structure System

GDL: Gas Diffusion Layer

CFD: Computational Fluid Dynamics

GGA: Generalized Gradient Approximation

HF: Hartree-Fock

hcp: Hexagonal Closed Packed (crystal structure)

HPCVL: High Performance Computing Virtual Laboratory

IS: Initial State

KS: Kohn-Sham

LDA: Local Density Approximation

LPG: Liquefied Petroleum Gas

LYP: (or BLYP Becke Lee-Yang-Par

M/WC: Metal catalyst supported on tungsten carbide

MCFC: Molten Carbonate Fuel Cell

MD: Molecular Dynamics

ME: Metal

MEA: Membrane-Electrode Assembly

ML: Mono Layer

MO: Molecular Orbital

MP2: Improved Moller-Plesset

NWChem: North-West National Laboratory of Chemistry

ORR: Oxygen Reduction Reaction

PAFC: Phosphoric Acid Fuel Fell

PBI: Polybenzimidazole

PEMFC: Polymer Electrolyte or Proton Exchange Membrane Fuel Cell

PTFE: Polytetrafluoroethylene

PW91: Perdew-Wang 1991

PW: Plane Wave

QCHEM: Quantum Chemistry (software)

QM: Quantum Mechanical

QUEST: Quantum Electronic STructure

RPBE: Revised Perdew-Burke-Ernzerhof

SCF: Self Consistent Field

SHC: Saturated Hydrocarbon

SOFC: Solid Oxide Fuel Cell

tm2: Improved Troullier-Martins

TS: Transition State

USSP: Ultra-Soft Pseudo-Potential

VASP: Viação Aérea São Paulo (QM computation software)

XC: Exchange Correlation

XRD: X-Ray Diffraction

ZPE: Zero Point Energy

ZrP: Zirconium Phosphate

ZM: Z Matrix a format for input file in SIESTA program

CHAPTER 1

Introduction

Fuel cells are one of the enabling technologies for future energy use. Like batteries fuel cells are electrochemical devices that convert the chemical energy of the reactants, a fuel and an oxidant, into electrical energy. The following section is an overview of fuel cells including structure, types, fuels and their history.

1.1 Fuel C ells: History and Types

The history of fuel cells covers almost two centuries. In 1839, William Grove, the British barrister, reported the first experiments with a fuel cell. He called his device a gas battery, i.e. the first fuel cell [1]. Since this early discovery, there has been a long period of research and development. Figure 1.1 shows a historical review of most fuel cell innovations to date.

Today fuel cell technology is diverse. Fuel cells (FCs) differ in the type of materials, the fuel used, operation conditions such as temperature and the end use. Hence many types of fuel cells have been and are being developed. Based on the type of electrolyte used, fuel cells can be classified as: proton exchange membrane fuel cells (PEMFCs), alkaline fuel cells (AFCs), phosphoric acid fuel cells (PAFCs), molten carbonate fuel cells (MCFCs), and solid oxide fuel cells (SOFCs). These five FC types are compared in Table 1.1.

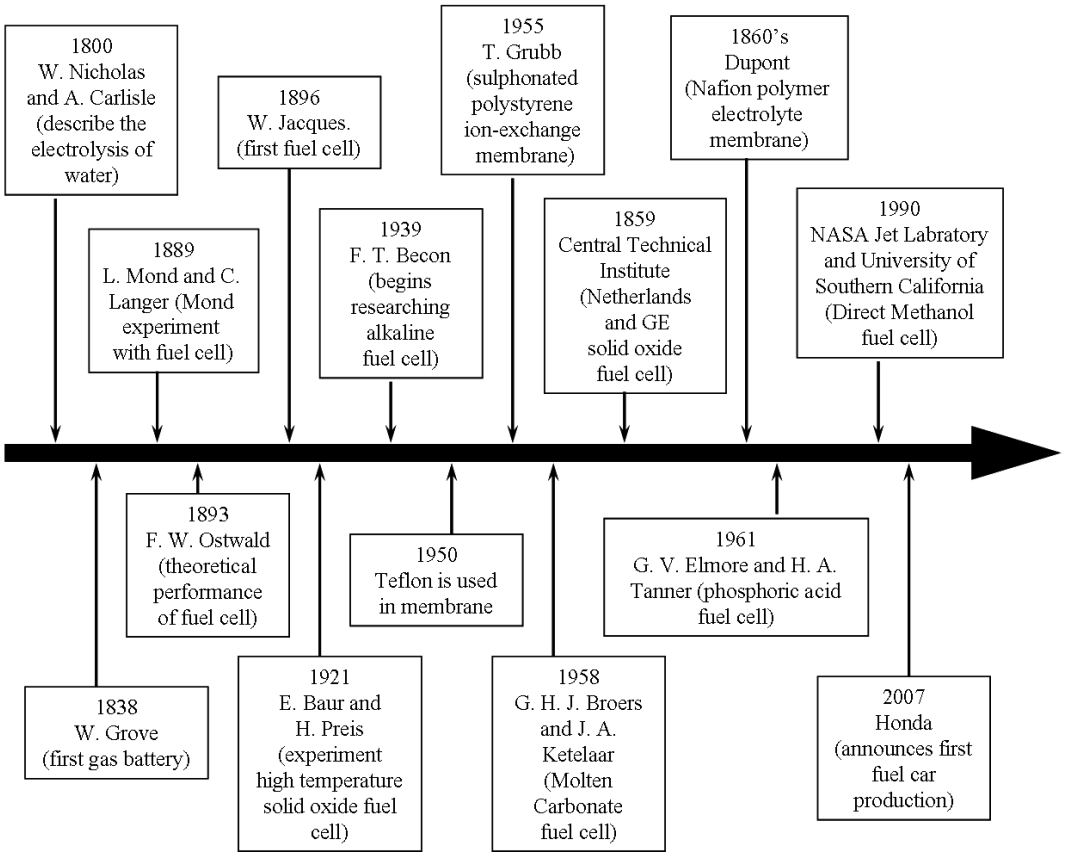

Figure 1.1: Historical review of most fuel cell innovations to date [1]

Table 1.1: Overview of fuel cell types [2-4]

Fuel cell types	Operating Temp. (°C)	Electrolyte & charge carrier	Fuel	Electrochemical Reactions
Alkaline fuel cell (AFC)	80-100	Aqueous solution of Potassium hydroxide (OH^-)	H_2	Anode : $H_2+2OH^- \rightarrow 2\,H_2O + 2e^-$ Cathode: $½\,O_2 + H_2O + 2e^- \rightarrow 2OH^-$
Polymer electrolyte Membrane fuel cell (PEMFC)	60-120	Solid organic polymer e.g. Poly-perfluorosulfonic acid (H^+)	H_2, (CO ≤ 10 ppm)	Anode : $H_2 \rightarrow 2H^+ + 2e^-$ Cathode: $½\,O_2 + 2H^+ + 2e^- \rightarrow H_2O$
Phosphoric acid fuel cell (PAFC)	60-250	Immobilized phosphoric acid (H^+)	H_2, (CO < 5%)	Anode : $H_2 \rightarrow 2H^+ + 2e^-$ Cathode: $½\,O_2 + 2H^+ + 2e^- \rightarrow H_2O$
Molten carbonate fuel cell (MCFC)	600-700	Molten alkali carbonates (CO_3^{2-})	H_2, CO, hydrocarbons	Anode : $H_2 + CO_3^{2-} \rightarrow H_2O + CO_2 + 2e^-$ Cathode: $½\,O_2 + CO_2 + 2e^- \rightarrow CO_3^{2-}$
Solid oxide fuel cell (SOFC)	600-1100	Solid oxide e.g. zirconium oxide with ytrria (O^{2-})	H_2, CO, hydrocarbons	Anode : $H_2 + O^{2-} \rightarrow H_2O + 2e^-$ Cathode: $½\,O_2 + 2e^- \rightarrow O^{2-}$

1.2 Polymer Electrolyte Membrane Fuel Cell

Polymer electrolyte membrane or proton exchange fuel cells (PEMFCs) have attracted

a great deal of attention. PEMFCs can be divided into subcategories based on the fuel used. The most common fuels used in PEMFCs are hydrogen and methanol. PEMFCs are popular because of their low operating temperature of about 80°C, low emissions and high power density. They are known for their good performance and a wide range of possible applications including stationary power generation, vehicles and electronic devices [1, 5-6].

1.2.1 PEMFC Components

A cross section structure of hydrogen PEMFC is shown in Figure 1.2. A PEMFC typically consists of a proton conducting membrane, two electrodes, anode and cathode, gaskets, graphite bipolar plates and gas diffusion layers. The membrane-electrode assembly (MEA) that consists of the proton conducting membrane sandwiched between the two electrodes (anode and cathode), is the heart of a PEM fuel cell. The membrane is typically 50-175 μm thick [7] and it is made of perfluorosulfonated polymers. Dupont's Nafion® polymer is one of the perfluorosulfonated polymers most widely used [8]. In each electrode there is a catalyst layer and a gas diffusion layer (GDL). The catalyst layer is about 50 microns [9] thick, most commonly containing dispersed platinum (Pt) supported on carbon particles. The GDL that is in immediate contact with the catalyst layer is hydrophobizied porous carbon paper or carbon cloth, with a thickness of 100-400 μm [7]. These layers are wet-proofed by treatment with polytetrafluoroethylene (PTFE).

The role of GDL is to enable direct and uniform access of the reactant gases to the catalyst layers as well as to supply and remove water in either vapor or liquid form. It

should consist of material with high and stable electronic conductivity in a wet environment [7].

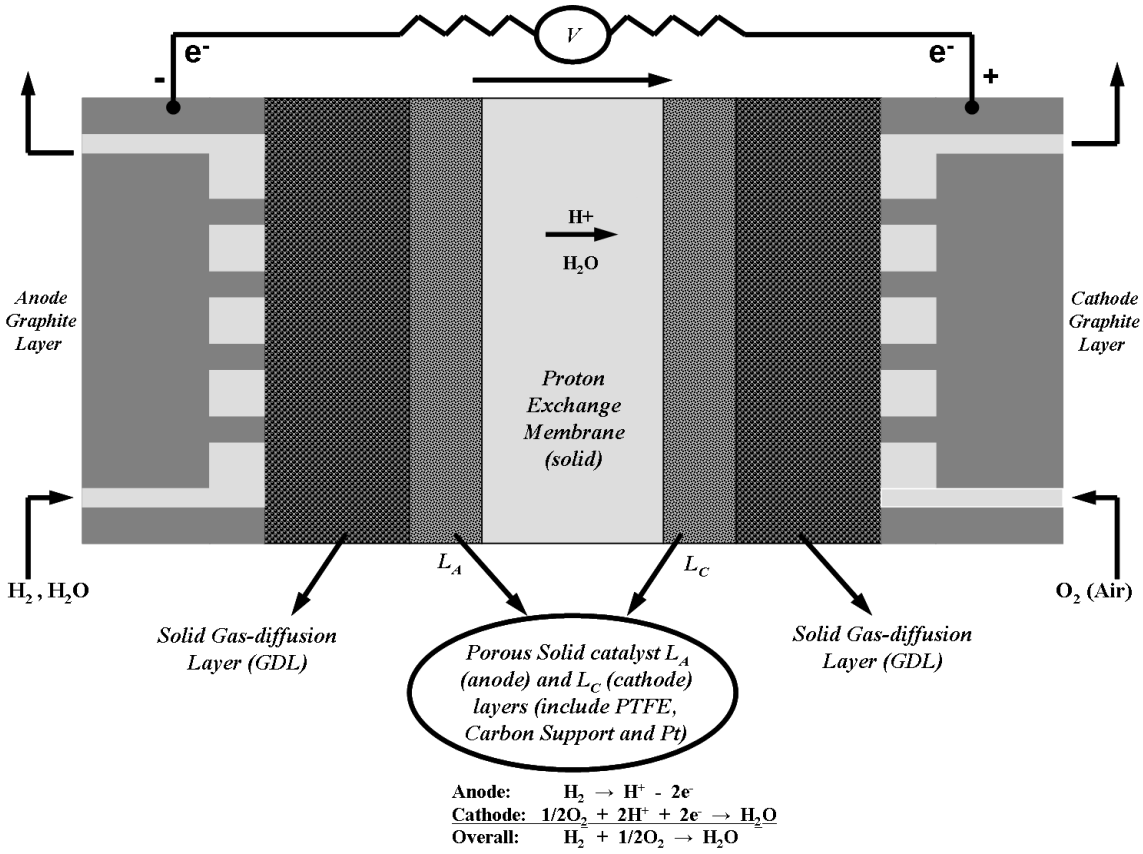

Figure 1.2: Cross-section structure of PEMFC

The membrane functions in a fuel cell are mainly three fold. It acts as the electrolyte that provides ionic (protons) communication between the anode and the cathode, while being an electronic insulator and it also serves as a separator for the two reactant gases. Optimized proton transport properties of the membrane and proper water management are crucial for efficient fuel cell operation. Dehydration of the membrane reduces proton conductivity and excess water can lead to flooding of the electrodes, thus, impeding

gaseous reactant transport to the catalyst. Both conditions result in poor fuel cell performance [10].

The membranes based on Nafion® materials present two main limitations: their high cost and their maximum operation temperature, limited to 90°C [8, 11]. Above this temperature, the membrane dehydrates and the conductivity falls. In addition, at its low operating temperature, CO poisons the Pt catalyst. To reduce or eliminate the CO poisoning, high proton conductivity membranes that tolerate temperatures of 150-200 °C are required [11].

The electro-catalysts (catalyst layers) are important in the fuel cell structure. They provide sites for electrochemical reactions taking place in the fuel cell. Depending on their chemical and physical properties they could significantly affect the rates of the reactions on either electrode. It is essential for the catalyst layer to have electrical conductivity [12], so it could provide both a continuous ionic pathway (eg. Nafion) and a electronic pathway (e.g. Pt/C). This layer also needs to be accessible to the gas molecules. The most common catalyst used for both anode and cathode is platinum with a state-of-the-art loading [13] of 0.1-0.2 mg/cm^2. This is a major decrease from 28 mg/cm^2 used in 1960's [14]. Platinum is an expensive precious metal. It has a very low CO tolerance of about 5-10 ppm^2 that affects the fuel cell power output significantly [15].

The bipolar plates serve a dual role of providing flow fields for gases and as current collectors. The plates are made of a light-weight, strong, gas-impermeable, electron-

conducting material. Graphite or metals are commonly used [2, 5]. The first task served by each plate is to provide a gas flow field while maintaining electronic contact with the gas diffusion layer. The plates contain channels (machined into the plate) and are in immediate contact with the GDL. The pattern of the flow field in the plate, as well as the width and depth of the channels, have a large impact on the effectiveness of the distribution of the reactant gases, and, hence, the current distribution across the MEA. Flow field design also affects the water supply to the membrane and water removal from the electrode. Consequently, it can affect the local membrane conductivity. The second role of the plate is as a current collector. Electrons produced by the oxidation of hydrogen must be conducted through the anode, through the GDL and through the plate before they can exit the cell, travel through the external circuit and re-enter the cell at the cathode plate. Thus, there must be a good electronic contact between the plates and the GDL [2, 5].

The Teflon® masks are gaskets that confine the gas flow to the interior of the flow field and provide an effective seal to avoid leakage of reactant gases [2].

1.2.2 Fuels for PEM Fuel Cells

1.2.2.1 Hydrogen

Hydrogen is the most common fuel for fuel cells. It has excellent electrochemical reactivity, provides high levels of power density, and has zero emission characteristics. However the infrastructure for its widespread distribution does not yet exist. Distribution and storage difficulties currently pose serious challenges to the use of pure hydrogen as

the feed for fuel cells in automotive-propulsion [16]. Today, approximately 95% percent of all hydrogen is produced by "steam-reforming" of natural gas, the lowest cost, large scale method of production.

1.2.2.2 Methanol

A common choice among possible fuels fed directly to the anode is methanol in DMFC. The advantages of supplying methanol directly to the fuel cell are significant. Liquids are easier to handle than gases. Feeding the fuel directly eliminates the fuel processing cost to make hydrogen, but does not eliminate the fuel processing cost to convert natural gas to methanol. However, there are some inherent problems with DMFCs. The slow anode kinetics (methanol electro-oxidation) requires a large overpotential and severely decreases the cell potential difference [17]. Perfluorosulforic-acid based membranes such as Nafion® have the problem of methanol cross over, which results in methanol and O_2 reacting at the cathode (O_2 reduction) without electrons being transferred through the electrical circuit. Thereby it reduces the total energy efficiency. Large amounts of anodic catalyst (noble metal) are needed for the electro-oxidation of methanol and to reduce the electrocatalyst self poisoning effect due to CO adsorption on the catalyst [1, 3, 12].

1.2.2.3 Hydrocarbon

Hydrocarbon fuels have great potential for use directly as the fuel in PEMFCs. This potential is due to the advantages of hydrocarbons in comparison with hydrogen. Compared to hydrogen, hydrocarbons provide higher energy density. There is an

established existing infrastructure for them. They are easy to store, more energy efficient (hence, less CO_2 emissions), and since they are fed directly to the fuel cell, the cost of fuel processing is eliminated. The maximum electrical energy efficiency ($\Delta G/\Delta H$) for complete methane oxidation to CO_2 in a CH_4/O_2 fuel cell at 25^oC (producing CO_2 and liquid water) is 0.92. The same quantity is 0.94 for ethane, 0.95 for propane 0.95 and 0.97 for octane 0.97, and 0.83 for H_2 oxidation [18-21]. However there is an addition loss of 0.25 or more to produce hydrogen by steam-reforming which brings the $\Delta G/\Delta H$ to less than 0.58. Despite their great potential, direct hydrocarbon fuel cells (DHFCs), exhibit very low current densities (reaction rates) which are orders of magnitude smaller than those for both hydrogen fuel cells and for DMFCs. Hence, in a DHFC the main challenge is the slow anodic kinetics of the hydrocarbon fuel electro-oxidation, at low temperature.

In all PEMFCs operating with any fuel, the cathode is the same. The details may vary, but a fuel cell cathode is invariably an electrode that reduces oxygen. The processes at the fuel cell anode [12] cause the overwhelming difference in performance among these fuels.

1.2.3 PEM Fuel Cell Performance

The fuel is oxidized on the anode catalyst, yielding electrons and protons. The protons travel through the proton selective membrane to reach the cathode side. Since the membrane is proton selective it does not allow electrons to pass through it, hence the electrons must get to the cathode through a circuit that includes the carbon support, in the catalyst layer, the porous carbon in the diffusion layer, the graphite plates and the

external electrical wires. On the cathode catalyst, oxygen combines with electrons from the external electrical wires and protons from the electrolyte to produce water [10, 12]. The electrochemical reactions occurring at the cathode and the anode of the PEMFC are shown in Table 1.1 (above).

The polarization curve (Figure 1.3) that represents the cell potential-current relationship is the standard figure of merit for evaluation of fuel cell performance. Potential versus current density, scaled by geometric electrode area, is typically shown, so that the results are scalable between differently sized cells. The curve shows the positions of the polarizations (losses) that cause a drop in potential, and the combined effect of all losses at a particular operating condition. The losses (at low current densities) are due to (kinetic) overpotential caused by surface processes at the electrodes. The ohmic polarization (at intermediate current densities) includes electrical and ionic conduction losses through the electrolyte, catalyst layers, cell interconnects and contacts. Concentration losses (at high current densities) are caused by mass transport limitations of the reactants to the electrodes. The combined contributions of the sources of overpotential loss and the other two polarization losses cause the cell potential output to decrease with increasing current density [21]. A polarization curve is typically recorded by starting at the open circuit potential and then increasing current and taking measurements at prescribed potential or current intervals [22]. A typical polarization curve is shown in Figure 1.3 below.

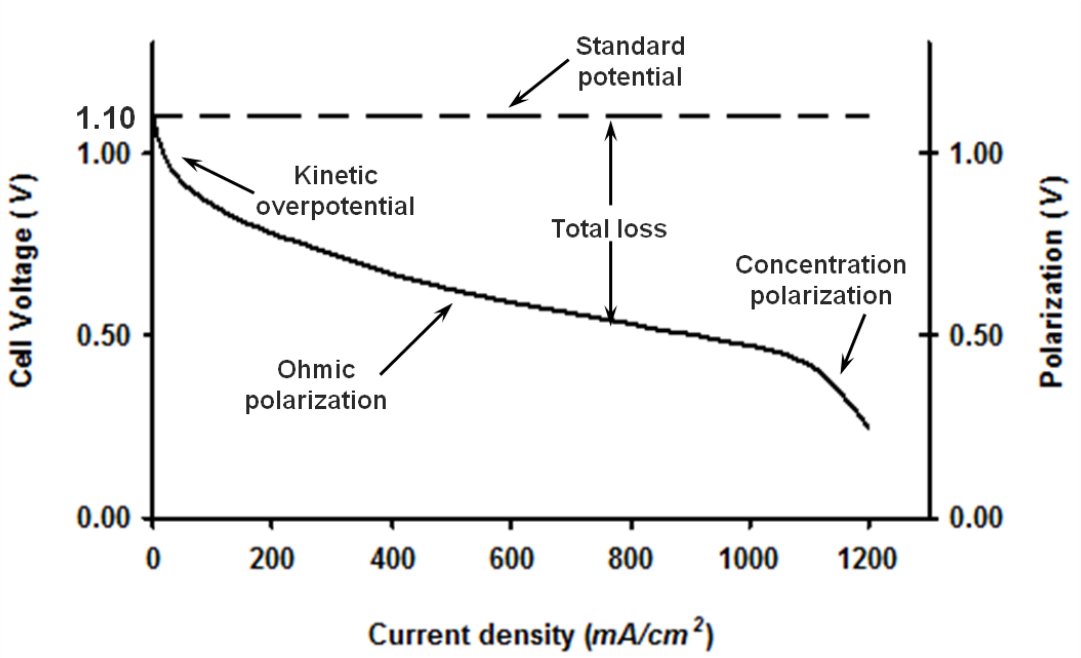

Figure 1.3: Typical polarization curve

1.3 Fuel Cell Concept Investigated in this Work

As presented above, direct hydrocarbon fuel cells (DHFCs) can be PEMFCs in which hydrocarbons are used directly as the fuel instead of hydrogen. DHFCs have great potential for a future fuel cell industry. This potential is due to many advantages (mentioned above) that DHFCs have when compared to hydrogen PEMFCs. The hydrogen production process in hydrogen PEMFCs accounts for 30% of the cost of the fuel cell [18]. Hence the possibility of using hydrocarbon fuels that do not need processing and can directly be fed to the fuel cell will eliminate this significant portion of the fuel cell cost. The focus of our group's research was on direct propane fuel cells. The objective was to improve the earlier versions of DPFCs by applying major modifications to the methods and materials used in them. Particular concentration in this work was on the anodic electro-catalyst and the electro-oxidation reaction of propane at the anode.

Many state-of-the-art catalysts used in fuel cells are comprised of Pt-group metals, and large loadings of these metals are required for efficient fuel cell operation. High cost and limited supplies of such precious metals potentially create prohibitive barriers to market penetration and scale-up of fuel cell production. Operating at a temperature above the boiling point of water, means there is no liquid water present in the system. This leads to less corrosion and therefore the possibility of using catalysts other than precious metals such as platinum. Hence, nickel (supported on carbon) was chosen as the anodic electro-catalyst, because it is less expensive than platinum and it has been used in alkaline fuel cells previously. Our goal was to enhance the anodic propane electro-oxidation kinetics under the operating temperature of about 150-200°C for the DPFC, (higher compared to PEMFC), and by employing a non-precious metal or metal alloy catalyst that can allow the electro-oxidation reaction.

The reactions in DPFCs, including anodic electro-oxidation of propane, cathodic reduction of oxygen and the overall FC reaction are shown in equations 1.1-1.3:

Anode: $C_3H_8(g) + 6H_2O(g) \rightarrow 3CO_2(g) + 20H^+ + 20e^-$ (1.1)

Cathode: $5O_2(g) + 20H^+ + 20e^- \rightarrow 10H_2O(g)$ (1.2)

Overall: $C_3H_8(g) + 5O_2(g) \rightarrow 3CO_2(g) + 4H_2O(g)$ (1.3)

In an ideal system propane reacts with water on the anode surface (Eq. 1.1), producing carbon dioxide, protons and electrons (anode reaction above). This is a multistage reaction with a complex mechanism through which production of a number of

intermediate by-products is possible. The reactions involved in this process are dissociative chemisorptions of propane, dissociative chemisorption of water, dehydrogenation, hydroxylation of adsorbed carbon species, and carbon-carbon bond cleavage. The possible by-products are propanol, propionaldehyde, propionic acid, ethanol, acetaldehyde, acetic acid, methanol, formaldehyde, formic acid and carbon monoxide. In this research some of these reactions were investigated by means of DFT calculations.

1.3.1 Objectives

The followings were the three main objectives in this research which were achieved by means of DFT calculations: First, a non precious 3d metal catalyst was to be identified as the anode catalyst of the DPFC, ideally one that would allow relatively strong adsorption of propane for its progressive oxidation to CO_2. Second, the selectivity of the identified catalyst was to be examined with respect to production of desired and undesired (e.g. oxygenated) by-products in the propane electro-oxidation process. Third, the capability of 3d metal alloys as alternative anodic catalysts that enhance the propane electro-oxidation process was to be examined. Taking into account that propane electro-oxidation is a complicated reaction involving many reaction steps and reaction by-products only some primary steps of the electro-oxidation reaction were to be examined.

1.3.2 Thesis Structure

This is a paper-based thesis organized in 8 chapters. The first three chapters provide: an introductory knowledge base on fuel cells, particularly DPFCs, and why they are of in-

interest (chapter 1), a descriptive background on the methodology and the theory behind it (chapter 2), and a literature review of DFT studies on fuel cell catalysts and reactions (chapter 3). Chapters 4, 5 and 6 are a collection of three papers reporting the work done and the results obtained in this research. In chapter 7 an overview of the thesis and an analysis of the three papers are provided. In chapter 8, a list of the main conclusions from the three studies, the original contributions to knowledge and some recommendation for future work, are provided. The thesis ends with an appendix. The following is a brief description of the content in the three papers.

Three studies were performed to investigate a suitable non-precious metal catalyst for the anode of DPFC, and to investigate a likely reaction pathway leading to complete propane electro-oxidation (production of CO_2). Adsorption energy and activation energy calculations were performed by employing DFT with SIESTA (Spanish Initiative for Electronic Simulation with Thousands of Atoms) software. The first study, Chapter 4, was a sequel to work by Psofogiannakis et al. [23] In their study of anodic electro-oxidation of methane in direct methane fuel cell, Psofogiannakis et al. [23] determined that chemisorption of methane on the surface of the anode catalyst, was the rate limiting reaction step, in the methane electro-oxidation process at the anode of direct methane fuel cell. The first part of the work described here was based on this study. To identify a non-precious metal that allows this reaction step, during the propane electro-oxidation process, chemisorption of propane on the surface of 3d metals was investigated in the first study reported here. Among the 3d metals examined, nickel was identified for this reaction, since it adsorbed propane more strongly than the other metals investigated.

In the second study, Chapter 5, the possible production of unwanted alcohol byproducts, specifically propanol, was investigated among the primary steps of the propane electro-oxidation reaction. Based on activation energies, it was concluded that compared to an allyl radical ($*C_3H_6$), a propanol by-product is less likely to be produced and released to the gas phase. As it is with any surface reaction process, it is important for the intermediate by-products of the propane electro-oxidation reaction to stay adsorbed on the surface long enough for the reaction to progress to completion (the production of CO_2 as the predominant product).

The third study, Chapter 6, concentrated on examining 3d metal alloys as possible multifunctional catalysts for the anode of a DPFC. Keeping nickel as the primary metal component, two different alloys were considered as the catalyst surface, 35Ni/1Me (slab of 35 nickel atoms and 1 metal atom from the 3d transition metals) and 28Ni/8Me (slab of 28 nickel atom and 8 secondary metal atoms). The secondary metals, Me, that were introduced into the slab were copper (Cu) and iron (Fe). For both water and propane adsorption Fe was an inhibitor (decreasing the adsorption energy), and Cu was a promoter. Fe was an inhibitor for propane dehydrogenation (increasing the energy barrier). It was a promoter for the water dissociation reaction (decreasing the energy barrier).

1.4 References

[1] Andujar, J. M., Segura, F.; *Renewable and Sustainable Energy Reviews* **2009**, *13*, 2309

[2] Zhang, J.; "*Investigation of CO Tolerance in Proton Exchange Membrane Fuel Cells*"Ph.D. Thesis in Chemical Engineering, Worcester Polytechnic Institute, **2004**

[3] Nikolla, E.; "*Combined Experimental/Theoretical Approach toward the Development of Carbon Tolerant Electrocatalysts for Solid Oxide Fuel Cells*" Ph.D. thesis in Chemical Engineering, University of Michigan, **2009**

[4] Bassler, W. G.; "*Electrochemistry and Transport in Solid Oxide Fuel cells*", Ph.D. thesis in Chemical Engineering, University of Heidelberg, **2007**

[5] Ramani, H., Kunz, R., Fenton, J. M.; "*Polymer Electrolyte Fuel cell*" Electrochemical Society Interface, **2004**

[6] Ramani, V.; "*Fuel Cells*", Electrochemical Society Interface, **2006**

[7] Igarshi, H., Uchida, H., Watanabe, M.; *Studies in Surface Science and Catalysis* **2001**, *132*, 953

[8] Asensio, J. A., Borros, S., Romero, P., G.; *Journal of the Electrochemical Society* **2004**, *151*, A304

[9] Wieckowski, A., Koper, M.; *Fuel Cell Catalysis: A surface Science Approach*, J. Wiley & Sons, Inc., Hoboken, New Jersy, **2009**

[10] Department of Energy Office of Fossil Energy National Energy Technology Laboratory, *Fuel Cell Handbook, 7th edition*, EG & G Technical Services Inc., **2004**

[11] Wainright, J. S., Wang, J. T., Weng, D., Savinell, R. F., Litt, M.; *J. Electrochem. Soc.*, **1995**, *142*, L121

[12] Scherer, G. G., Gursel, S. A.; *Fuel Cells I*, Springer, Berlin, **2008**

[13] Weidner J., Sethuraman V. A., Van Zee J.W.; *Electrochem. Soc. Interface* **2003**, *12*, 40

[14] Ralph T.R., Hogarth M.P.; *Platinum Metals Rev.* **2002**, *46*, S14

[15] Haug A.T.,White R., Weidner J.W., Huang W.; *J. Electrochem. Soc.* **2002**, *149*, A862

[16] He, C. Z., Kunz, R., Fenton, J. M.; *J. Electrochem. Soc.* **2001**, *148*, A1116

[17] Xu, Y., Mavrikakis, M.; *Surf. Sci*. **2001**, *494*, 131

[18] Savadogo, O., Varela, F. J. R.; *New Mat. Electrochem. Sys.* **2001**, *4*, 93

[19] Bockris, J. O'M., Srinivasan, S.; *Fuel Cells: Their Electrochemistry*, McGraw-Hill Inc., New York, **1966**

[20] Savadogo O., *J. Power Sources*, **2004**, *127*, 135

[21] Ledjeff-Ney K., *J. Power Sources* **2002**, *86*, 166

[22] Barbir, F.; *PEM Fuel Cell: Theory and Practice*, Elsevier Academic press, Burlington, MA, **2005**

[23] Psofogiannakis, G., St-Amant, A., Ternan, M.; *J. Phys. Chem. B* **2006**, *110*, 24593

CHAPTER 2

Methodology

This section provides a brief summary on the theory of the quantum mechanical (QM) [1-4] operations that were required to run the calculations in this research, and the software used. Short descriptions of the QM terms that are used throughout this report are given. In addition the specifics and details of the methods used and calculations performed are provided.

2.1 Quantum Mechanical Operations

Quantum mechanical methodologies are capable of providing fairly accurate optimum values for system energies including adsorption energies for adsorbed molecules on catalyst surfaces and activation energies for surface reactions. Therefore these methods can be used to compare reaction mechanisms for surface reactions on various metals and metal alloys, to understand the metallic component of a novel catalyst.

ab initio (from first principles) methods are used by computational groups to understand structure, bonding and reaction paths. Theoretical calculations or simulations can be performed without needing to be guided by experimental data.

2.1.1 Schrödinger Equation and Wave Function

The Schrödinger equation (Equation 2.1) is the fundamental postulate of quantum me-

chanics. It is an example of the category of mathematical equations known as eigenvalue equations. When an operator, namely *"$\hat{H}$"* (the Hamiltonian operator), operates on a function, "*Ψ"* (the eigenfunction), it produces the function multiplied by a constant. In this case the constant is "*E*" (the eigenvalue), the sum of the kinetic and potential energy. The aim of quantum mechanics or *ab initio* electronic structure theory is to obtain the eigenvalues, *E*, and the eigenfunctions, Ψ, of the following Schrödinger equation (Eq. 2.1).

$$\hat{H}\Psi = E\Psi \tag{2.1}$$

The energy, *E*, is defined as the eigenvalue of molecular electronic Hamiltonian, $\hat{H}$. The Hamiltonian consists of the kinetic energy of all the electrons, kinetic energy of the nuclei and the potential energy due to the following forces: electron-nuclear attraction, electron-electron repulsion and nuclear-nuclear repulsion, shown respectively in Equation 2.2.

$$\hat{H} = \sum_{i=1}^{N} [(\hbar^2/(2m_i)) \bigtriangledown_i^2] - \sum_{A=1}^{M} [(\hbar^2/(2m_A)) \bigtriangledown_A^2] + \sum_{i=1}^{N} \sum_{A=1}^{M} (q_i q_A/(4\pi\varepsilon_0 r_{iA})) + \sum_{i=1}^{N} \sum_{j>1}^{N} (q_i q_j/(4\pi\varepsilon_0 r_{ij})) + \sum_{A=1}^{M} \sum_{B>A}^{M} (q_A q_B/(4\pi\varepsilon_0 r_{AB})) \tag{2.2}$$

The Hamiltonian in Equation 2.2 can be simplified using Born-Oppenheimer approximation (BOA) that separates (slow) nuclear motion from (fast) electronic motion, adjusting to the position of nuclei simultaneously. Therefore, the electronic energy for fixed nuclear positions is calculated and potential energy due to nuclei-nuclei repulsion is

added as a constant. The reduced electronic Hamiltonian is then:

$$\hat{H}_{el} = -\sum_{i=1}^{N}[(\hbar^2/(2m_i))\,\nabla_i^2] + \sum_{i=1}^{N}\sum_{A=1}^{M}(q_i q_A/(4\pi\varepsilon_0 r_{iA})) + \sum_{i=1}^{N}\sum_{j>1}^{N}(q_i q_j/(4\pi\varepsilon_0 r_{ij})) \quad (2.3)$$

When this operator is applied to the electronic wave function, the solution is the electronic energy as an eignvalue (Equation 2.4).

$$\hat{H}_{el}\Psi_{el} = E\Psi_{el} \quad (2.4)$$

The Ψ_{el} that is the wave function of the electronic Schrödinger equation provides a complete description of how the electrons (or the electronic system) behave. This function is impossible to solve exactly beyond the hydrogen atom for which the solution is known (1s, 2s, $2p_x$ etc). Thus, for many electron systems various approximations are generally made. In general the wave function of the Schrödinger equation is a function of *4N* coordinates (with *4N* variables) of the *N* electrons in the system. The four coordinates by which the electrons are described properly, include the three space coordinates, x, y, z, and a spin coordinate (spin α or spin up and spin β or spin down). The antisymmetry principle says that with the interchange of the four coordinates between two electrons, the sign of the wave function changes. All electrons must satisfy this requirement that along with the spin value (another fundamental electron property) initiate the quantum mechanical effect called “exchange correlation”. This effect accounts for the interaction between electrons with the same spin, such that electrons of like spin cannot be

simultaneously present in a particular space. Exchange correlation causes depletion in the density of the like-spin electrons around a given electron in the molecule and it decreases the energy of the molecule.

2.1.2 Basis-set and Pseudopotentials

A set of approximations, used to solve the Schrödinger equation, and commonly invoked in all Hartree-Fock (HF) methods, is the expansion of unknown MOs in terms of a given, fixed and finite set of basis functions known as the atomic orbital (AO) basis set. The basis set functions are normally chosen such that their linear combinations can approximate the atomic orbital of H atom. Due to complexity of the integrals of the true atomic orbitals of the hydrogen atom (the Slater functions), they are not used in HF methods. Instead, the atomic orbitals are expanded through a linear combination of the Gaussian functions, which are proportional to $exp[-\alpha(r-R_0)^2]$. In this function R_o is the position of the atomic nucleus around which the orbital is located and α is chosen such that the shape of the Gaussian function resembles that of Slater function. The basis sets may be “minimal” (i.e., one basis function per atomic orbital), “split valence” (two basis functions per valence atomic orbital, one per core orbital), or higher zeta (where *n*-zeta means *n* basis functions per orbital). Multiple basis functions per atomic orbital allow the size of the orbitals to increase (i.e. along a bond axis) or decrease (i.e. perpendicular to a bond axis). The higher-order basis sets may also be augmented with polarization functions (e.g. one or more sets of d functions on first row atoms). These functions describe small displacements of the orbitals from atomic centers in the molecular environment, and diffuse functions for anions and Rydberg excited states. The size of the

Hamiltonian to be diagonalized is proportional to N^3 (where N is the number of AOs); therefore, the use of large basis sets is very time-consuming.

Using pseudopotentials, effective core potentials (ECP's) within the framework of an *ab initio* method, significantly simplifies its mathematical implementation for heavier elements (3rd row and below) of the periodic table. When pseudopotentials are used, the core electrons are not treated explicitly, but as a collective (e.g. average) effect. Hence, many calculations such as individual core electron-electron interactions integrals are eliminated from the process. Only the valence electrons need to be treated explicitly. This means fewer calculations, thus less computing time for such heavy atoms.

2.2 Density Functional Theory

Density functional theory, a computational method that focuses on the electron density as the carrier of all the information in the molecular (or atomic) ground state, has gained a great deal of popularity in quantum chemistry. DFT seeks to determine the exact ground state energy using electron density (an actual physical property of the matter), directly, without computing a many-electron wave function. The electron density is a function with three variables, x-, y-, z-position of the electrons; it is independent of the number of electrons, unlike the wave function that is a function of the number of electrons. For this reason wave function approach becomes significantly complicated as the number of electrons increases. Therefore the complexity of the problem with DFT is tremendously reduced compared to the conventional wave function approach [3, 5-6]. The most significant advantage to DFT methods is the significant increase in

computational accuracy without the additional increase in computing time. In most DFT methods, the computational cost scales as the third power of number of electrons. This is large, but much smaller than, for example, the power of 4 required by HF, and 5, 6, or 7 by post-HF methods. Hartree-Fock, Hartree-Fock limit, and post-Hartree-Fock methods are described in the next section.

2.2.1 Hartree-Fock Approximation, Hartree-Fock Limit and Post Hartee-Fock Method

As a first approximation, to solve the Schrödinger equation, a single form for Ψ is defined. The Hartree-Fock approximation is one such method where the function of *4N* variables are reduced to *N* functions, which are referenced as atomic or molecular orbitals (MOs), each dependent on 4 variables. Each orbital describes the probability of a single electron moving in the average field of all other electrons. Due to the requirements of antisymmetry, with respect to interchange of any two electrons, and indistinguishability of electrons, the trial wave function is a single determinantal wave function of the orbitals, called a Slater determinant. One such antisymmetric determinant is the wave function for the $1s^2$ singlet state of the He atom (Eq. 2.5) [7].

$$\Psi = \frac{1}{\sqrt{2}} \begin{vmatrix} 1s(1)\alpha(1) & 1s(1)\beta(1) \\ 1s(1)\alpha(1) & 1s(1)\beta(1) \end{vmatrix} \tag{2.5}$$

In the wave function above, which is written in terms of known atomic orbitals (s, p, d, f,..), *1s(1)* is the molecular orbital (the space function) associated with electron 1 and *α(1)*

is the spin coordinate of electron 1 (*1s(1)α(1)* is a spin orbital).

In the HF method, the optimum MO's are determined through variationally minimizing molecular energy, *E*. The variational principle states that for any trial function Ψ:

$$\int \Psi_0 \hat{H} \Psi_0 \, d\tau \geq \int \Psi \hat{H} \Psi \, d\tau \qquad \rightarrow \quad E[\Psi_0] \leq E[\Psi] \tag{2.6}$$

The energy computed from a guessed Ψ (the true wave function), is an upper bound to the true ground state energy E_0. Full minimization of the functional $E[\Psi]$ with respect to all allowed *N*-electrons wave functions will give the true Hartree-Fock ground state, Ψ_0, and energy $E[\Psi_0]=E_0$ [7-8].

The interelectronic repulsions, mathematically, are treated such that each electron experiences the average electrostatic repulsion of a charge cloud created by all the electrons within the HF method. There is no particular position for electrons in the molecule at any point of time. Their positions instead are defined by the probability distribution that causes a mean electric field that applies a force to each electron. Thus HF method is a mean field method applied to a many-electron problem, the solution to which is known as the self consistent field (SCF theory indicates that in a system of *N* electrons, each electron interacts with a mean potential created by the entire system, rather than with the other *N*-1 electrons) [9]. This does not portray a precise picture of what actually happens, that is each immediate pair-wise interactions between each

electron and all remaining electrons in the molecule, is felt by that electron. Based on this the interelectronic repulsion is overestimated by HF since electrons actually avoid each other more than what HF allows. This overestimation is referred to as electron correlation, and the difference between a molecule's actual energy and the lowest possible HF energy is known as the correlation energy. The HF calculations always converge to an energy that is greater than the true energy, regardless of the accuracy of the basis used. This calculated energy is known as the HF limit [7-8].

As discussed above the HF theory does not include details of the instantaneous electron-electron correlations, hence, several post-HF techniques have been developed, including many-body (Møller-Plesset) perturbation theory [10], and configuration interaction (CI) [11].

In the former a mathematical technique provides 1^{st}, 2^{nd} and higher order corrections to the known "zero order" ground state wave function. This wave function is constructed form the HF MOs, making up for the difference between the sum of HF operators and the exact Hamiltonian. There are different versions of this method with progressively higher levels of accuracy and longer computational times as higher-order corrections are computed for the unperturbed system. In CI methods, electron-pair correlations are treated self-consistently assuming the wave function is a linear combination of the HF determinant.

2.2.2 Hohenberg-Kohn Theorems and Kohn-Sham Approach

DFT relies on two fundamental theorems. The first is the Hohnberg-Kohn (1964) [12] theorem, stating that the ground-state electron density, $\rho_0(r)$, uniquely determines the ground state energy and all ground state properties (Equations 2.7 and 2.8) [5-6, 12] Otherwise stated, the energy is a functional of the electronic density function $\rho(r)$.

$$E(\rho(r)) = \int v(r)\rho(r)dr + F(\rho(r)) \quad (2.7)$$

$$F(\rho(r)) = E_{ki}\,(\rho(r)) + E_{col}\,(\rho(r)) + E_{xc}\,(\rho(r)) \quad (2.8)$$

In the above equations, $v(r)$ is the external potential, $E_{ki}(\rho(r))$ is the kinetic energy, $E_{col}(\rho(r))$ is the classical Columbic repulsion energy, and $E_{xc}(\rho(r))$ is the exchange-correlation energy. The second part of the Hohnberg-Kohn theorem states that the energy functional will yield a higher energy for any density $\rho(r)$, other than the true ground state density. The energy functional is variational (Eq. 2.9) [6, 13].

$$E(\rho(r)) \geq E(\rho_0(r)) \quad (2.9)$$

The Kohn-Sham (KS) (1965) [13] approach provides a way to determine approximate $\rho(r)s$. The challenge in DFT is the design of accurate functionals, specifically the kinetic and the exchange-correlation (XC) energies density functionals. The exchange correlation energy functional is not known and because there is no accurate kinetic energy functional available at this point, a good kinetic energy estimation is obtained by the introduction of KS orbitals in the KS method. This is done by expressing the density as a function of the

KS orbitals, θ_i^{KS} (Eq. 2.10). The difference between the true kinetic energy and the kinetic energy calculated from the KS orbitals is displaced to the exchange-correlation functional. Based on Equation 2.8, the sum of the square of the occupied KS orbitals is the true density of the system. This is why KS orbitals are different from other kinds of orbitals, for which a similar sum is only an approximated density in other quantum mechanical methods such as HF [5-6].

$$\rho(r) = \sum_i^N | \theta_i^{KS} |^2 \qquad (2.10)$$

In Equation 2.10, N is the number of the electrons. The ground state energy can be found by varying $\rho(r)$ to minimize the functional $E(\rho(r))$, or equivalently by varying the KS orbitals. As mentioned earlier, the exchange-correlation energy is not known and cannot be calculated exactly, hence approximations need to be made for its calculation. The local density approximation (LDA) and generalized gradient approximation (GGA) are two such approximations. LDA methods assume that each point has an XC potential identical to that of a homogeneous electron gas of the same density [14] (electron density attains a constant value everywhere in the system). This method is a fairly good model for simple metals such as sodium. GGA methods on the other hand, account for the non-uniformity of the electron density by importing derivatives of the density into the energy functional [14]. Hybrid methods attempt to incorporate some of the more useful features from *ab initio* methods (specifically Hartree-Fock methods) with some of the improvements of DFT mathematics. Hybrid methods such as B3LYP are used to calculate the exchange correlation energy. B3LYP is a parametric functional (with 3

parameters) in which the HF exchange energy is introduced into DFT. Three parameters have been used in B3LYP to give satisfactory results compared to the experimental results in many cases [15].

2.2.3 Common DFT Basis-Sets: Localized versus Delocalized

The ground state energy is obtained as a solution of constrained minimization of the Kohn-Sham energy. The electron density (the bases for DFT) is made up from one electron orbital in Kohn-Sham DFT. A linear expansion is used to expand the Kohn-Sham molecular orbitals using a set of basis functions (Eq. 2.11). A thorough description of most common, localized and delocalized basis functions is provided below [14, 16].

Commonly used basis sets are atomic localized basis sets constructed from linear combination of atomic orbitals. The popularity of localized basis sets are due to: being efficient, fast convergency with respect to the basis set size (just a few functions per atom is needed), well describes finite systems (e.g. atoms with few orbitals) and all-electron solution (core region is included in the calculation). However there are disadvantages to using localized basis sets, among which are the followings: expensive to use, centered on atomic nuclei and dependent on atomic position, difficult to evaluate the convergence quality (no systematic way to improve convergence), basis set superposition error, very difficult to optimize the many parameters involved, requirement of different basis set for molecules and solids [14, 16].

In contrast to localized basis sets, planewaves (PWs) are simple delocalized basis sets

with many advantages that make them well suited to solve the Kohn-Sham equations, particularly extended systems using very efficient numerical schemes. Planewaves are orthonormal. They are not biased to any particular atom, any region in space is treated on an equal footing so that the calculations do not have to be corrected for a basis set superposition error (i.e. numerically efficient). Since PWs do not depend on the positions of the atoms, the Hellmann-Feynman theorem [17-18] can be applied directly to calculate atomic forces (no Pulay forces [19]) even for a non-complete basis set (hence less expensive). Systematic convergence is achieved with respect to a single parameter, cutoff energy (E_{cutoff}), i.e. only PWs with a kinetic energy less than the cutoff energy are included in the calculations. Therefore, the convergence of the calculations with respect to the basis set size can be controlled and improved by increasing the cutoff energy. Furthermore Fast Fourier Transforms (FFT) can be used for transformation between real and reciprocal space, therefore calculations scale up with $N_{pw}ln(N_{pw})$ (where N_{pw} is the number of planewaves), nearly linear with number of functions versus N^2 for DFT with localized basis set [15-16].

Despite the many advantages of PW basis sets, there are two main disadvantages: 1) due to the nodal structure of the valence wave functions in the core region of the atoms a prohibitively large number of PWs would be needed for a good representation of these fast oscillations. This also means a large PW cutoff energy is required to represent the core features efficiently, 2) Large supercells are required to give a reasonable description of physical properties of finite systems. Introducing pseudopotentials can assist in overcoming these shortcomings [14-16].

In the next section the mathematical representation of the planewaves function and more detailed explanations of how introducing pseudopotentials and *k*-points assist in overcoming the shortcoming of PW basis sets, are provided.

2.2.4 Pseudopotential Planewaves, Supercells and *k-point* Sampling

One of the most widely used methods for calculating ground state properties of extended systems within the framework of DFT is the pseudopotential planewave approach. Using pseudopotentials guarantees that the wave functions can be expanded in a relatively small set of PWs. By introducing pseudopotentials to PW approaches, two main goals are achieved. First, core electrons are removed from the calculations. Core electrons do not contribute much (negligible) to chemical bonding but their contribution is most to the total energy of the system. By removing the core electrons from the calculations, total energy differences between ionic configurations are the differences of much smaller numbers. This leads to a much less demanding required accuracy for the total energy calculations than in all-electron calculations. Second, by employing pseudopotentials the true valence wave functions are replaced by pseudo wave functions. These functions match the true valence wave functions exactly outside the ionic core region, and are nodeless inside. Pseudo wave functions can be expended using a much smaller number of PW basis sets compared to all-electron systems [20-21].

The linear expansion of Kohn-Sham molecular orbital using a set of PW basis functions is shown in Equation 2.11. In this equation $\varphi_j(r)$ is the planewave basis function, and $C_{j\alpha}$ is a constant. Equation 2.12 shows the PW basis set function where *i* is

the imaginary unit, G is the reciprocal lattice vector and r represents the point in space where the function is evaluated at, and N is the normalization constant [20-21].

$$\Psi_{\alpha}(r) = \sum_{j=1}^{K} C_{j\alpha}\,\varphi_j(r) \tag{2.11}$$

$$\varphi_j(r) = N e^{i\boldsymbol{G}\cdot r} \tag{2.12}$$

Although pseudopotential PWs simplify the many-body (all-electron system) problem the calculation is still a difficult task. For simplicity the system of interest is assumed to be a lattice of atoms in which the lattice points are periodically repeated. This lattice is called the "Direct Lattice" or "Bravais Lattice" and is defined by a set of primitive translation vectors (vectors are shown in bold), $\boldsymbol{a_1}$, $\boldsymbol{a_2}$, and $\boldsymbol{a_3}$. In Equation 2.13 "$\boldsymbol{h}$" denotes the direct lattice vector space. All points are represented with the position vector $\boldsymbol{T}$ in the direct lattice (Eq. 2.14). n_1, n_2, and n_3 are integers. The volume Ω of the lattice is defined by Equation 2.15 [22-23].

$$\boldsymbol{h} = [\boldsymbol{a_1}, \boldsymbol{a_2}, \boldsymbol{a_3}] \tag{2.13}$$

$$\boldsymbol{T} = n_1\boldsymbol{a_1} + n_2\boldsymbol{a_2} + n_3\boldsymbol{a_3} \tag{2.14}$$

$$\Omega = \boldsymbol{a_1} \cdot (\boldsymbol{a_2} \times \boldsymbol{a_3}) \tag{2.15}$$

This lattice can be as small as the unit cell or a large supercell containing a sufficient number of independent atoms to represent the solid. It is essential to make the supercell large enough to prevent molecules in neighbouring cells from interacting appreciably with each other. The independence of the configurations can be checked systematically

by increasing the volume of the supercell until the computed quantity of interest converges. On this basis it can be seen that the number of the plane waves depends on not only the cutoff energy but on the volume of the cell, Ω [22-23].

For every direct lattice there is reciprocal lattice $\boldsymbol{G}$, represented by a set primitive reciprocal lattice vectors, e.g. $\boldsymbol{b_1}$, $\boldsymbol{b_2}$ and $\boldsymbol{b_3}$. Equation 2.16 and 2.17 [22-24] represent the reciprocal lattice and the lattice vectors in it, respectively. The relationship between the primitive (unit) vectors in the direct lattice and the reciprocal lattice are shown in Equation set 2.18-2.20 [22-24].

$$2\pi(\boldsymbol{h}^t)^{-1} = [\boldsymbol{b}_1, \boldsymbol{b}_2, \boldsymbol{b}_3] \quad (2.16)$$

$$\boldsymbol{G} = n_1\boldsymbol{b}_1 + n_2\boldsymbol{b}_2 + n_3\boldsymbol{b}_3 \quad (2.17)$$

$$\boldsymbol{b}_1 = (\boldsymbol{a}_2 \times \boldsymbol{a}_3)/[\,\boldsymbol{a}_1 \cdot (\boldsymbol{a}_2 \times \boldsymbol{a}_3)] \quad (2.18)$$

$$\boldsymbol{b}_2 = (\boldsymbol{a}_3 \times \boldsymbol{a}_1)/[\,\boldsymbol{a}_2 \cdot (\boldsymbol{a}_3 \times \boldsymbol{a}_1)] \quad (2.19)$$

$$\boldsymbol{b}_3 = (\boldsymbol{a}_1 \times \boldsymbol{a}_2)/[\,\boldsymbol{a}_3 \cdot (\boldsymbol{a}_1 \times \boldsymbol{a}_2)] \quad (2.20)$$

Furthermore a PW function of the form $f(r) = exp(i\boldsymbol{k}\cdot\boldsymbol{r})$ in the direct lattice, where k is an arbitrary fixed vector, can only have the same periodicity of the simulation cell with direct lattice vectors T, if $exp(i\boldsymbol{k}\cdot\boldsymbol{T})$ is equal to 1. This is true only if vectors k belong to the reciprocal lattice G as defined above. In any direct lattice there is an area around a lattice point that is closer to that point than any other lattice point. This region is called Wigner-Seitz (WS) [23] cell the shape of which is defined by the geometry of the unit

cell. The same region of the reciprocal lattice is called Brillouin Zone (BZ) [22-26], this zone is the origin of set of special points called *k*-points [22-26].

The transitional symmetry of the atomic arrangement in a periodic system can be used to reduce the computational cost for solving the Kohn-Sham equation. In a periodic system where the atoms are arranged in a periodically repeating pattern, the potential acting on the electrons and the electron density are periodic (Equation 2.21) [23]. Since the density is equal to the magnitude of the wave function, this magnitude is also periodic. However this does not mean that the wave function is also periodic because their phase factor can be anything.

$$V(\boldsymbol{r} + \boldsymbol{T}) = V(\boldsymbol{r}) \;\rightarrow\; \rho(\boldsymbol{r}+\boldsymbol{T}) = \rho(\boldsymbol{r}) \tag{2.21}$$

Based on Bloch's theorem [23] for the wave function at any point in the direct lattice, translated by lattice vector *T*, there is a vector $\boldsymbol{k}$ that provides the condition to allow the periodicity of the wave function as seen in Equation 2.22. Hence, in order for the wave function to be periodic, the phase factor, $exp(i\boldsymbol{k}\cdot\boldsymbol{T})$ must be selected in a systematic way such that it is unitless. Therefore, since $\boldsymbol{T}$ is the vector in the direct lattice, $\boldsymbol{k}$ can only belong to the reciprocal lattice.

$$\Psi_{\alpha}(\boldsymbol{r} + \boldsymbol{T}) = e^{i\boldsymbol{k}\cdot\boldsymbol{T}}\, \Psi_{\alpha}(\boldsymbol{r}) \tag{2.22}$$

The only valid $\boldsymbol{k}$ vectors that satisfy the Bloch's theorem are in the BZ of the reciproc-

al lattice. All the calculated properties of the total periodic wave functions are averages over the BZ, i.e. these properties are calculated at the all selected *k*-points and then averaged to provide the final quantity. Therefore, increasing the number of *k*-points provides a better average, hence, more accurate results. But this also increases the cost of the calculation. To resolve this problem using the symmetry of the BZ, all the points that are symmetrically equivalent are avoided, so the set of many *k*-points of the BZ are reduced to a much smaller set containing only the unique *k*-points. The part of BZ that includes these unique *k*-points is called irreducible Brillouin Zone (IBZ) [22-24].

Any smooth function can be numerically integrated with a suitable grid points and weights. Monkhorst-Pack [24] method is a simple and one of the most common methods for generating k-points and weights. This method is presented in Equations 2.23 and 2.24 [24].

$$\boldsymbol{K}_{prs} = u_p \boldsymbol{b}_1 + u_r \boldsymbol{b}_2 + u_s \boldsymbol{b}_3 \tag{2.23}$$

$$u_r = (2r - q_r - 1)/2q_r \quad where \quad r = 1,2,\ldots, q_r \tag{2.24}$$

where $\boldsymbol{b}_i$ is the reciprocal lattice primitive vectors, u_r, u_p and u_s are integers in *r*, *p* and *s* directions respectively, and q_r determines the number of *k*-pints in *r* direction [22-24].

2.2.5 Slab versus Cluster Calculations

Slab computations and cluster models are two commonly used approaches for determining surface properties. The main difference between surface methods is the bou-

ndary condition(s) used to model the surface.

The slab models treat the surface to be infinite and periodic in two dimensions parallel to the surface, with finite thickness in the third dimension (perpendicular to the surface). In slab computations a finite number of atomic layers (thickness), periodic within the layer, is used to model the surface. Slabs have two surfaces, top and bottom that are symmetry equivalent. Because of theses surfaces, the computed surface properties are converged, when the addition of layers at the center of the slab does not affect the results. The slab thickness is a critical parameter for determining the surface properties. The minimum of this thickness is defined as the number of the layers needed to make the surface states (states for which the electron density is localized at the surface), on the top and bottom surfaces, non-interacting. This critical thickness is different for different surface properties, since not all properties converge at the same rate. The equilibrium surface structures are computed by relaxing the atoms in the vicinity of the surface. This means that the forces on each atom from the potential are computed, then the atoms are moved in such way that the forces are minimized. This process may include only the atoms on the top few layers or every atom in the slab, depending on the complexity of the potential [27].

The cluster methods model is the surface with a finite cluster (set) of atoms with no periodic boundary conditions. The advantage of this approach is that due to absence of translational symmetry (i.e. having a finite system), the computation is greatly simplified and *ab initio* quantum-chemical potentials for which computer codes already exist could

be used. However, there are disadvantages to this approach including the presence of the edge effects (i.e. effects resulting from the termination of the cluster edges) that makes the examination of the surface electronic structure nearly impossible [27].

In this research all quantum chemical computations were performed using periodic (slab model) Kohn-Sham density functional theory (DFT). The GGA method was used as the exchange correlation functional type, with the Becke, Lee, Yang, Parr (BLYP) parameterization. The program default basis set, a double-ζ polarization set composed of a compact and a diffused orbital basis, was used in these calculations.

2.2.6 DFT Applications and Available Programs

DFT is a general-purpose method. Like all computational methods it is more useful for some types of calculations than others and unlike *ab initio* methods (e.g. HF method) it can be used for calculations involving metals.

DFT methods are now standard in virtually all of the most popular QM software packages. They can be categorized into three groups, DFT periodic codes, DFT molecular codes and DFT atomic pseudopotential codes. QUEST, SIESTA, and VASP mainly belong to DFT periodic; Gaussian, GAMESS, QCHEM, and NWChem principally belong to DFT molecular; USSP and ADPACK belong to DFT atomic pseudopotential codes. A calculation can be customized to include advanced DFT methods such as time-dependent DFT for determination of excited states [16, 28].

2.3 SIESTA

The steady increase in computer power and the progress in methodology have allowed the study of increasingly more complex and larger systems. The scaling of the computation time with the system size for most software is poor. Even for efficient DFT based codes computation time increases with N^{2-3} where N is the number of atoms in the system [29]. This makes it very difficult to reach system sizes larger than few hundreds of atoms. This problem stimulated the first ideas [30] for developing schemes to reduce the computational time and memory to linear scaling and has been the subject of important efforts for the past 4 decades. SIESTA is one such program. It was developed initially in 1995 [31-32]. SIESTA is a method and a computer program that performs electronic structure calculations and *ab initio* molecular dynamics simulations of molecules and solids [33]. A comprehensive overview of the operation and characteristics of SIESTA has been given by Ordejon and co-workers [31, 33-34].

SIESTA is used in this research as a tool to perform all the QM DFT calculations and it was chosen because its DFT calculation time scales linearly (for sufficiently large systems) with the number of atoms in the system. Also the fact that it is open source software is an advantage.

2.3.1 Atom program: All-electron versus Pseudopotential Generation

As appears from the name, the Atom program, initially written in 1980 [35], is a program used to perform atomic calculations. It has had some substantial structural

changes over the years. It is currently a tool in SIESTA software. This program is capable of the following:

- All-electron DFT atomic calculations for arbitrary atomic electronic configurations
- Atomic calculations in which the effect of the core is represented by a previously generated pseudopotential (the results from which, for a valence complex, can be compared to the all-electron results to assess its validity)

The all-electron method, accounts for all the electrons individually including the core electrons. In contrast, the pseudopotential represents the effects of all the core electrons as a single entity [35].

Pseudopotentials for a number of atoms were generated previously, and are implemented in the SIESTA program. If the pseudopotential for a desired atom does not exist in SIESTA, the user can generate it through a simple, user friendly procedure [35]. Table 2.1 is an example of pseudopotential input file for the ground state of nickel atom that was developed for this work.

Details of the example in Table 2.1 are explained as follows. The symbol “pg” in the first line is the calculation code and stands for pseudopotential generation. It is followed by the title for the job that is the atom name in this case. In the second line, “tm2” is an acronym for, Improved Troullier-Martins (Original Troullier-Martins type [36]). It is the “flavor” or the generation scheme. The number “3.00” is the radius at which the

logarithmic derivatives are computed for test purposes. The third line shows the atomic symbol Ni and the exchange correlation type which is normally identified by the initials of the author(s)' name. In this example "pb" indicates use of PBE scheme by Perdew,

Table 2.1: Nickel pseudopotential input file

```
------------------------------------------------------------
 pg       Nickel
      tm2   3.0
 Ni    pb
      0.0       0.0       0.0       0.0       0.0       0.0
  5    4
  4    0     2.00     0.00
  4    1     0.00     0.00
  3    2     8.00     0.00
  4    3     0.00     0.00
 3.34     3.34     3.34     3.34
------------------------------------------------------------
```

Burke and Ernzerhof [37]. The fourth line is a series of "0.0"s which is used for esoteric reasons [35]. In the fifth line, "5" represents the number of core orbitals (2s, 2p, 3s and 3p) and "4" represents the number of valence orbitals (*4s, 4p, 3d, 4f*). The next four lines will be described in terms of columns. The first column (starting under the "5", number of core orbitals) represents the principle quantum numbers, n, for the valence orbitals. For example n=4, represents the fourth level orbitals (for example *4s*) in the atom. The second column represents the angular momentum quantum numbers (for example "0" represents the "s" orbital and "1" represents the "p" orbital). The third column provides the number of electrons in a particular valence orbital, specified by the angular momentum quantum number in the previous column. The fourth column provides the spin polarization information in an excited state of the atom. In the above example, this

column contains all zeros because nickel is in the ground state and there is no spin polarization. In summary, the line "4 0 2.00 0.00" represents the *4s* orbital with two electrons ($4s^2$) and no spin polarization. Finally the last line in the oxygen input file represents the set of core radii, "r_c" (r_c =3.34 for nickel), one for each valence orbital. All the input values are very much position dependent. The above input data values must be located in specific columns that correspond to the input data format [35].

The pseudopotentials for carbon, oxygen, and hydrogen were previously generated and available in the software, however, the pseudopotentials for all the metals used in this research were generated using the ATOM program. For all cases the PBE exchange correlation was used for the generation of the electronic configuration, and the tm2 method was used to generate the pseudopotential files for the metals in their non-polarized ground state electron configurations. A particular core radius, r_c, needed to be specified for the pseudopotential input file of each metal. This was done by trial and error in each case. If an r_c initial value was too small ($\leq$ 1.5 for metals used in this study), the pseudopotential could not be generated. After an r_c trial value slightly greater than the minimum acceptable value had been specified, the software would generate an exact r_c value. This r_c value was then used as the r_c for that particular metal atom to generate a valid pseudopotential. The pseudopotential output file was the one used for all the computations that included that particular metal atom.

2.3.2 Molecular Input File: Molecules and Molecules on Metal Surfaces

Creating an input file, like pseudopotential generation, for a molecule or a system con-

sisting of a molecule adsorbed on a metal surface is not a difficult task for smaller molecules or smaller systems. However it becomes more difficult as the number of atoms in the system increases. Nevertheless, SIESTA provides a very user friendly and straight forward procedure that can be used to build the desired system.

The input file for a desired system is written in flexible data format (FDF) that allows the data input to appear in any order. It contains all the necessary physical data for the system and the parameters for the simulations (specified by the user) that need to be performed. The information for each FDF category (tag) in this input format is either specified by the user or is the default value assigned by SIESTA. There are only four mandatory tags that must be specified by the user and more than 194 optional tags for which SIESTA has default values if not specified by the user

The mandatory categories are, “Number of Species”, “Number of Atoms”, “Chemical Species Label”, and “Atomic Coordinate and Atomic Species” or “Zmatrix” [33]. “Atomic Coordinate and Atomic Species” and “Zmatrix” are two different formats for specifying the geometry of the system by inputting the information about the position of each atom in the system. The “Zmatrix” format is more detailed and it is easier to use in some cases. An example of an optional tag is “NetCharge”, where if it is not specified by the user, SIESTA will assign the value of “0.0” for it. A “0.0” value represents a neutral system with a net charge of zero [21].

Table 2.2 shows an example input file that was developed in this work for propane on

the nickel slab of 36 nickel atoms using the "Zmatrix" format. In this format, every line provides certain information required for running the program. A detailed description of the information provided in this particular example is given below.

The input file starts with the name and label tags of the system in the first and the second line respectively. The first tag is "SystemName" which could be any name given by the user, normally it identifies the system. Then in the second line, "SystemLabel", is the chemical formula of the molecule or the system, in this case propane on slab of 36 Ni atoms, C_3H_8-Ni_{36}, (case insensitive). The tags in the next two lines, "NumberOfAtoms", and "NumerOfSpecies", stand for exactly what is described by the names. In this case, there are 47 [(3C+8H) +36Ni] and 3 (C, H, Ni) atoms. The fifth line, "MD.TypeOfRun", stands for type of molecular dynamics (MD) run. It specifies the method used for coordinate and structural optimization. Conjugate gradient, CG, is the MD type of run used in all calculations in this research. The next line, "MD.NumCGSteps", stands for the maximum number of moves that the conjugate gradient method applies to minimize the system energy. This number was set at 5000 for all calculations, however generally the systems would optimize after several hundreds (<<5000) of CG steps. "MD.MaxForceTol" is the atomic force tolerance in CG coordinate optimization. A value of 0.01 eV/Ang (electron volts per Angstrom) was used for this category in all calculations which means the atomic geometry of each system was considered to be optimized when the maximum force was smaller than this value. The maximum number of self consistent field (SCF) iterations per each time step (each CG step) is identified with "MaxSCFIterations" and it was set to be 30 for all cases. The system is converged if

Table 2.2: FDF input file for propane on slab of 36 Ni atoms

```
SystemName              propane-Nickel 36
SystemLabel              c3h8-ni36
NumberOfAtoms           47
NumberOfSpecies          3
NetCharge                0.0
MD.TypeOfRun             CG
MD.NumCGsteps           5000
MD.MaxForceTol           0.01 ev/Ang
MaxSCFIterations        30
DM.MixingWeight         0.03
DM.NumberPulay          20
DM.Tolerance             0.001
DM.EnergyTolerance      0.001 ev
XC.Functional            GGA
XC.Authors               LYP
ZM.UnitsLength           Ang
ZM.UnitsAngle            deg
LatticeConstant         3.524 Ang

%block LatticeVectors
  3.000  0.000  0.000
  0.000  3.000  0.000
  0.000  0.000 10.000
%endblock LatticeVectors

%block kgrid_Monkhorst_Pack
  4  0  0  0.5
  0  4  0  0.5
  0  0  4  0.5
%endblock kgrid_Monkhorst_Pack

%block ChemicalSpeciesLabel
 1   6  C
 2   1  H
 3 28  Ni
%endblock ChemicalSpeciesLabel

%block Zmatrix
molecule
 3  0  0  0   5.286  7.048  1.762   1 1 1
 1  1  0  0   2.100  10.12  0.002   1 1 1
 1  2  1  0   1.553  121.8  180.0   1 1 1
 1  2  3  1   1.550  109.5  179.8   1 1 1
 2  2  3  4   1.102  109.3  119.7   1 1 1
```

Table 2 continued----------

2	2	3	4	1.200	109.4	-119.8	1	1	1
2	3	2	4	1.101	109.5	60.0	1	1	1
2	3	2	4	1.101	110.7	180.0	1	1	1
2	3	2	4	1.101	109.5	300.0	1	1	1
2	4	2	3	1.101	109.5	60.0	1	1	1
2	4	2	3	1.100	109.5	180.0	1	1	1
2	4	2	3	1.101	109.5	300.0	1	1	1

fractional

3	0.000000	0.000000	0.000000	1	1	1
3	0.000000	0.166667	0.050000	1	1	1
3	0.000000	0.333333	0.000000	1	1	1
3	0.000000	0.500000	0.050000	1	1	1
3	0.000000	0.666667	0.000000	1	1	1
3	0.000000	0.833333	0.050000	1	1	1
3	0.166667	0.000000	0.050000	1	1	1
3	0.166667	0.166667	0.000000	1	1	1
3	0.166667	0.333333	0.050000	1	1	1
3	0.166667	0.500000	0.000000	1	1	1
3	0.166667	0.666667	0.050000	1	1	1
3	0.166667	0.833333	0.000000	1	1	1
3	0.333333	0.000000	0.000000	1	1	1
3	0.333333	0.166667	0.050000	1	1	1
3	0.333333	0.333333	0.000000	1	1	1
3	0.333333	0.500000	0.050000	1	1	1
3	0.333333	0.666667	0.000000	1	1	1
3	0.333333	0.833333	0.050000	1	1	1
3	0.500000	0.000000	0.050000	1	1	1
3	0.500000	0.166667	0.000000	1	1	1
3	0.500000	0.333333	0.050000	1	1	1
3	0.500000	0.500000	0.000000	1	1	1
3	0.500000	0.833333	0.000000	1	1	1
3	0.666667	0.000000	0.000000	1	1	1
3	0.666667	0.166667	0.050000	1	1	1
3	0.666667	0.333333	0.000000	1	1	1
3	0.666667	0.500000	0.050000	1	1	1
3	0.666667	0.666667	0.000000	1	1	1
3	0.666667	0.833333	0.050000	1	1	1
3	0.833333	0.000000	0.050000	1	1	1
3	0.833333	0.166667	0.000000	1	1	1
3	0.833333	0.333333	0.050000	1	1	1
3	0.833333	0.500000	0.000000	1	1	1
3	0.833333	0.666667	0.050000	1	1	1
3	0.833333	0.833333	0.000000	1	1	1

%endblock Zmatrix

---

the number of SCF iterations is less than 30 within each CG step.

The next four tags, “DM.MixingWeight”, “DM.NumberPulay”, “DM.Tolerance” and DM.EnergyTolerance”, set the optimization criteria for the density matrix (DM). As seen in the Table 2.2 the values assigned to these categories in our calculations were 0.03, 20, 0.001 and 0.001 eV respectively. “DM.MixingWeight” is the proportion of the output DM that is used for the density matrix of the next SCF cycle in a linear mixing manner[33]. “DM.NumberPulay” represents Pulay mixing and it controls the Pulay convergence accelerator. Pulay mixing accelerates convergence significantly. In some cases where convergence cannot be reached with linear mixing; it can be reached with Pulay mixing. Self-consistency is considered to have been achieved if the maximum difference between the output and the input on each element of the DM in a SCF cycle is smaller than the “DM.Tolerance” value specified. Finally, “DM.EnergyTolerance” represents the minimum energy convergence criterion. The self-consistency of the DM is achieved when the change in the total energy value between the SCF cycles is less than the value of the “DM.EnergyTolerance”, and the density matrix change criterion is smaller than the “DM.Tolerance” [33].

The categories starting with XC provide the information in regards to exchange correlation functional. The two XC tags used in the above example, “XC.Functional” and “XC.Authors” are exchange correlation functional type and the particular parameterization of the exchange correlation, respectively. The author’s initials are usually used for the latter. Once again, as seen in Table 2.2, GGA and LYP (or BLYP i.e.

Becke, Lee, Yang, Parr) were used for these categories in our computations.

Several tags are used to specify the geometry of the supercell (metal slab and vacuum). The tags, "ZM.UnitLength" and "ZM.UnitAngle", specify length and angle units used in the "Zmatrix". Angstrom (Ang) and degree (deg) are the units used in our calculations. As evident from the name, "LatticeConstant" specifies the lattice constant, in angstroms, of the metal used for the catalyst slab. The matrix block, "LatticeVectors" provides the dimensions of the repeating super cells in the system, in terms of crystal unit cells in each dimension. In the above case, there are three unit cells in each "x" and "y" directions and 10 in the "z" direction. Out of the 10 crystal unit cells in the z-direction, 9 are empty and represent the vacuum layer in the supercell (a distance of 9 times the lattice constant of the metal). This layer defines the distance between the surface of one metal slab in one periodic supercell and the bottom of next metal slab in the next periodic supercell above it.

The matrix block,"kgrid_Monkhorst_Pack", represents the number of Monkhorost-Pack [24] *k*-points that were used. A 4×4×4 (4*4*4/2=32 k-points) Monkhorost-Pack *k*-point mesh was used. The convergence as a function of the number of *k*-points was carefully monitored. Increasing the k-point mesh from 32 k-points to 48 k-points changed the adsorption energies by an insignificant amount (~4×10^{-5} eV or ~8×10^{-3} kJ/mol).

The "ChemicalSpeciesLabel" block provides the information about the atoms in the system. In this block, a number is assigned to each species. This number, the species

(atomic) label and its atomic number are provided in each line for each species (e.g. carbon is species number 1, with atomic number 6).

Finally, the "Zmatrix" block contains all the information about the geometry and the geometry optimization of the system. This block specifies all the positions of the atoms in the system with respect to each other. "Zmatrix" includes either a "molecule" section for any gas phase individual molecule system; or both a "molecule" and a "fractional" section for systems of molecules on a metal surface. In the "molecule" section the position of all the atoms are specified using their bond distances and bond angles between the atoms in the molecule, and dihedral angles between one atom in the molecule (central carbon of propane species), the metal atom directly below it, and the plane of the metal slab surface. The relationships between the atoms are specified using the number assigned to them. The first column in both "molecule" and "fractional" sections lists all the atoms in the system by their assigned number. In the propane-Ni36 system carbon is number 1 (3 carbons), hydrogen is number 2 (8 hydrogens), and nickel is number 3 (36 nickels, 1 in the "molecule" section and 35 in the "fractional" section of the "Zmatrix"). The second, third and fourth columns present the atoms (identified by numbers) for which the atoms in the first column have bond distances and bond angles, and dihedral angles, respectively. The fifth, sixth and seventh columns represent the actual value for bond distances, bond angles and the dihedrals angles, respectively. Finally the last three columns of ones (can alternatively be zeros), represent the optimization criteria for all the bond distances, bond angles and dihedrals angles defined in the previous three columns. In these latter three columns, a value of "0" means that particular parameter is kept fixed

and "1" means that it is relaxed. The "fractional" section of the "Zmatrix" provides all the fractional coordinates (i.e. positions in Cartesian geometry) of the metal atoms in the metal slab. The position of each metal atom can be optimized in three "x", 'y', and "z" directions, using the same "0" for fixed and "1" for relaxed, coding system explained above for the "molecule" section of the "Zmatrix". The program will optimize any of these variables for which a value of "1" is assigned by the user (in the optimization columns) in order to obtain the most stable structure and hence the minimum energy for the system.

2.4 Energy Calculation: Binding Energies and Electronic Energy Barriers

The total electronic energies for the absorbate plus metal slab is $E_{adsorbate+slab}$ and $(E_{adsorbate+slab})_{MIN}$ is the total electronic energy for the configuration of the adsorbate plus metal slab that has the minimum energy, $E_{gadsorbate(gas)}$ is the electronic energy of an isolated adsorbate molecule in the gas phase, and $\boldsymbol{E_{slab}}$ is the electronic energy for a metal slab. All these quantities were calculated using DFT. The adsorption energies, E_{ads}, that is the electronic energy for adsorption of the species on the surface of the metal slab (or heat of adsorption), for each of the intermediates in the propane electro-oxidation reaction steps studied were calculated according to the following Equation (Eq. 2.25).

$$E_{ads} = (E_{adsorbate+slab})_{MIN} - E_{adsorbate(g)} - E_{slab} \qquad (2.25)$$

The activation energies E_{act} or barrier heights for each reaction were obtained from a

series of calculations that were performed by progressively increasing bond distance of the bond that needed to break for the reaction to occur. For example in the dehydrogenation of adsorbed propane ($*C_3H_8$) to form adsorbed propyl ($*C_3H_7$) and adsorbed (*H), several calculations were performed with the C-H bonds of the propane's central-carbon atom being increased from its original gas-phase distance, ~0.1nm, to a distance of 0.37nm. In this example the transition state distance was found to be 0.17nm. The transition state energy (the highest energy point) for each reaction was obtained using this procedure, and then calculated using the following equation (Eq. 2.26)

$$E_{act} = (E_{adsorbate+slab})_{MAX} - (E_{adsorbate+slab})_{MIN} \quad (2.26)$$

where E_{act} is the activation energy (energy barrier), $(E_{adsorbate+slab})_{MAX}$ is the total electronic energy for the reactant molecule(s) on the metal slab at the reaction transition state (maximum adsorbate+slab energy), and $(E_{adsorbate+slab})_{MIN}$ is the total electronic energy of the adsorbed reactant molecule(s) on the metal slab at the initial reaction state (minimum adsorbate+slab energy). Variations in the electrical potential of the slabs were not considered (zero electric field).

2.5 References

[1] Gokhale, A.A., Kandoi, S., Greeley, J.P., Mavrikakis, M., Dumesic J.A.; *Chemical Engineering Science* **2004**, *59*, 4679

[2] Masel, R. I.; *Chemical Kinetics and Catalysis*, J. Wiley & Sons, New York, NY, **2001**

[3] McQuarrie, D.A., Simon, J.D., *Molecular Thermodynamics*, University Science Books, Sausalito, CA, **1999**

[4] Cramer, C. J. *Essentials of Computational Chemistry*, 2nd ed.; J. Wiley, Chichester, UK, **2004**

[5] Gross, E. K. U., Dreizler, R. M. (editors); *Density Functional heory*, Springer, Plenum Press, New York, **1993**

[6] Chermette, H.; *Journal of Computational Chemistr*, **1999**, *20*, 129

[7] Galea, N. M., Knapp, D., Ziegler, T.; *Journal of Catalysis* **2007**, *247*, 20

[8] Ferrin, P., Nilekar, A. U., Greeley, J., Mavrikakis, M., Rossmeisl, J.; *Surface Science* **2008**, *602*, 3424

[9] Cairns, E. J.; *J. Electrochem. Soc.* **1966**, *113*, 1200

[10] Goddard, W. A., Kua, J.; *J. Am. Chem. Soc.* **1999**, *121*, 10928

[11] Christoffersen, E., Liu, P., Ruban, A., Skriver, H. L., and J. K. Nørskov, J. K.; *Journal of Catalysis* **2001**, *199*, 123

[12] Honenberg, P., Kohn, W.; *Physical Review B* **1964**, *136*, B864

[13] Kohn, W., Sham, L.J.; *Physical Review A* **1965**, *140*, A1133

[14] Koch, W.; Holthausen, M. C.; *A Chemist's Guide to Density Functional Theory*, Second Edition; Wiley-VCH Verlag GmbH, New York, **2002**

[15] Parr, R. G., Yang, W.; *Density Functional Theory of Atoms and Molecules*, Oxford University Press, Oxford, **1989**

[16] Jensen, F.; *Introduction to Computational Chemsitry*, Second Edition, J. Wiley & Sons, Ltd; Odense, Denmark; **2007**

[17] Hellmann, H.; *Einführung in die Quantenchemie*; Leipzig: Franz Deuticke, **1937**

[18] Feynman, R. P.; *Phys. Rev.* **1939**, *56*, 340

[19] Pulay, P.; *Mol. Phys*. **1969**, *17*, 197

[20] Denteneer, P. J. H.; Herngen, W. V.; *J. Phys. C: Solid State Phys.* **1985**, *18*, 1427

[21] Pickett, W.; Comput. Phys. Rep. **1989**, *9*, 115

[22] Evarestov, R. A.; Smirnov, V. P.; *Phys. Stat. Sol*. *B* **1983**, *119*, 9-39

[23] Ashcroft, N. W.; Mermin, N. D.; *Solid State Physics*; Saunders College Publishing, Philadelphia, **1976**

[24] Monkhorst, J. H.; Pack, J. D.; *Phys. Rev. B* **1976**, *13*, 5188

[25] Chadi, D. J.; Cohen, M. L.; *Phys. Rev. B* **1973**, *8*, 5747

[26] Baldereschi, A.; *Phys. Rev. B* **1973**, *7*, 5212

[27] Unertl, W. N.; *Physical Structure*, Elsevier Science B.V., Netherlands, **1996**

[28] http://dft.sandia.gov/Quest/DFT_codes.html

[29] Artacho, E., Sanchez-Portal, D., Ordejon, P., Gracia, A., Soler, J. M.; *Phys. Stat. Sol. B* **1999**, *215*, 809

[30] Soler, J. M., Artacho, E., Gale, J. D., Garcia, A., Junquera, J., Ordejon, P., Sanchez-Portal, D.; *J. Phys.: Cond. Matt.* **2002**, *14*, 2745

[31] Ordejon,P., Sanchez-Portal, D., Garcia, A., Artacho, E., Junquera, J., Soler, J. M; *Riken Review* **2000**, *29*, 42

[32] Junquera, J., Paz, O., Sanchez-Portal, D., Artacho, A.; *Physical Review B* **2001**, *64*, 235111

[33] Artacho, E., Gale, J. D., Garcia, A., Junquera, J., Martin, R. M., Ordejon, P., Sanchez-Portal, D., Soler, J. M.; *SIESTA 2.0.2,* Fundacion General University, Madrid, **2008** (http://www.uam.es/siesta)

[34] Ordejon, P.; *Phys. Stat. Sol. B* **2000**, *217*, 335

[35] Garcia, A.; *Atom User Manual*, University of Pais Vasco, Bilbo Spain, **2006** (http://nf.nci.org.au/facilities/software/Siesta/2.0/atom.pdf)

[36] Troullier, N.; Martins, J. L.; *Phys. Rev. B* **1991**, *43*, 1993

[37] Perdew, J. M.; Burke, K. Ernzerhof, M. *Phys. Rev. Lett*. **1996**, *77*, 3865-3868

[38] Hammer, B.; Hansen, L. B., Norskov, J. K.; *Physical Review B*, **1999**, *59*, 7413

CHAPTER 3

Literature Review

Fuel cell research started almost two centuries ago, hence there is an extensive amount of literature on scientific work done on fuel cells that goes back to the early 19 century. In this work the concentration was on the anodic catalyst and the anodic electro-oxidation reaction in DPFCs by means of DFT calculations. The literature reviewed in this section covers only DFT studies done on fuel cell reactions and on fuel cell catalysts regardless of the fuel cell type.

3.1 DFT Studies on Electro-Oxidation Reaction in Fuel Cells: a Review

Density functional theory (DFT) is a quantum mechanical theory that describes the ground state electronic structure of many-body systems, in particular, atoms, molecules and condensed phases. With this theory, the properties of a many-electron system can be determined by using functionals, i.e. functions of other functions which in this case includes the spatially dependent electron density. DFT is among the most versatile methods available to perform quantum mechanical calculations in condensed-matter physics, computational physics, and computational chemistry [1].

Many DFT studies have been performed to describe electrochemical reactions on catalyst surfaces and on the performance of electro-catalysts used in fuel cells. A review of some of these studies (related to our work) is given below. This review covers some

studies on the electro-oxidation reactions of methanol, ethanol, methane, carbon monoxide (the most common byproducts in hydrocarbon and alcohol fuel cells) and hydrogen at the anode, followed by a number of studies on anodic and cathodic metal electrocatalysts in fuel cells.

3.1.1 Anodic Electro-Oxidation of Methanol in DMFC

A series of studies [2-8] on the methanol electro-oxidation reaction, at the anode of DMFC, from 1998-2009 are reviewed here. In general the focus of all these studies was on obtaining the rate limiting step and a mechanism for methanol electro-oxidation by means of energy barriers of the reaction steps involved. DFT was the method for calculation of the energy barriers in all these studies. There are two main possible reaction mechanisms (scheme 1 and 2) for the electro-oxidation of methanol to form CO, on a catalyst surface [5]. Scheme 1 involves C-H bond activation to form the hydroxymethyl ($*CH_2OH$) intermediate and scheme 2 is the result of the breaking of the O-H bond of methanol to form the methoxy ($*CH_3O$) intermediate. The total anodic reaction and the two suggested schemes are [5]:

Scheme 1: $CH_3OH \rightarrow *CH_2OH \rightarrow *CHOH \rightarrow *COH \rightarrow *CO$ (3.1)

Scheme 2: $CH_3OH \rightarrow *CH_3O \rightarrow *CH_2O \rightarrow *CHO \rightarrow *CO$ (3.2)

The total anodic reaction is:

$$CH_3OH(g) + H_2O(l) \rightarrow CO_2 + 6H^+ + 6e^- \quad (3.3)$$

The asterisk symbol indicates that the species is "adsorbed". For example *CO reacts with *OH from water dissociation on the catalyst surface, resulting in CO_2, a proton and an electron. Not all researchers agree on a common scheme for methanol electro-oxidation. During 1999 to 2008 [2-4, 6-8] a number of researchers performed periodic DFT calculations in search of finding a pathway for methanol electro-oxidation on a catalyst (e.g. platinum) surface. They all agreed that the path to form stable *CO occurs via an initial C-H cleavage step to form an adsorbed hydroxymethyl species over a wide range of potential, followed by several dehydrogenation steps to form *CO (Eq. 3.1) [6].

Zaragoza and Salcedo used a pure DFT method with a GGA-B88LYP functional within NWChem software. They demonstrated that the CH_3 fragment is the preferred end group in both methanol and ethanol molecules for the initial dehydrogenation in the presence of Pt [7].

In 2009 Watanabe et al. used different Pt (Pt_4, Pt_8 and Pt_{10}) cluster sizes for methanol anodic reaction in DMFC's. They used a dipped adcluster model (DAM) combined with DFT calculations using a B3LYP functional. All their calculations were performed using the Gaussian 03 suit of programs. They predicted the reaction pathway that starts from O–H bond scission to be more favorable than that starting from C–H bond scission for methanol dehydrogenation on a Pt surface. They presented the path in scheme 2 (Eq. 3.2) as the exact path to *CO [5].

The rate determining step in all the above studies seems to be the first dehydrogentati-

on of methanol in either scheme. Dehydrogenation occurs from the methyl group in Scheme 1 and from OH group in Scheme 2 (Eq. 3.1-3.2).

In 2007 however, Janik et al. [8] suggested a different scheme (Eq. 3.4), to be the rate limiting step in methanol electro-oxidation reaction in DMFC's. They examined this reaction over pure platinum, ruthenium (Ru) and different platinum-ruthenium alloys. They performed periodic plane wave DFT calculations with a GGA-RPBE functional, using the Vienna *ab initio* Software Package (VASP) package. The energy barriers for all the intermediates involved in the electro-oxidation of methanol to *CO (listed below) were calculated [8].

$$CH_3OH \rightarrow *CH_2OH \rightarrow *CHOH \rightarrow *CHO \rightarrow *CO \qquad (3.4)$$

They identified the rate limiting step to be the $*CH_2OH \rightarrow *CHOH$ step which has the greatest activation barrier compared to the other steps. They showed that adsorbed carbon monoxide then will react with *OH to form *COOH and finally CO_2 [8].

3.1.2 Anodic Electro-Oxidation of Ethanol

Interest in direct ethanol fuel cells (DEFCs) has increased, since governments have been subsidizing ethanol production from biomass. Conversion of ethanol to CO_2 at the anode is the key to the DEFCs performance. Like methanol in DMFCs, full oxidation of ethanol at the anode of DEFCs is a challenging process [9-10]. A search for the ideal catalyst that could promote this reaction in order to enhance the DEFCs performance is

ongoing.

In 2008 Wang and Liu [11] examined ethanol electro-oxidation in DEFC by performing periodic DFT calculations using GGA-PBE functional, numerical atomic orbital basis sets and Troullier-Martin norm-conserving pseudopotenitals, using SIESTA software. Based on their DFT calculated adsorption and transition state energies they suggested the following (Eq. 3.5) path for anodic ethanol electro-oxidation on platinum surfaces with different coordination.

$$*CH_3CH_2OH \rightarrow *CH_3CHOH \rightarrow *CH_3COH \text{ (or } *CH_3CHO) \rightarrow *CH_3CO \rightarrow *CH_2CO \rightarrow *CHCO \rightarrow *CH + *CO \quad (3.5)$$

where energy barriers for $*CH_3COH$ and $*CH_3CHO$ production are very close, and the acetyl (*CH3CO) formation via either the dehydrogenation of CH_3CHO or the O-H cleavage of CH_3COH is facile. The last oxidation step of *CO will result in production of CO_2. In addition, Wang and Liu [11] also showed that the above reaction pathway is the most facile (smallest activation barrier) on the Pt surface with lowest coordination (100).

In 2009, Kowal et al. [12] studied an alternative pathway for ethanol electro-oxidation in DEFCs via periodic DFT calculations using a GGA-PBE functional and numerical basis set. They used DMo13 code by Delley [13] to perform the DFT calculations. They synthesized and used a ternary $PtRhSnO_2/C$ (platinum-rhodium deposited on carbon supported tin dioxide) catalyst as the anode. Kowal et al. [12] showed that this electro-

catalyst facilitates the optimal pathway (Eq. 3.6), based on DFT calculated activation energy barriers, to C-C bond breaking in ethanol at room temperature, allowing its predominant oxidation to CO_2.

$$*CH_3CH_2OH \rightarrow *CH_3CH_2O \rightarrow *CH_2CH_2O \rightarrow *CH_2 + *CH_2O \quad (3.6)$$

3.1.3 Anodic Electro-Oxidation of Methane

In 1960's [14-17] the use of hydrocarbons such as methane in aqueous electrolyte fuel cells was studied. It was shown that hydrocarbons were oxidized completely to CO_2 in a fuel cell. However the current densities were small. Methane is one of the hydrocarbons that is most commonly used directly as a fuel by means of internal reforming in solid oxide fuel cells. Its use as a fuel in PEM fuel cells has also been studied. The electro-oxidation of methane at the anode of a fuel cell limits the reaction rate.

In 2007 Galea et al. [18] suggested a mechanism for methane electro-oxidation at the anode in SOFC's. They performed a plane wave DFT calculation with a GGA-PBE [18] functional, on slab geometry, using VASP software. They suggested the following (Eq. 3.7-3.8) as the methane dehydrogenation mechanism (obtained by means of energy barriers).

Steps: $CH_4(g) \rightarrow *CH_3 \rightarrow *CH_2 \rightarrow *CH \rightarrow *C \quad (3.7)$

Overall: $CH_4(g) + 4O^{2-} \leftrightarrow 2H_2O(g) + CO_2(g) + 8e^- \quad (3.8)$

where *C will then react with *O (from water dissociation at the anode) to produce *CO which leaves the catalyst surface as CO(g), reacts with O^{2-} transferred through the electrolyte to produce CO_2(g), water vapor and electrons. They calculated the transition state energy for every C-H bond breaking step and all the adsorption energies on the surface of anodic nickel and anodic copper. They found that the last C-H bond breaking step (*CH→ *C) is the most difficult and hence the rate limiting step on both metals.

Psofogiannakis et al. [19] studied the methane electro-oxidation in direct methane (or direct methane PEM) fuel cells. They performed cluster DFT calculation using B3LYP and PW91 to calculate the electronic energy barriers of surface reactions pertaining to the Bagotzky mechanism, on a 10-atom platinum cluster (anode electro-catalyst). Psofogiannakis et al. [19] also employed frequency analysis and transition state theory to show that methane chemisorption ($CH_4 \rightarrow *CH_3 + *H$) step is the rate limiting step the Bagotzky mechanism. The surface reactions in their work included chemisorption of methane on Pt, dehydrogenation of adsorbed intermediates and oxygenation reactions of adsorbed CHx (x=0,..,3). Their energy barrier based investigation of the Bagotzky mechanism (Figure 3.3) identified Eq. 3.9 as the main pathway in the anodic reaction [20].

.

Main pathway: $CH_4 \rightarrow *CH_3 \rightarrow *CH_2 \rightarrow *CH \rightarrow *CHOH \rightarrow *CHO \rightarrow *CO$ (3.9)

Overall anode reaction: $CH_4 + 2H_2O \rightarrow CO_2 + 8H^+ + 8e^-$ (3.10)

The mechanism for the electro-oxidation of propane in a DPFC used in this study was

an extension of that for the Bagotzky mechanism for methane (Figure 3.1).

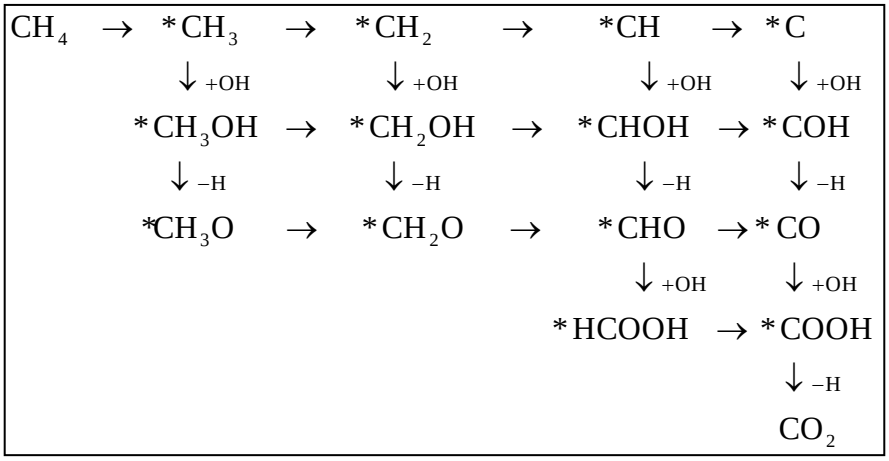

Figure 3.1: The Bagotzky mechanism [20]

3.1.4 Anodic Electro-Oxidation of CO

Carbon monoxide is one of the main intermediates in the electro-oxidation pathway in DMFC's and DHFC's. In addition it is also known to be a contaminant, present in H_2 reformate fuel, used in PEM fuel cells. CO's strong adsorption on the surface of platinum, the most common anodic catalyst in PEM fuel cells, poisons the Pt surface [21], even in the amounts of only about 5-10 ppm. This leads to a significant overpotential that is associated with oxidizing the strongly bonded CO on the electrode surface. By understanding the elementary steps involved in CO electro-oxidation on the surface, it may become possible to address the poisoning problem. Many theoretical studies have attempted to describe these elementary steps. The literature reviewed here concentrates only on energy barrier based density functional theory studies pertaining to PEMFCs.

Janik and Neurock [21] studied the CO oxidation reaction on the Pt anode surface in DMFC's. They performed gradient-corrected DFT calculations with periodic boundary conditions, using VASP software, to compute the potential-dependent reaction energies and activation barriers for this reaction. As a result they proposed a reaction pathway which involves hydroxylation of *CO and dehydrogenation of *COOH (Eq. 3.11), where the first step had the highest activation barrier height and therefore was rate limiting. The alternative pathway that had a much greater barrier height was shown to be the one in Eq. 3.12 that was not favoured.

$$*CO + *OH \rightarrow *COOH \rightarrow CO_2(g) \quad (3.11)$$

$$*CO + *OH \rightarrow *CO + *O \rightarrow *COO \rightarrow CO_2(g) \quad (3.12)$$

They also showed by increasing the electrical potential at the anode, smaller barrier height and hence a lower transition state energy was obtained [21].

In 2007 Janik et al. [8] studied three different compositions of Pt and Ru surfaces and compared them to a pure Pt surface. They carried out the CO oxidation reaction on Pt, a Pt_2Ru monolayer over a Pt substrate, Pt monolayer over a Ru substrate and Pt_2Ru monolayer over Ru substrate. They used the same DFT calculation process as in Janik and Neurock [21] (above). Their results confirmed the above mechanism (Eq. 3.11).

Ferrin et al. [22] also confirmed the reaction pathway shown in Eq. 3.11 for CO oxidation by means of an indirect mechanism with low activation barriers over the

surface of different catalysts in DMFC's. They showed that this mechanism was favoured when Re, Ru, Os, Co or Ni was used as the anodic electro-catalyst. They employed DFT calculations with periodic boundary conditions with GGA-PW91 functional using DACAPO software [22].

3.1.5 Anodic Electro-Oxidation of H_2

The electro-oxidation of H_2 on the anode of fuel cells has been the subject of a number of studies. A brief review of some DFT studies in which the sole interest was predicting a mechanism for the anodic electro-oxidation of H_2 is given in this section.

Mukherjee and Linic [23] studied the H_2 electro-oxidation reaction on the surface of different metals (section 3.2.2), under SOFC operating conditions. They employed a periodic, self consistent DFT calculation, using GGA-PW91 functional. All their calculations were done using DACAPO code. According to their proposed mechanism that was obtained based on the energy barriers of the reaction steps involved, hydrogen from the gas phase dissociates over two vacant sites on a metal, thereby forming two adsorbed H (*H) atoms. Oxygen anions (O^{2-}) from the electrolyte are transferred to the metal thereby forming adsorbed oxygen (*O), and two electrons are transferred to the metal. The *H reacts with *O to form adsorbed hydroxyl (*OH). Finally, *OH and *H react on the metal surface to form water that desorbs into gas-phase, thereby completing the electro-catalytic cycle [23]. It was also demonstrated that the oxygen adsorption energy is a reasonable descriptor for the rate of the electro-catalytic H_2 oxidation over various metals [9].

During the 2005-2006 period Pacheco et al. [24-25] studied the Pt-H_2 interactions relevant to fuel cell anodes. They implemented periodic DFT calculations with a GGA-B3LYP functional and a Moller-Plesset (MP2) calculation via NWchem software. They showed that the physisorption of H_2 molecules on the surface of platinum occurs first, to form Pt-H_2. Then the H-H bond dissociates and an HPtH structure is formed with an HPtH angle of about 90 degrees where one hydrogen is the mirror image of the other, on platinum. All the energies involved in the process were calculated, starting from individual Pt and H_2 species until the H atoms separate and remain bound on the surface of the platinum forming a new product.

3.2 DFT Studies on Electro-Catalysts

3.2.1 Anode Electro-Catalyst

A great amount of effort has been put into research to identify an anodic electro-catalyst with a faster half-cell rate of reaction and hence a higher current density as well as a high CO tolerance. Ferrin et al. [22] examined a wide range of metals including Cu, Ag, Au (group IIB), Re, Ru, Os, Co, Rh, Ir, Ni, Pd and Pt, for anodic methanol electro-oxidation. They used periodic DFT calculations with a GGA-PW91 functional employing DACAPO software. They found that the group IIB metals had good CO tolerance, but very slow anodic reaction rates. They showed that each individual metal would only selectively promote the rate of one or two intermediate reaction steps in the methanol electro-oxidation pathway. Also the CO tolerance using non group IIB metals did not improve significantly compared to platinum. Hence, they concluded that no single pure metal could simultaneously overcome all the reaction problems involved with the anodic

catalyst [22].

In 1999, Kua and Goddard [26] studied the anodic methanol reaction on clusters of six 2^{nd} and 3^{rd} row group VIII transition metals (Pt, Ir, Os, Pd, Rh, Ru) and one Pt-Ru alloy. Non-local DFT calculations with a B3LYP functional were performed. Based on their calculated energy barriers for the reaction steps involved in methanol oxidation, they found that this reaction is the most facile on Pt, while Ir is also favorable. In addition they found that Pt has the least tolerance to CO. Ru and Pt produced opposite results with respect to water dissociation. Ru performed the best providing the smallest barrier height and Pt the poorest with largest barrier height. However the Pt-Ru alloy caused much faster reactions than either of the pure metals. This supports their bifunctional role whereby Pt is responsible for methanol dehydrogenation and Ru is responsible for water dissociation. They also showed that Os exhibits the bifunctionality effect of Pt-Ru [26].

In 2001 Christoffersen [27] did a thorough study of anode materials for low temperature (PAFC, AFC and PEMFC) fuel cells using *ab initio* DFT with RPBE and PW91 functionals. The basis for their study was a competition between H_2 and CO for catalyst sites. They studied a number of pure (single metal) and alloy catalysts, and compared them with pure Pt. They found that a good anode material must bind CO more weakly (i.e. smaller adsorption energy) than pure Pt, but not too weakly, because H_2 surface reaction must be maintained. They showed that since all the transition metals to the left of Pt, bind CO stronger than Pt (hydrogen adsorption has the same trend), changing Pt for any of these metals will only make the CO poisoning worse. Hence, they

considered alloying, to make Pt less reactive (to bind CO less strongly). In particular they showed that a Ru-Pt alloy (with Ru in the bulk) was a superior anode electro-catalyst compared to pure Pt. This finding was attributed to a smaller CO-Pt adsorption energy and therefore more free platinum sites on the surface. On this basis, they claimed that all Pt alloys with Ir, Rh, Ru, Cu, Ni, Co and Fe should have more weakly adsorbed CO and therefore be better anode catalysts [27].

Rossmeisl and Bessler [28] performed periodic DFT calculations with a GGA-RPBE functional to determine the stability of surface-adsorbed *H, *O and *OH (intermediates in the H_2 electro-oxidation pathway) on anodic electro-catalyst metals (Mn, Fe, Co, Ni, Ru, Rh, Pd, Pt, Au) for use in SOFCs. They observed volcano-type behaviour for the adsorption energies of the intermediates on the metal surfaces. They found that 1) Ni had intermediate oxygen adsorption energy and was the best catalyst, 2) The reaction rate decreases for other metals, both for metals with increasing oxygen bonding strength (Ru, Co, Fe, Mn) and for metals with decreasing oxygen binding strength (Rh, Pd, Pt, Au), 3) The stability of *H is not correlated with anode behavior [28].

In their study of H_2 electro-oxidation at the anode of SOFC's [23], Mukherjee and Linic examined a number of metals (W, Mo, Fe, Co, Ir, Ru, Rh, Ni, Cu, Pt, Pd, Ag and Au) as the anodic catalyst using DFT calculations (see details in section 3.1.5). They noted that the reaction rates increase substantially with an increasing anode potential. It was observed that within the low anode overpotential limit (η=0.0 V, ΔV=1.1V), for all metals, the calculated overall anodic reaction rates were very slow. They found that under

this condition the metals to the left of Pt in the periodic table (W, Mo and Fe), that bind oxygen very strongly are better catalysts compared to the other metals. Ir and Ru were shown to be the best catalysts at all conditions, followed by Rh, Ni and Co (Rh>Ni>Co). The general trend is that the rate of electro-oxidation of hydrogen decreases both for metals that are bonded to oxygen either too strongly or too weakly [23].

In 2009 Kowal et al. [12] studied the effect of alloying on the performance of the electrocatalyst used in DEFC. They synthesized a ternary electro-catalyst, $PtRhSnO_2/C$ as the anode of a DEFC that allowed the complete electrooxidation of ethanol to CO_2. Using DFT calculations they compared the ability of $PtRhSnO_2/C$, PtSnO2/C and RhSnO2/C to promote ethanol oxidation in DEFC. They showed that $PtRhSnO_2$ allows C-C bond cleavage through an energetically optimal reaction pathway for ethanol oxidation that is not promoted by either of $PtSnO_2$ or $RhSnO_2$ alloy catalysts. They explained this result was caused by the synergy between the three constituents of the alloy electrocatalyst. According to their findings the role of SnO_2 was to strongly adsorb water while interacting with Pt and Rh on its surface. SnO_2 also provided *OH to oxidize CO at empty Rh sites. Pt and Rh strong interactions on the surface (SnO_2) causes an electron transfer from Rh to Pt, hence, more empty Rh sites become available (than in $RhSnO_2$) for oxidation of oxygen species in the ethanol oxidation process. On the other hand, this causes Pt to interact weakly with ethanol and other dissociated oxygenates, and to become more available for facilitating ethanol dehydrogenation steps. Pt also modifies the electronic structure of Rh allowing it to be able to adsorb ethanol, and other intermediates in the electrooxidation process making a pathway to C-C bond cleavage

and hence making complete ethanol oxidation to CO_2 possible [12].

In 2011 Kelly et al. [29] studied a series of alloy metal-modified tungsten carbide catalysts (M/WC) to investigate a pathway for methanol oxidation reaction in reforming and DMFC applications. They performed periodic DFT calculations with PW91 functional using VASP software to calculate binding energies for species involved in the methanol oxidation process. Based on their combined DFT and experimental results they showed that Rh/WC, Ni/WC and Pt/WC catalysts can effectively promote methanol oxidation.

Following this study, Esposito and Chen [30] also examined the capability of a possible cost effective M/WC catalyst, as a potential anode catalyst in DMFCs (and other similar clean energy technologies) by further modifying the M/WC catalyst used by Kelly et al. [29]. They studied tungsten carbide (WC) having Pt in the top mono layer (ML). Their hypothesis was that the ML of Pt on the WC surface should have electronic and catalytic properties closer to Pt than to WC. It should exhibit catalytic performance comparable but not identical to bulk Pt catalysts while making full use of every Pt atom. Using experimental measurements in combination with the DFT results obtained by Kelly et al. [29], Esposito and Chen [30] showed that the two main challenges in DMFC, (1) the high cost of DMFC electro-catalysts Pt (and Ru), and (2) CO poisoning of Pt, can be overcome by using ML Pt/WC as an alternative to a pure Pt catalyst. This catalyst can be a low-cost alternative to bulk Pt (precious metal) electro-catalysts, since it represents the lower limit of platinum loading which significantly decreases the Pt costs in fuel cells

by over an order of magnitude [30]. Under the DMFC conditions CO adsorbs much more weakly on bulk WC and on the surface ML of Pt-WC. This most likely facilitates the oxidation of CO by surface OH species to produce CO_2, thus increasing the availability of active Pt sites compared to a pure Pt catalyst [30]. This addresses the Pt poisoning problem. Overall Esposito and Chen [30] showed that their hypotheses were true; ML Pt-WC was much less expensive. It was a better anodic catalyst than pure Pt because the complete electro-oxidation of methanol to CO_2 [30] occurred resulting in higher current densities. They also suggested that considering PEMFCs generally face the same two challenges mentioned above for DMFCs, ML Pt-WC could be a suitable candidate to replace commonly used Pt in PEMFCs.

3.2.2 Cathode Electro-Catalyst

DFT calculations with periodic boundary conditions and a GGA-PW91 functional using DACAPO code were performed by Nikolla et al. [31] By means of these calculations they showed that Sn-Ni alloy is much more resistant to carbon poisoning than monometallic Ni when used as the electro-catalyst in catalytic steam reforming of methane, propane and isooctane. This is important in particular for SOFC's with hydrocarbon fuels, since steam reforming is required for conversion of hydrocarbons to hydrogen. Because of its tolerance to carbon poisoning, Sn-Ni alloy was a better catalyst for oxidizing carbon atoms rather than forming C-C bonds [31].

The effect of the catalyst on the oxygen reduction reaction, ORR ($½\ O_2 + 2(H^+ + e^-) \rightarrow H_2O$) at the cathode of fuel cells has been studied; Vukmirovic et al. [32] and Norskov et

al. [33]. Vukmirovic et al. performed self-consistent, DFT calculations with periodic boundary conditions using a GGA-PW91 functional implemented in DACAPO code. They used a new class of ORR electro-catalysts composed of a Pt or a Pt-M (M=Ir, Ru, Rh, Au, Pd, Re, Os) monolayer on the surface of Pd single crystals or carbon supported Pd nanoparticles. They showed that these alloy electro-catalysts (Pd-rich alloys) improve the ORR rate up to 20 fold, compared to pure Pt ORR electro-catalysts. This was mainly due to reduced Pt-OH coverage [32]. Norskov et al. also used DFT with periodic boundary conditions using planewave pseudopotentials, but with a RPBBE functional. They examined a number of Pt and Pd transition metals and analyzed their results by means of a volcano plot. They found that the metals with either stronger (Pt<Ag<Au) or weaker (Co<Ru<Ni<Rh<Ir<Pd<Pt) oxygen bonding than Pt, are poorer oxygen reduction catalysts. Among the metals they examined, Pt and Pd stand out as the metals with smallest overpotential followed by Ir and Rh. They showed that OH bonding energy is also important in determining the surface reaction rate. It is roughly linearly correlated with oxygen bonding for the elemental surfaces discussed above [33].

3.3 A Concluding remark

It is important to note that the results of the studies above cannot really be compared to one another. There are many variations among them. The factors that made these studies different from one another included the type of fuel cell (hence different operating conditions), the fuel types, the catalyst types, the DFT software, the catalyst surface geometry (e. g. slab vs. cluster) and the DFT functionals. One common feature among all these studies is that they all used DFT as the basis of their calculations. That indicates

this method is relied upon and respected among different groups of researchers.

3.4 References

[1] Joubert, D.; *Density Functional: Theory and Application*, Springer-Verlog, Berlin, **1998**

[2] Mavrikakis, M.; Hammer, B.; Norskov, J. K.; *Phys. Rev. Lett.* **1998**, *81*, 2819

[3] Xu, Y.' Mavrikakis, M.; *Surf. Sci*. **2001**, *494*, 131

[4] Greeley, J.' Mavrikakis, M.; *J. Cat.* **2002**, *208*, 291

[5] Watanabe, T.; Ehara, M.; Kuramoto, K.; Nakatsuji, H.; *Surface Science* **2009**, *603*, 641

[6] Cao, D.; Lu G. D.; Wieckowski, A.; Wasileski, S. A.; Neurock, M.; *J. Phys. Chem. B* **2005**, *109*, 11622

[7] Zaragoza, I. P.; Salcedo, R.; Vergara, J.; *J. Mol. Model* **2009**, *15*, 447

[8] Janik, M. J.; Taylor, C. D.; Neurock, M.; *Top. Catal.* **2007**, *46*, 306

[9] Vigier, F.; Rousseau, S.; Coutanceau, C.; Leger, J. M.; Lamy, C. *Top. Catal.* **2006**, *40*, 111

[10] Vigier, F.; Coutanceau, C.; Perrard, A.; Belgsir, E. M.; Lamy, C. *J. Appl. Electrochem.* **2004**, *34*, 439

[11] Wang, H. F.; Liu, Z. P. *J. Am. Chem. Soc.* **2008**, *130*, 10996

[12] Kowal, K.; Li. M.; Shao, M.; Sasaki, K.; Vukmirovic, M. B.; Zhang, J.; Marinkovic, N. S.; liu, P.; Frenkel, A. I.; Adzic, R. R. *Nature Materials* **2009**, *8*, 325

[13] Bradely, D.; *J. Chem. Phys.* **1990**, *92*, 508

[14] Bockris, J. O'M.; Srinivasan, S.; *Fuel Cells: Their Electrochemistry*, McGraw-Hill Inc., New York, **1966**

[15] Grubb, W. T.; Michalske, C. J.; *Nature* (*London*) **1964**, *201*, 287

[16] Cairns, E. J.; *J. Electrochem. Soc.* **1966**, *113*, 1200

[17] Binder, H.; Kohling, A.; Krupp, H.; Richter, K.; Sandstede, G.; *J. Electrochem. Soc.* **1965**, *112*, 355

[18] Galea, N. M.; Knapp, D.; Ziegler, T.; *Journal of Catalysis* **2007**, *247*, 20

[19] Psofogiannakis, G.; St-Amant, A.; Ternan, M.; *J. Phys. Chem. B* **2006**, *110*, 24593

[20] Bagotzky, V. S.; Vassiliev, Y. B.; Khazova, O. A. *J. Electroanal. Chem.* **1977**, *81*, 229

[21] Neurock, M.; Janik, M. J.; *Electrochemica Acta* **2007**, *52*, 5517

[22] Ferrin, P.; Nilekar, A. U.; Greeley, J.; Mavrikakis, M.; Rossmeisl, J.; *Surface Science* **2008**, *602*, 3424

[23] Mukherjee, J.; Linic, S.; *Journal of the Electrochemical Society* **2007**, *154*, B919

[24] Pacheco, J. H.; Bravo, A.; *Revista Mexicana de Fisica* **2006**, *52*, 394

[25] Pacheco, J. H.; Zaragoza, I. P.; Garcıa, L. A.; Bravo, A.; *Revista Mexicana de Fisica* **2005**, *52*, 172

[26] Kua, J.; Goddard, W. A.; *J. Am. Chem. Soc.* **1999**, *121*, 10928

[27] Christoffersen, E.; Liu, P.; Ruban, A.; Skriver, H. L.; and J. K. Nørskov, J. K.; *Journal of Catalysis* **2001**, *199*, 123

[28] Rossmeisl, J.; Bessler, W. G. *Solid State Ionics* **2008**, *178*, 1694

[29] Kelly, T. G.; Stottlemyer, A. L.; Ren, H.; Chen, J. G. *J. Phys. Chem. C* **2011**, *115*, 6644

[30] Esposito, D. V.; Chen, J. G.; *Energy Environ. Sci*. **2011**, *4*, 3900

[31] Nikolla, E.; Schwank, J.; Linic, S.; *Journal of Catalysis* **2007**, *250*, 85

[32] Vukmirovic, M. B.; Zhang, J.; Sasaki, K.; A.U. Nilekar, A. U.; Uribe, F.; Mavrikakis, M.; Adzic, R. R.; *Electrochimica Acta* **2007**, *52*, 2257

[33] Nørskov, J. K.; Rossmeisl, J.; Logadottir, A.; Lindqvist, L.; Kitchin, J. R.; Bligaard, T.; Jonsson, H.; *J. Phys. Chem. B* **2004**, *108*, 17886

CHAPTER 4

A DFT Study of Propane Adsorption on Transition Metal Surfaces: The Initial Step for Propane Oxidation at the Anode of a Direct Propane Fuel Cell

Shadi Vafaeyan, Alain St-Amant, Marten Ternan

Abstract

Because propane or LPG (liquefied petroleum gas) is available in rural locations, it is being seriously considered as the fuel for off-grid fuel cells. The first step in the fuel cell anode reaction, propane adsorption, was investigated using DFT (density functional theory) on metals that are possible candidates for fuel cell anodes, the 3d metals Ni, Fe, Co, Cu, and Zn. The adsorption energies of propane on these metals formed a volcano plot, with Ni being at the peak of the volcano. Two geometric effects were observed. First, the position of adsorbed propane was further from those surfaces having metal atoms of 3-fold symmetry than from those having 4-fold symmetry, probably because the geometrical configuration of the adsorbed propane was different on 3-fold and 4-fold surfaces. Second, for metals of the same surface symmetry, the magnitude of the adsorption energy was inversely proportional to the distance of the adsorbed propane from the metal edge. With the propane-nickel system, the C-H bond on the propane central carbon atom was longer than with the other metals. Ni was identified as a possible

replacement for Pt anodes in fuel cells where there is no water in the liquid phase and corrosion is not expected to be an issue.

4.1 Introduction

Fuel cells convert the chemical energy contained in a fuel into electrical energy. The fuel in most commercial fuel cells is hydrogen. Back-up power (for telecommunications) and materials handling (such as forklifts), are examples of applications that use hydrogen fuel cells. Methanol is the second most common fuel used in fuel cell investigations. Methanol fuel cells are being proposed for portable applications that currently use batteries. In theory conversion of a fuel to electrical energy can be more energy efficient using a fuel cell than using the conventional combinations of thermo-chemical conversion processes (fuel combustion, steam generation, turbine rotation).

Direct hydrocarbon fuel cells (DHFCs) have several advantages over the hydrogen and methanol fuel cells mentioned above. No fuel processing equipment is required to convert a hydrocarbon fuel to hydrogen or methanol. This decreases capital cost. Since hydrocarbon infrastructure (natural gas for stationary applications in urban locations, gasoline or diesel fuel for transportation applications) already exists, unlike hydrogen, new infrastructure for transportation and storage would not be needed, making the capital cost smaller. DHFCs avoid the energy loss caused by the endothermic methane-steam reforming reaction. That has two benefits. The efficiency of transforming the energy in the fuel to electrical energy can be greater for DHFCs compared to hydrogen fuel cells. The absence of methane-steam reforming also decreases the operating costs. Despite their

advantages, DHFCs have one major disadvantage. Their current densities (reaction rates) are much smaller than those in hydrogen or methanol fuel cells.

An extensive amount of research was performed in the 1960's on DHFCs. Three reviews of that work are available [1-3]. More recent work has been of limited extent. There has been considerable interest in feeding hydrocarbons directly to the anodes of solid oxide fuel cells (SOFCs) operating near 1000 K. Gross, Vohs, and Gorte [4] have reviewed that work. Direct hydrocarbon fuel cells operating at 300°C using 1 mm thick $Sn_{0.9}In_{0.1}P_2O_7$ pressed powder electrolytes have been reported [5]. There has been some fundamental work on kinetics and mechanisms [6-9]. Finally there have been a few reports of direct hydrocarbon fuel cells using polymer electrolytes [10-12].

The context of our work is the use of direct propane fuel cells (DPFCs) in rural locations. Propane is the component having the largest concentration in liquefied petroleum gas (LPG). LPG is currently used as a fuel for heating in rural areas, and is available in most rural regions where roads exist. Therefore no additional infrastructure would be required to generate electrical power for a rural fuel cell application. Although the price of electrical power in rural areas is often identical to that in urban areas, the electrical utility company's cost of delivering electrical power in rural areas can be as much as an order of magnitude greater than that in urban areas. As a result a much larger capital cost for fuel cells could be justified in rural areas than in urban areas.

Work in our laboratories has been directed toward understanding DHCFC phenomena

with a view to improving current density. The focus has been on the development of polymer electrolyte fuel cells (PEMFCs) having membrane electrode assemblies (MEAs) that operate at temperatures greater than the boiling point of water. With no water present in the liquid phase corrosion issues should be much less severe. If corrosion rates are sufficiently small then the use of platinum group precious metal electro-catalysts may be avoided again decreasing capital costs. A combination of fuel cell reactor modeling using computational fluid dynamics (CFD) [13-15], fuel cell catalyst modeling using density functional theory (DFT) [16], and experimental work with high temperature polymer-ion-conductor composite electrolytes [17] has been used in our group.

In this work density functional theory, DFT, computations were performed to investigate the 3d transition metals as anode electro-catalysts (possible alternatives to commonly used platinum anode electro-catalysts) in DPFCs. The initial step in the propane reaction network (Equation 4.1) at the anode of a DPFC was studied. Many different DFT studies of various fuel cell reactions have been reported in the literature. Some examples are: the oxygen electro-reduction reaction [18], the hydrogen electro-oxidation reaction in hydrogen fuel cells [19], the electro-reduction reaction in the presence of liquid water [20], and the methanol electro-oxidation reaction in methanol fuel cells [21]. Also, the synergy between computational studies and experimental studies for fuel cells has been described recently [22].

$$C_3H_8(g) + 6\ H_2O(g) \rightarrow 3\ CO_2(g) + 20\ H^+\ (ZrP) + 20\ e^-\ (Me) \qquad (4.1)$$

where ZrP represents a solid zirconium phosphate electrolyte phase and Me represents the solid transition metal electro-catalyst.

More specifically our DFT computations have been performed to determine the adsorption energy of propane on selected non-precious 3d transition metals, Fe, Co, Ni, Cu, and Zn. Although the electro-catalysts in fuel cells operating above the boiling point of water may not need to be corrosion resistant, they do require appropriate adsorption/reaction properties. There are a number of adsorption studies (experimental and computational) for some low-weight hydrocarbons, alkanes (methane & ethane [23-24]), alkenes and alkynes on metal surfaces. However, neither experimental nor computational investigations were found for propane adsorption on nickel, where adsorption energies were investigated.

4.2 Methodology and Computational Details

Quantum chemical computations were performed by employing SIESTA software [25] using Kohn-Sham density functional theory (DFT). The generalized gradient approximation method (GGA) was used as the exchange correlation functional type, with the Becke, Lee, Yang, Parr (BLYP) parameterization. The default basis set, a double-ζ polarization set composed of a compact and a diffused orbital basis, was used in these calculations. The tolerance of the density matrix was set to 10^{-3}. This value sets the limit for achieving the self consistency within each SCF cycle. The default value of 100 Rydberg (1300 eV) was used for the mesh cutoff energy. A 4×4×4 (4*4*4/2=32 k-points) Monkhorost-Pack *k*-point mesh was used. The convergence as a function of the number

of *k*-points was carefully monitored. Increasing the k-point mesh from 32 k-points to 48 k-points changed the adsorption energies by an insignificant amount (about 4×10^{-5} eV or ~8×10^{-3} kJ/mol). In some calculations the atomic coordinates were allowed to relax to determine the geometry having the minimum energy. When the difference in energy between successive calculations was less than 10^{-3} eV, and when the maximum atomic force was less than 0.01 eV/Å, the convergence criteria were attained and the atomic geometry optimized.

Pseudopotentials for all metals were generated using the ATOM program of SIESTA. The Perdew Burke Ernzerhof (PBE) [26] exchange correlation was used for the generation of the electronic configurations. The Improved Troullier-Martins (tm2) method was used to generate the pseudopotential files for all the metals in their non-polarized ground state electron configurations. The pseudopotential input file for each metal required a particular core radius, r_c, to be specified. This was obtained by trial and error. If an r_c initial value was too small ($\leq$ 1.5 bohr for metals used in this study), the pseudopotential could not be generated. After an r_c trial value slightly greater than the minimum acceptable value had been specified, the software would generate an exact r_c value. This r_c value was then used to generate a valid pseudopotential. The pseudopotential output file was the one used for all the computations that included that particular metal atom. The r_c values (generated by the software) for the 3d metals decreased along the row from 3.64 bohr for Fe to 3.08 bohr for Zn, as the atomic number increased.

DFT calculations were performed on a system of periodically repeated entities that were defined in terms of metal crystal unit cells. Each entity consisted of one propane molecule and a slab of metal atoms. The (100) surface was used for all metals. The entities were either a 4×4×10 arrangement for bcc and hcp metal slabs with two atoms per crystal unit cell (4*4*2 = 32 atoms), or a 3×3×10 arrangement for fcc metal slabs with 4 atoms per crystal unit cell (3*3*4 =36 atoms).

The vacuum layer was represented by nine of the 10 crystal unit cells being empty in the z-direction. This layer is defined as the distance from the upper surface of a metal slab within one periodic entity to the bottom surface of the next metal slab above it in the next periodic entity. The vacuum layer is equivalent to 9 crystal unit cells (a distance of 9 times the lattice constant of the metal). Ideally this layer can prevent, or minimize, interactions between the periodic entities in the direction perpendicular to the surface.

Slabs with two-layers of atoms per unit cell were used, with 16 metal atoms in each of the two layers for bcc or hcp metals, and 18 atoms in each of the two layers for fcc metals. The choice of 32 or 36 metal atoms per slab is typical of the number of metal atoms in many DFT slab calculations [27-30]. The fractional surface coverage of propane was less than 0.2 when 16-18 atoms were in one layer of a slab. That avoided both adsorbate-adsorbate interactions and interactions between the adsorbed propane and metal atoms in neighbouring slabs. It has been shown [31] that adsorbate-adsorbate interactions can influence the binding energy by as much as 1 eV when the fractional surface coverage increases from 0.2 to 1. For propane adsorption on Ni(100), increasing

the number of layers from 2 to 4 (increasing the number of atoms from 36 to 72) only changed the value of adsorption energy by 7.3% (~0.04 eV or ~4 kJ/mol). This variation is well within the target accuracy of 0.1 eV for functionals [32]. The small change in binding energy (0.04 eV) caused by increasing the slab layers from 2 to 4 suggests that neither adsorbate-adsorbate interactions nor interactions between the adsorbed propane and metal atoms in neighbouring slabs has a substantial effect on 2-layer slabs of larger surface area, such as the ones used here.

Another single adsorption energy calculation for propane was performed on a 2-layer Ni(100) slab in which the bottom layer was fixed and the top layer was allowed to relax. When compared to the calculation in which the atoms in both layers were allowed to relax, the change in energy was very small (4×10^{-4} eV ~ 0.04 kJ/mol).

The adsorption energies (E_{ads}) of propane on the metal slabs described above were calculated according to the following equation.

$$E_{ads} = E_{prop+slab} - E_{prop} - E_{slab} \quad (4.2)$$

where $E_{prop+slab}$ is the total electronic energy for a propane molecule plus a metal slab when the propane molecule is adsorbed on the metal slab, E_{prop} is the electronic energy of an isolated propane molecule in the gas phase, E_{slab} is the electronic energy for a metal slab, and E_{ads} is the electronic energy for the adsorption of propane on the surface of the

metal slab (or heat of adsorption). Variations in the electrical potential of the slabs were not considered (zero electric field).

4.3 Results and Discussion

The metals investigated in this study have three different crystal structures, body centered cubic (bcc), face centered cubic (fcc), and hexagonal closed packed (hcp). The metal atoms in the surface layer of fcc and bcc structures have 4-fold symmetry with the metal atoms in the layer below. In contrast the metal atoms in the surface layer of the hcp structures have 3-fold symmetry with the metal atoms in the layer below.

The lattice constants (LC) of the metals investigated in this study were used as a control tool to examine the reliability of the calculations. Based on the information in Table 4.1, our DFT calculated LC values (obtained from the geometry of the DFT optimized single unit cell of each metal crystal structure), are in good agreement with both the experimental LC values [33] obtained by X-ray diffraction (XRD) and the LC values that we calculated from the literature values for metal bulk densities [33].

After completing the calculations for the slabs alone, calculations were performed for the combinations of a slab plus propane. The coordination of an adsorbed propane molecule on the surface of each of the metal slabs was optimized. Although there were some variations in the final optimized propane geometries, as a function of crystal structure, there were also many similarities.

The fcc Ni(100) structure is shown as an example in Figure 4.1. The Ni atoms in the upper layer are staggered to have 4-fold symmetry with respect to the Ni atoms in the lower layer of the slab. Three (top, front and side) views of the optimized propane-on-nickel structure are shown. The central carbon atom of propane has on-top coordination with the nickel atom directly below it in the surface of the slab. The two end-carbon atoms in propane are symmetrically elevated from the slab surface, compared to the propane central carbon atom. The hydrogen atoms attached to the central propane carbon atom are also coordinated to the same Ni atom below the central carbon atom. The optimized propane-metal structures for 4-fold symmetry metals, the bcc Fe(100) and the fcc Cu(100) surfaces were generally similar to the one for the fcc Ni(100) surface.

Table 4.1: Metal crystal information: a comparison of a) Lattice Constant (LC) values obtained in this study from DFT calculations that optimized a single unit cell of each metal crystal structure with both b) experimental LC values [33] measured by XRD and c) LC values calculated (in this work) for the metals using literature values of the metal bulk densities [33]

Metal	***Bulk Density (g/cm^3)***	***Crystal structure (a, b, c = LCs)***	***No of atoms in 2-layer slabs***	***LC by our DFT (nm)***	***LC from literature (nm)***	***LC by density (nm)***
Fe(100)	*7.87*	*bcc (a=b=c)*	*32*	*0.287*	*0.287*	*0.285*
Co(100)	*8.90*	*hcp (a=b c=1.63a)*	*32*	*0.250*	*0.251*	*0.234*
Ni(100)	*8.91*	*fcc (a=b=c)*	*36*	*0.352*	*0.352*	*0.353*
Cu(100)	*8.92*	*fcc*	*36*	*0.362*	*0.362*	*0.362*
Zn(100)	*7.14*	*hcp (a=b c=1.86a)*	*32*	*0.268*	*0.267*	*0.254*

The optimized propane-on-metal structures having 3-fold symmetry, hcp metals, were slightly different than the structures for metals having 4-fold symmetry. The cobalt hcp structure is shown in Figure 4.2 as an example. Like propane on Ni(100) (fcc) in Figure

4.1, the carbon-hydrogen bonds of the central propane carbon atom straddled the cobalt atom that was directly below it in the slab. Unlike propane on Ni(100) (fcc), on cobalt the carbon-carbon bond between the propane central carbon atom and one of its end-carbon atoms, was almost parallel to the surface of the slab. As a result, for Co(100) there were two carbon-hydrogen bonds and one carbon-carbon bond in close proximity to the cobalt atom that was below the propane central carbon atom. In contrast Figure 4.1 shows that for Ni(100) the carbon-carbon bonds between the propane central carbon atom and the end carbon atoms are inclined to the surface of the slab.

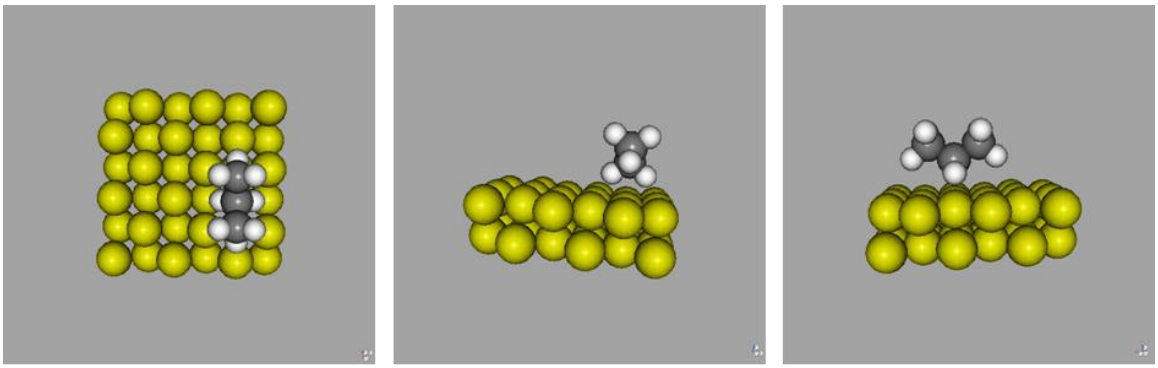

Figure 4.1: *(a)* Top view, *(b)* front view and *(c)* side view of the DFT optimized structure of propane on Ni(100) fcc slab (3×3×1 unit cell system)

Our DFT calculated values for E_{ads}, the electronic adsorption energies (or internal energies of adsorption) of propane on the surfaces of the metal slabs are shown in Table 4.2. These energy values had converged within a tolerance of 10^{-3} eV. The metal slab energies, E_{slab}, correspond to the internal energy of the bulk metal plus a vacuum space above the slab that is equivalent to 9 unit cells in the z direction. In each optimized calculation the positions of all the atoms in the system were relaxed.

The E_{ads} values calculated using DFT in this study can be compared to other values reported in the literature [34-41]. There are a number of experimental and computational

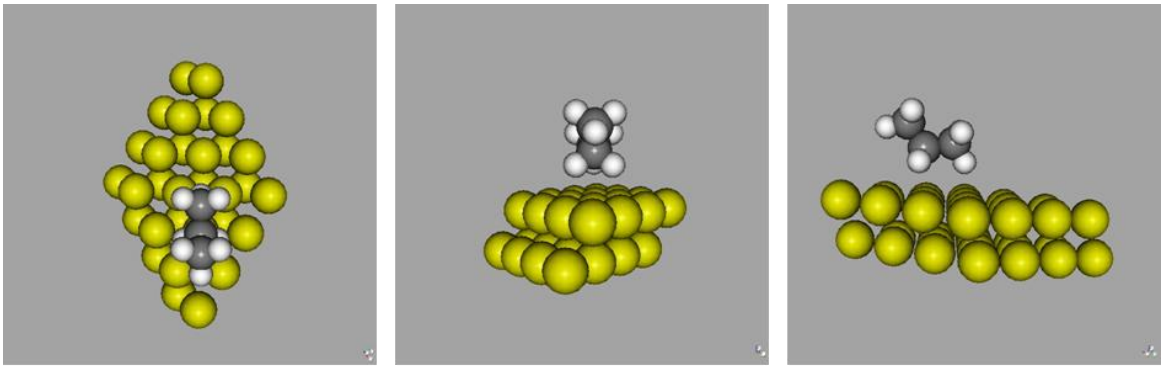

Figure 4.2: *(a)* Top view, *(b)* front view and *(c)* side view of the DFT optimized structure of propane on Co(100) bcc slab (4×4×1 unit cell system)

studies that have been performed on the adsorption of light weight alkanes (eg. methane and ethane [24]), alkenes (eg. ethylene), and alkynes (eg. acetylene) using different metal surfaces. In general the literature E_{ads} values, for the alkynes are greater than those for alkenes and those for alkenes are greater that our results in Table 4.2 for an alkane (propane). This is expected, because the bond strength between a metal atom and a hydrocarbon molecule is expected to increase as the electron density in the carbon-carbon molecular orbitals near the central carbon atom increases: from σ-orbitals (propane), to an additional π-orbital (ethylene) and to two additional π-orbitals (acetylene and propyne). The adsorption energies calculated in this study (Table 4.2) are consistent with such a trend when compared with the E_{ads} values reported for other light weight molecules. For example Medlin and Allendorf [34] reported an E_{ads} of -285.4 kJ/mol for acetylene on a 3-layer Ni(111) slab and Bernardo and Gomes [41] reported an E_{ads} of -170.2 on a 2-layer Ni(100) cluster. These E_{ads} values were also obtained using DFT (slab

or cluster) calculations. Comparing the E_{ads} of propane on a Ni(100) surface in this study, -52.7 kJ/mol (Table 4.2), it is evident that the adsorption energies of these lightweight hydrocarbons on Ni surfaces follow the expected order: E_{ads} (C_3H_8) < E_{ads} (C_2H_4) < E_{ads} (C_2H_2).

Table 4.2: Calculated DFT energies (eV and kJ.mol) for: the metal slabs (E_{slab}), the systems of metal slabs + adsorbed propane ($E_{prop+slab}$), and the adsorption energies (E_{ads}) for propane on the slabs, where $E_{ads} = E_{prop+slab} - E_{slab} - E_{prop}$. The calculated DFT total energy of propane (E_{prop}) in the gas phase is -589.863 eV.

Metal	***E_{slab} (eV)***	***E_{tot} (eV)***	***E_{ads} (eV)***	***E_{ads} (kJ/mol)***
Fe(100)	*-14952.774*	*-15543.145*	*-0.508*	*-49.1*
Co(100)	*-20198.142*	*-20788.548*	*-0.543*	*-52.4*
Ni(100)	*-29451.891*	*-30042.299*	*-0.545*	*-52.7*
Cu(100)	*-37763.985*	*-38354.281*	*-0.434*	*-41.9*
Zn(100)	*-41492.931*	*-42083.173*	*-0.380*	*-36.7*

The following three adsorption energies, E_{ads}, of propane, were compared in Figure 4.3: E_{ads} on a fully relaxed 2-layer Ni(100) slab; E_{ads} on a 2-layer Ni(100) slab with a relaxed top layer and a bottom layer with atoms fixed at the positions of bulk nickel; and a fully relaxed 4-layer Ni(100) slab. The difference between the 2-layer slab that is fully relaxed and the one with the atoms in the bottom layer having fixed positions (0.0004 eV) was not distinguishable on the energy scale used in Figure 4.3. Although the difference between E_{ads} of propane on a 4-layer and 2-layer Ni(100) slabs, ~0.04 kJ/mol, is appreciable, it is within the target accuracy for functionals [32]. That 0.04 kJ/mol difference is small enough to conclude that the trend obtained from 2-layer calculations in Figure 4.3 is qualitatively correct.

This work has shown that propane is chemisorbed, not physisorbed on metal surfaces. The heats of propane adsorption on metals in this work varied from 36 to 53 kJ/mole (0.38 to 0.55 eV/molecule). In contrast heats of physical adsorption are generally comparable to the latent heat of vaporization of the adsorbed molecule. For propane the latent heat of vaporization at 25°C is 15 kJ/mole (0.16 eV/molecule). Therefore our chemisorption energies are 2 to 5 times greater than physical adsorption energies.

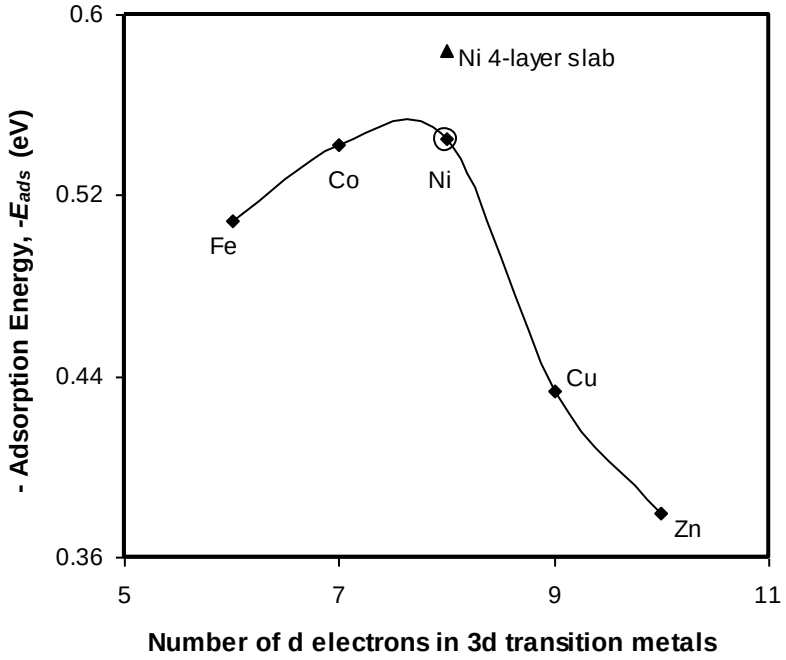

Figure 4.3: Exothermic adsorption energy, -E_{ads}, (eV) calculated using DFT for 3d transition metals versus number of 3d electrons in the metal atom (-♦- all relaxed 2-ayer Ni(100) slab, -○- bottom layer fixed & top layer relaxed 2-layer Ni(100) slab, -▲- all relaxed 4-layer Ni(100) slab)

There are two lines in Figure 4.4 for the carbon-centre to metal-centre distance: the distance from the centre of the central carbon atom in an adsorbed propane species to the centre of the nearest surface metal atom. The 4-fold symmetry metals (fcc, bcc), Fe(100),

Ni(100), and Cu(100) are on one line and have centre to centre distances less than 0.28 nm [Fe (0.271 nm), Ni (0.262 nm), and Cu (0.276 nm)]. The 3-fold symmetry metals (hcp), Co(100) and Zn(100) are on a second line and have centre-to-centre distances greater than 0.3 nm [Co (0.304 nm) and Zn (0.326 nm)].

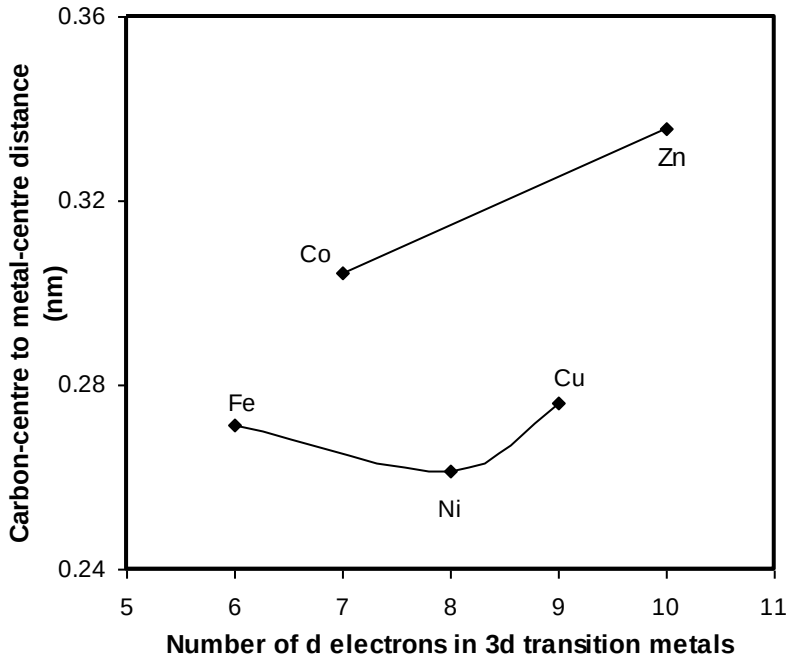

Figure 4.4: Carbon-centre to metal-centre distance (nm) [the distance from the centre of the central-carbon atom in an adsorbed propane species to the centre of the nearest surface metal atom] versus number of d electrons in 3d transition metals

Some older explanations of catalysis and adsorption sometimes included the categories of an electronic factor or a geometric factor [42]. The separation of the 3d metals in Figure 4.4 into two categories based on of the geometry of the metal surfaces is a geometric factor.

Mulliken population analyses were determined for each metal slab on which propane was adsorbed. In every case there was electron population movement from the metal to the adsorbed propane species. In general, there was an increase in the electron population on the carbon atoms of the propane adsorbed on each metal slab, as shown in Figure 4.5, for propane in vacuum and for propane adsorbed on Ni(100). The electron populations on the three propane carbon-hydrogen groups [methyl-methylene-methyl] were [7.024 – 5.951 – 7.024]$_{VAC}$, for propane in vacuum, [7.039 – 6.037 – 7.039]$_{Ni}$, for propane on Ni(100) having 4-fold symmetry, and [7.019 – 5.980 – 7.050]$_{Co}$, for propane on Co(100) having 3-fold symmetry, respectively. For the metals with 4-fold symmetry, the majority of the electron population transferred from the slab was transferred from the metal atom adjacent to the central-carbon of propane. The equality of the electron population [7.039] on the two methyl groups on Ni(100) is consistent with the symmetrical propane structure in Figure 4.1 where the two end carbon atoms are equally elevated from the surface. That was not the case for metals having 3- fold symmetry. For the metals with 3-fold symmetry the majority of the electron population was transferred from two different metal atoms. As mentioned previously, metals with 3-fold symmetry had two carbon atoms parallel to the metal surfaces. For Co(100) the electron population on the methyl group nearest the surface [7.050] was much greater than the one that was elevated from the surface [7.019]. The positions of both those methyl groups are shown in Figure 4.2.

The carbon-centre to metal-edge distance, the distance from the centre of the central carbon atom in an adsorbed propane species to the nominal edge of the nearest metal surface atom, is an alternative parameter. It was computed by subtracting the metal radius

(determined from the metal bulk density) from the carbon-centre to metal-centre distance, shown in Figures 4.4. The advantage of the carbon-centre to metal-edge distance is that it does not include the metal radius, which varies from metal to metal, and is only dependant on the propane species.

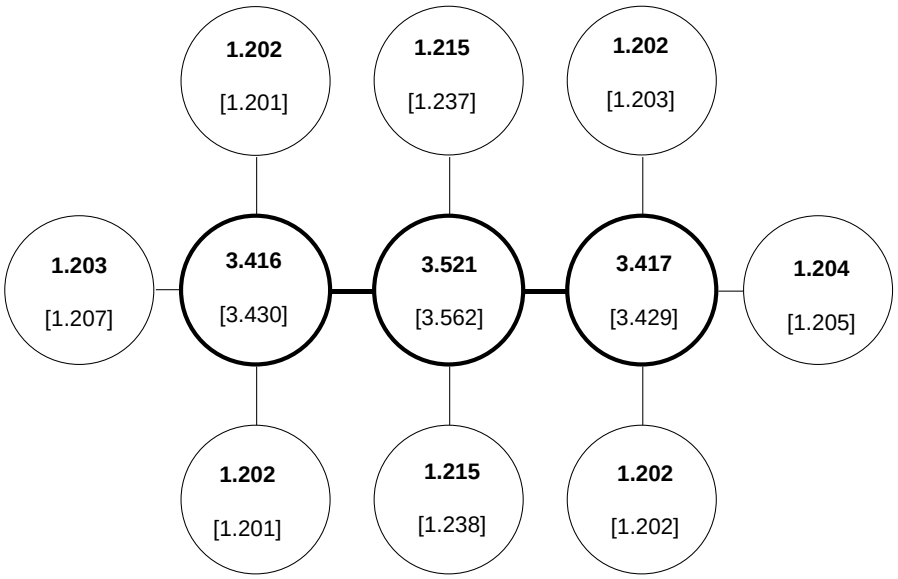

Figure 4.5: Schematic diagram showing the electron populations from Mulliken population analyses on the atoms in (a) a propane molecule in vacuum (numbers without brackets), and (b) a propane molecule adsorbed on the Ni(100) surface of a slab [numbers in square brackets]. The circles with the thickest lines represent carbon atoms. The thinner lined circles represent hydrogen atoms

The propane adsorption energies on 3d metals are shown in Figure 4.6 as a function of the carbon-centre to metal-edge distance. It is much different than the volcano plot in Figure 4.3. In Figure 4.6, the geometric factor attributed to the difference between 3-fold and 4-fold symmetry surfaces is displayed as two separate correlation lines. In addition a

second geometric factor is apparent. For metals having the same surface symmetry, there is an inverse relationship between the propane adsorption energy and the carbon-centre to metal-edge distance. The closer the adsorbed propane is to the edge of the metal, the larger the adsorption energy. Although the slopes of the two correlation lines shown in Figure 4.6 are the same, the intercept for 3-fold symmetry surfaces is distinctly different from that for 4-fold symmetry surfaces.

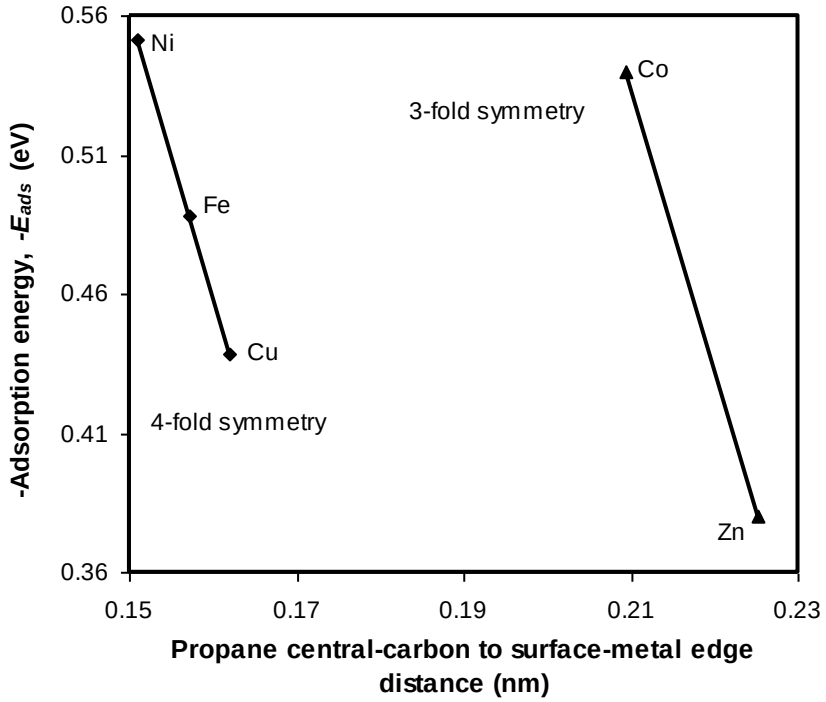

Figure 4.6: DFT calculated exothermic adsorption energy, $-E_{ads}$ (eV), versus carbon-centre to metal-edge distance [the distance from the centre of the central carbon atom in an adsorbed propane species to the nominal edge of the nearest metal surface atom] (nm)

The two geometric factors evident in Figure 4.6 provide a partial explanation for the volcano plot in Figure 4.3. Different symmetries of the metal surface atoms contribute to

the shape of the volcano plot. In addition for metal surfaces having the same symmetry, the carbon-centre to metal-edge distance also contributes to the shape of the volcano plot.

Figure 4.7 shows that there is a correlation between the C-H bond length for the central carbon atom in adsorbed propane and the carbon-centre to metal-edge distance. All the 3d metals, regardless of the symmetry of their surface atoms, follow the same trend. The C-H distance (1.12 nm) on the Zn(100) surface is essentially the same as the C-H distance in gaseous propane. At the other extreme, the adsorbed species on the Ni(100) surface has the longest C-H bond length.

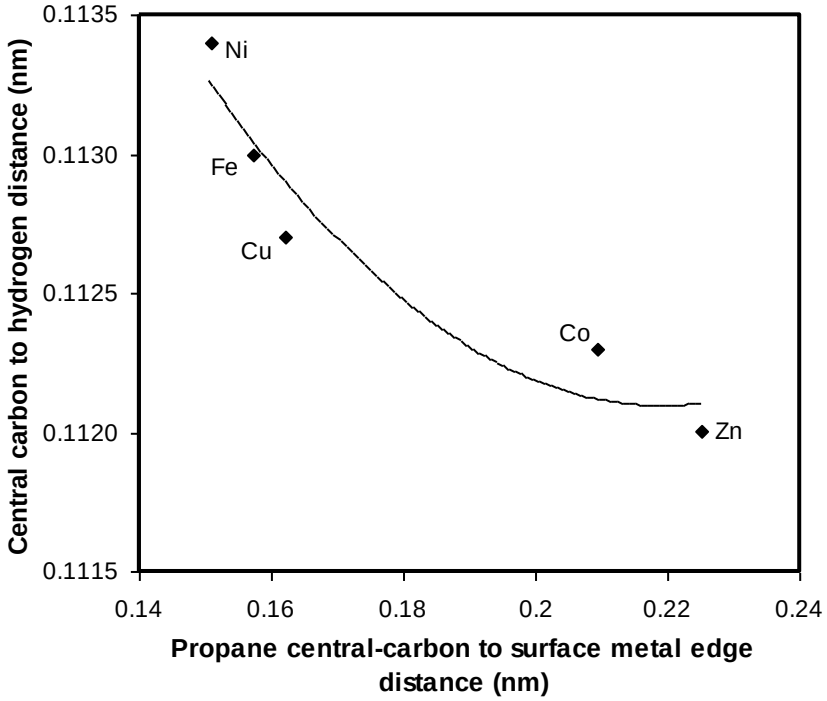

Figure 4.7: C-H bond length for the central carbon atom (nm) in adsorbed propane species versus carbon-centre to metal-edge distance [the distance from the centre of the central carbon atom in an adsorbed propane species to the nominal edge of the nearest metal surface atom] (nm)

The C-H bond length of the central carbon atom in propane, in Figure 4.7, is of interest for two reasons. The larger the C-H values the more closely the adsorbed propane species approach the next step in the reaction network, dehydrogenation. The smaller the C-H values the more closely the adsorbed propane species approach the reverse step, desorption to gas phase propane.

Because the adsorbed propane species on the Ni slab has the largest C-H bond length it is closest to dehydrogenation and furthest from desorption, and on that basis it may be a good candidate to replace Pt as the anode electrode material in fuel cells that operate at a temperature where liquid water is not present and where corrosion resistance is not a prime concern.

4.4 Conclusion

The DFT calculated energies for propane adsorption on transition metal (100) surfaces (Fe, Co, Ni, Cu, and Zn) were found to be in the range from -36 to -53 kJ/mol. These values are consistent with the order alkanes < alkenes < alkynes. This work has shown that propane is chemisorbed, rather than physisorbed on metal surfaces.

When the adsorption energies for 3d metals were plotted as a function of the number of 3d electrons in the metal, a volcano plot was obtained. Two geometric factors were identified. The geometry of propane adsorbed on metals whose surface atoms had 4-fold symmetry was different than that on metals having 3-fold symmetry. The carbon-centre to metal-edge distance of the adsorbed propane species was much shorter for 4-fold

symmetry than for 3-fold symmetry metals. On 4-fold symmetry surfaces the propane central carbon atom was adsorbed on-top of a metal atom with the two end carbon atoms further from the surface forming a symmetrical configuration. In contrast, on 3-fold surfaces the central carbon atom and one of the end carbon atoms were almost parallel to the surface with the second end carbon atom much further from the surface.

When the adsorption energies on 3d metals were plotted as a function of the central-carbon to metal-edge distance, a second geometric effect was identified. Both 4-fold symmetry metals and 3-fold symmetry metals had correlation lines with the same slope. For metals of the same symmetry there is an inverse relationship between the propane adsorption energy and the carbon-centre to metal-edge distance. A small change in distance had a large impact on the adsorption energy.

For all of the 3d metals investigated the C-H bond length for the central carbon atom in the adsorbed propane species was found to vary with the central-carbon to metal-edge distance. The adsorbed propane species on the Ni(100) surface had the longest C-H bond length. Therefore it was closer to dehydrogenation and further from desorption than any of the adsorbed propane species on other metal surfaces. As a result Ni was identified as a possible replacement for Pt anodes in fuel cells where there is no water in the liquid phase and corrosion is not expected to be an issue.

5.5 References

[1] Liebhafsky, H. A.; Cairns, E. J. *Fuel Cells and Fuel Batteries: a Guide to Their*

Research and Development; Wiley: New York, **1968**

[2] Bockris, J. O.; Srinivasan, S. *Fuel Cells: Their Electrochemistry,* McGraw-Hill: New York, **1969**

[3] Cairns, E. J.: *Adv. Electrochem. Electrochem. Eng.* **1971**, *8*, 337-392

[4] Gross, M.D.; Vohs, J.M.; Gorte, R.J. *J. Mater. Chem.* **2007**, *17*, 3071-3077

[5] Heo, P.; Ito, K.; Tomita, A.; Hibino, T. *Angew.Chem. Int. Ed.* **2008**, *47*, 7841-7844

[6] Bagotsky, V.S.; Vassiliev, Y.B.; Khazova, O.A. *J. Electroanal. Chem.* **1977**, *81*, 229-238

[7] Hsieh, S.Y.; Chen, K.M. *Electrochem. Sci. Technol.* **1977**, *124*, 1171-1174

[8] Sustersic, M.G.; Cordova, R.; Triaca, W.E.; Arvia, A.J. *Electrochem. Sci. Technol.* **1980,** *127*, 1242-1248

[9] Hahn, F.; Melendres, C.A. *Electrochim. Acta*, **2001**, *46*, 3525-3534

[10] Savadogo, O.; Rodriguez-Varela, F.J. *J. New Mater. Electrochem. Sys.* **2001,** *4*, 93-97

[11] Cheng, C.K.; Luo, J.L.; Chuang, K.T.; Sanger, A.R. *J. Phys. Chem. B*, **2005**, *109*, 13036-13042

[12] Rodriguez-Varela, F.J.; Savadogo, O. *J. New Mater. Electrochem. Sys.* **2006,** *9*, 127-137

[13] G. Psofogiannakis, Y. Bourgault, B.E. Conway, and M. Ternan, J. Appl. Electrochem. **2006**, *36*, 115-130

[14] Khakdaman, H.; Bourgault, Y.; Ternan, *Ind. Eng. Chem. Res.* **2010**, *49*, 1079-1085

[15] Khakdaman, H.; Bourgault, Y.; Ternan, M. *J. Power Sources,* **2011**, *196*, 3186-3194

[16] Psofogiannakis, G.; St-Amant, A.; Ternan, M. *J. Phys. Chem. B* **2006**, *110*, 24593-24605

[17] Al-Othman, A.; Tremblay, A. Y.; Pell, W.; Liu, Y.; Peppley, B. A.; Ternan, M. *J. Power Sources,* **2012**, *199*, 14-21

[18] Tian, F.; Anderson, A.B. *J. Chem. Phys*. C, **2011**, *115*, 4076-4088

[19] Skulason, E.; Tripkovic, V.; Bjorketun, M.E.; Gudmundsduttir, S.; Karlberg, G.; Rosseisl, J.; Bligaard, T.; Junsson, H.; Norskov, J.K. *J. Phys. Chem. C*. **2010**, *114*, 18182-18197

[20] Sha, Y.; Yu, T.H.; Merinov, B.V.; Shirvanian, P.; Goddard, W.A. *J. Phys. Chem. Lett*. **2011**, *2*, 572-576

[21] Ferrin, P.; Mavrikakis, M. *J. Am. Chem. Soc*. **2009**, *131*, 14381-14389

[22] Zawodzinski, T.; Wieckowski, A.; Mukerjee, S.; Neurock, M. *Electrochem. Soc. Interface*, **2007**, *16[2]*, 37-41

[23] Cortright, R. D.; Watwe, R. M.; Spiewak, B. E.; Dumesic, J. A. *Catalysis Today*, **1999**, *53*, 395-406

[24] Lin, Y. Z.; Sun, J.; Yi, J.; Lin, J. D.; Chen, H. B.; Liao, D. W. *Theo Chem*, **2002**, *587*, 63-71

[25] Soler, J.M.; Artacho, E.; Gale, J.D.; Garcia, A.; Junquera, J.; Ordejon, P.; Sanchez-Portal, D. *J. Phys.: Condens. Matter*. **2002**, *14*, 2745-2779

[26] Perdew, J. M.; Burke, K. Ernzerhof, M. *Phys. Rev. Lett*. **1996**, *77*, 3865-3868

[27] Ford, C.; Nilekar, A.U.; Xu, Y.; Mavrikakis, M. Surf. Sci. **2010**, *604*, 1565-1575

[28] Jiang, T.; Mowbray, D.J.; Dobrin, S.; Falsig, H.; Hvolbaek, B.; Bligaard, T.; Norskov, J.K. *J. Phys. Chem. C* **2009**, *113*,10548-10553

[29] Hummelshoj, J.S.; Blomqvist, J.; Datta, S.; Vegge, T.; Rossmeisl, J.; Thygesen, K.S.; Luntz, A.C.; Jacobsen, K.W.; Norskov, J.K. *J. Chem. Phys.* **2010**, *132*, 071101

[30] Taylor, C.D.; Neurock, M.; Scully, J.R. *J. Electrochem. Soc.* **2011**, *158*, F36-F44.

[31] Grabow, L.C.; Hvolbaek, B.; Noskov, J.K. *Top. Catal.* **2010**, *53*, 298-310.

[32] Koch, W.; Holthausen, M.C. *A Chemist's Guide to Density Functional Theory, 2nd ed.*, Wiley-VCH: Weinham, **2001**

[33] Haynes, W. M. *CRC Handbook of Chemistry and Physics*, 91st ed.: CRC Press: **2010**

[34] Medlin, J. W.; Allendorf, M. D. *J. Phys. Chem. B*, **2003**, *107*, 217-223

[35] Gross, H.; Campbell, C. T.; King, D. A. *Surf. Sci.* **2004**, *572*, 179-190

[36] Peck, J. W.; Mahon, D. I.; Koel, B. E. *Surf. Sci.* **1998**, *410*, 200-213

[37] Mittendorfer, F.; Thomazeau, C.; Raybaud, P.; Thoulhoat, H. *J. Phys. Chem. B* **2003**, *107*, 12287

[38] Hofmann, S.; Csanyi, G.; Ferrari, A. C.; Payne, M. C.; Robertson, *J. Phys. Rev. Lett.* **2005**, *95*, 036101

[39] Valcarcel, A.; Ricart, J. M.; Clotet, A.; Markovits, A.; Minot, C.; Illas, F. *Surf. Sci.* **2002**, *519*, 250

[40] Valcarcel, A.; Clotet, A.; Ricart, J. M.; Illas, F. *Chem. Phys*. **2005**, *309*, 33-39

[41] Bernardo, C. G. P. M.; Gomes, J. A. N. F.; *J. Molec. Strruc*. **2001**, *542*, 263-271

[42] Thomas, J. M.; Thomas, W.J., *Introduction to the Principles of Heterogeneous Catalysis*, Academic Press, London, **1967**

CHAPTER 5

Selectivity in the Reaction of an Adsorbed Intermediate Species on the Anode of a Direct Propane Fuel Cell

Shadi Vafaeyan, Alain St-Amant, Marten Ternan

Abstract

Propane oxidation at the anode of a direct propane fuel cell (DPFC) via a partial Bagotsky-like reaction mechanism was investigated by performing density functional theory (DFT) calculations. There are several reports indicating that at some conditions CO_2 is the predominant product, and that partially oxidized products such as alcohols, aldehydes, carboxylic acids, and carbon monoxide are not formed, if platinum is the anode metal. Alternative electrolytes that operate above the boiling point of water may allow less expensive metals such as nickel (Ni) to be anode materials. The purpose of this work was to investigate the possibility that CO_2 might also be the predominant product if a nickel anode was used. The adsorption energies of H_2O and C_3H_8 , and the transition state energies of the reactants in four reactions (H_2O dissociation, C_3H_8 dehydrogenation to form a propyl radical, propyl dehydrogenation to form an allyl radical, and hydroxylation of a propyl radical to produce propanol) on the surface of a Ni(100) slab were calculated. The results indicate that the propyl radicals adsorbed on a Ni(100)

surface are much more likely to form allyl radicals that remain on the Ni(100) surface than to react with surface hydroxyl radicals to form gas phase propanol.

5.1 Introduction

Fuel cells convert the chemical energy of a fuel into electrical energy. Theoretically they can be more efficient than batteries or combustion processes. Polymer electrolyte membrane fuel cells, PEMFCs, operating near 80°C with precious metal catalysts are one of the more common types. They have several desirable features; low operating temperatures (80°C), large power densities, and small emissions. Currently they are having some success in competing against batteries in at least two niche markets; materials handling (eg. for forklifts) and back-up power (e.g. for telecommunications).

The most commonly used fuels are hydrogen and methanol. Unfortunately no infrastructure exists for their distribution and storage. Furthermore they are both manufactured from natural gas (a hydrocarbon mixture that is primarily methane) using complex reactor systems that have a large capital cost. They also have a large operating cost because 25 % of the natural gas is consumed to provide the endothermic heat for the steam reforming reaction.

Most of the above disadvantages can be avoided by using hydrocarbon fuels directly at the anode of the fuel cell, in a direct hydrocarbon fuel cell, DHFC. Natural gas is generally available in urban areas. Liquefied petroleum gas LPG, (mostly propane) can be delivered by trucks, in rural areas where roads exist. The cost of delivering

conventional electrical power in rural areas is about an order of magnitude greater than in urban areas, even though the price charged for electrical power is similar. Therefore in real terms, a greater capital cost for fuel cells can be justified for rural areas than for urban areas. Despite their many advantages, DHFCs have one substantial drawback. They have much smaller current densities (reaction rates) than fuel cells using hydrogen or methanol.

During the 1960's an extensive amount of research on DHFCs was performed [1-3]. Since that time there have been relatively few investigations. They include hydrocarbons being fed to the anode of solid oxide fuel cells [4], operations at 300°C using 1 mm thick $Sn_{0.9}In_{0.1}P_2O_7$ [5], kinetics and mechanisms [6-9], and the use of polymer electrolytes [10-12].

Work in our laboratory has been directed toward the improvement of current densities in direct propane fuel cells, DPFCs. One aspect of our work has been to develop a zirconium phosphate-glycerol electrolyte [13] that can operate at temperatures above the boiling point of water (120 - 200°C). In the absence of liquid phase water corrosion should be less severe, and electro-catalysts other than precious metals may be suitable, thereby decreasing capital costs. Another aspect of our work has been to investigate nickel metal as an anode catalyst. Nickel has been used successfully in alkaline fuel cell anodes. Compared to precious metals it is inexpensive. Non-fuel cell applications are known to use catalysts having large nickel contents (well in excessive of one mono-layer) that do not require careful dispersion of small metal particles [14].

In this work some of the steps in the propane electro-oxidation network on a Ni (100) surface of a thin film were investigated using density functional theory, DFT. The overall reaction between propane and water at the anode is shown in the reaction below (Equation 5.1).

$$C_3H_8 + 6H_2O(g) \longrightarrow 3CO_2(g) + 20H^+(ZrP) + 20e^{-1}(Ni) \quad (5.1)$$

where (g) stands for gas phase, (ZrP), for $Zr(HPO_4)_2 \bullet H_2O$-Glycerol electrolyte, and (Ni) for nickel metal anode catalyst.

A variety of DFT studies on various fuel cell reactions have been reported. They include: oxygen electro-reduction [15], hydrogen electro-oxidation [16], electro-reduction in the presence of water [17], and methanol electro-oxidation [18]. Although we searched extensively, we were unable to find any experimental or computational studies of propane reactions on metal surfaces, prior to this study. In contrast numerous studies on water, both adsorption [19-21] and dissociation [22-24], have been reported on metal surfaces.

Bagotsky et al. described a reaction network for methane and its derivatives in fuel cells [6]. The reactions shown in Figure 5.1 are a part of an analogous Bagotsky-like electro-chemical reaction network for propane. Both dehydrogenation reactions and hydroxylation reactions using OH groups obtained from the dissociation of water are shown.

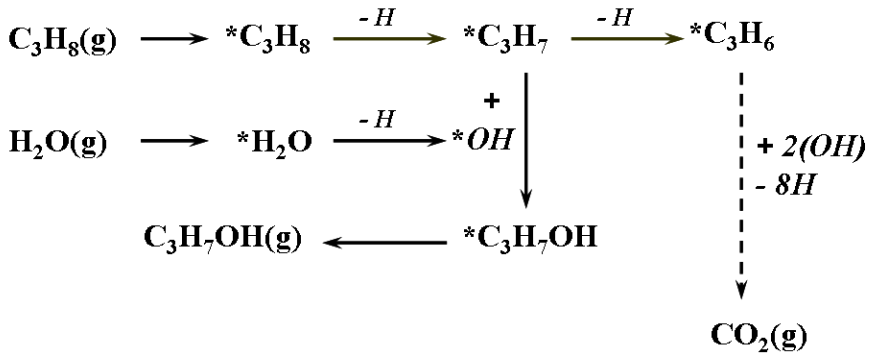

Figure 5.1: A partial Bagotsky-like electro-chemical reaction network for propane

The reactions in Figure 5.1 are chemical reactions. The dehydrogenation reactions in Figure 5.1 produce hydrogen radicals. They can react in a subsequent electrochemical reaction (Equation 5.2) to produce protons and electrons.

$$H \longrightarrow H^{+} + e^{-1} \qquad (5.2)$$

Complete conversion of a hydrocarbon fuel to CO_2, the total oxidized product, is far more desirable than the formation of partially oxidized products such as alcohols, aldehydes, carboxylic acids, and CO. Several experiments with a platinum anode have shown that CO_2 was the predominant product formed at specific operating conditions. The only product reported was CO_2 when the hydrocarbon fuel was (a) ethylene being fed to a sulphuric acid fuel cell [25], (b) propane being fed to a phosphoric acid fuel cell [26], and (c) methane being fed to a PEMFC [27]. CO_2 was the predominant product when propane was fed to a PEMFC [28]. In contrast when a PEMFC, with a platinum-ruthenium (Pt-Ru) anode, was being fed methane, all of the possible partial oxidation products, CH_3OH, CH_2O, COOH, CO, and CO_2 were formed [11]. Furthermore when a

PEMFC with a platinum anode was being fed propane, the major product was CO_2 at cell potentials less than 0.1 V, and CO when the cell potential was greater than 0.4 V.

The purpose of this investigation was to determine whether or not CO_2 is the dominant product formed on a nickel anode. Four of the reactions in Figure 5.1 were investigated using DFT. The first two steps were, the adsorption of C_3H_8 and its dehydrogenation to form an adsorbed propyl radical ($*C_3H_7$). Followed by water dissociation to form hydrogen (*H) and hydroxyl radicals (*OH). The propyl radical could then be converted by either of two competing reactions: further dehydrogenation to form an allyl radical ($*C_3H_6$) that has two bonds to the surface, which would be more likely to remain attached to the surface than a propyl radical that only has one bond to the surface; or hydroxylation of the propyl radical to produce propanol, a partially oxidized species that may leave the surface to enter the gas phase.

Fuel cell reaction rates are usually expressed as current densities, *j*, that can be described by the Butler-Volmer equation (Equation 5.3).

$$j = j_0 \left\{ exp\left[\frac{-\alpha n_C F \eta}{RT} \right] - exp\left[\frac{\alpha n_C F \eta}{RT} \right] \right\} \qquad (5.3)$$

Where j_0 is exchange current density [mA/cm^2], n_C is moles of charged species per mole of molecular species, F is the Faraday constant (96485 C/mole of charged species), η is overpotential in V, R is gas constant in J/ (mole K), T is Temperature in K, and α is the

transfer coefficient. In turn the exchange current density is given by Equation 5.4.

$$j_0 = n_C F k_{F(C_3H_8)} \left\{ exp\left[\frac{- \alpha n_C F \Delta\phi_{EQ}}{RT} \right] \right\} \quad (5.4)$$

where k_F is the overall rate constant for a first order chemical reaction (e.g. Eq. 5.1) in the forward direction, $\Delta\phi_{EQ}$ is anode half cell potential at equilibrium and where the Arrhenius equation, $k_F = exp[-E_{act}/(RT)]$, can be used to represent rate constants in which E_{act} is the activation energy, the parameter that is the key to the findings in this study.

In this work, density functional theory was used to investigate the four reactions in Figure 5.1 on the (100) surface of a two-layer slab that represents a thin nickel film on an inert catalyst support. The rate constants for each of those reactions will contribute to the overall rate constant, k_F, in Eq. 5.4. The energy barrier for the reactions, calculated according to Eq. 5.6, was to be used for the activation energy, E_{act}, in the Arrhenius equation. The magnitudes of E_{act}, for each of the reactions in Figure 5.1, were to be used to compare their relative rates.

5.2 Methodology and Computational Details

Quantum chemical computations were performed by using SIESTA software [29] that is based on Kohn-Sham density functional theory (DFT). The generalized gradient approximation method (GGA) was used as the exchange correlation functional type, with Becke, Lee, Yang, Parr (BLYP) parameterization. The default basis set was a double-ζ

polarization set composed of a compact and a diffused orbital basis. The default value of 100 Rydberg (1300 eV) was used for the mesh cutoff energy. A 4×4×4 (4*4*4/2=32 k-points) Monkhorost-Pack 32 *k*-point mesh was used. The convergence as a function of the number of *k*-points was examined carefully. Increasing the k-point mesh from 32 k-points to 48 k-points changed the adsorption energies by an insignificant amount (~4×10^{-5} eV or ~8×10^{-3} kJ/mol). The atomic coordinates of the adsorbed species were allowed to relax to determine the geometry having the minimum energy. If the change in energy was less than 10^{-3} eV and if the change in the maximum atomic force was less than 0.01 eV/Å, between successive calculations, then the convergence criteria were attained and the atomic geometry optimized.

The pseudopotential for nickel was generated using the ATOM program of SIESTA. The Perdew Burke Ernzerhof (PBE) [30] exchange correlation was used for the generation of the electronic configuration. The Improved Troullier-Martins (tm2) method was used to generate the pseudopotential file for nickel in its non-polarized ground state electron configuration. The pseudopotential input file for a metal required that a particular core radius, r_c, be specified. It was obtained by trial and error. If the initial r_c value was too small ($\leq$ 1.5 for metals used in this study), the pseudopotential could not be generated. After a trial value of r_c that was slightly greater than the minimum acceptable value had been obtained, the software would generate an exact value for r_c. That r_c value (3.34 bohr for nickel) was used to generate the pseudopotential. The pseudopotential output file was used for all subsequent computations that included nickel atoms.

DFT calculations were performed on a system of periodically repeated entities, defined in terms of metal unit cells. Each entity consisted of one or two adsorbed species (e.g. OH, C_3H_7) on a slab of nickel atoms. A nickel slab having a (100) surface and two layers was used in all calculations. The fcc nickel slabs were in a 3×3×10 metal unit cell arrangement with 4 atoms per metal unit cell (3*3*4 =36). The 36 metal atoms per slab is typical of the number of metal atoms used in many DFT slab calculations [31-34]. Nine of the 10 metal unit cells in the z-direction were empty and together they constituted the vacuum layer.

The fractional surface coverage of propane was less than 0.2 in these slabs. This comparatively small surface coverage avoided both adsorbate-adsorbate interactions and interactions between the adsorbed propane and metal atoms in neighbouring slabs. Adsorbate-adsorbate interactions can cause large changes in binding energy [35] (as much as 1 eV when the fractional surface coverage increases from 0.2 to 1.

The adsorption energies (E_{ads}) of the adsorbates (initially adsorbed reactants and subsequent adsorbed intermediate species) on the metal slabs were calculated according to Equation 5.5.

$$E_{ads} = (E_{adsorbate+slab})_{MIN} - E_{adsorbate(g)} - E_{slab} \qquad (5.5)$$

where $E_{adsorbate+slab}$ is the total electronic energy for the absorbate plus metal slab and $(E_{adsorbate+slab})_{MIN}$ is the total electronic energy for the configuration of the adsorbate plus

metal slab that has the minimum energy, $E_{adsorbate(g)}$ is the electronic energy of an isolated adsorbate molecule in the gas phase, E_{slab} is the electronic energy for a metal slab, and E_{ads} is the electronic energy for adsorption of the species on the surface of the metal slab (or heat of adsorption).

The activation energy (energy barrier), E_{act} for each reaction was obtained by calculating $E_{adsorbate+slab}$ as a function of the adsorbate-slab bond length. For each $E_{adsorbate+slab}$ calculation for a particular fixed bond length between the adsorbate and the slab, the value of the adsorbate-slab bond length was maintained constant, while all other bond lengths and all bond angles in the adsorbed species were relaxed to obtain the adsorbate configuration having the minimum energy for that particular adsorbate-slab bond length. Subsequently the resulting energies that had been calculated at each adsorbate-slab bond length were compared as a function their bond lengths. The configuration of the adsorbed species having the maximum energy, $(E_{adsorbate+slab})_{MAX}$, was the transition state (TS) and the configuration of the adsorbed species having the minimum energy, $(E_{adsorbate+slab})_{MIN}$, was the initial state of the reaction. The activation energies (energy barriers) were obtained using Equation 5.6.

$$E_{act} = (E_{adsorbate+slab})_{MAX} - (E_{adsorbate+slab})_{MIN} \quad (5.6)$$

Variations in the electrical potential of the slabs were not considered (zero electric field).

5.3 Results and Discussion

A dehydrogenation mechanism for the transformation of propane, in the gas phase, to an adsorbed propyl radical is shown in Figure 5.2. The formula -(Ni – Ni)-$_{slab}$ represents a 36 atom slab of Ni atoms in two layers in which the Ni atoms in each layer have four-fold symmetry. The adsorbed propane, Figure 5.3a, is oriented parallel to the Ni slab surface. That is, a plane drawn though the three carbon atoms in the adsorbed propane, Figure 5.3a, is perpendicular to the surface of the Ni(100) surface. The central carbon atom of the propane has on-top coordination with the nickel atom below it. Relative to the central carbon atom, the two propane end carbon atoms are symmetrically elevated from the slab surface. The hydrogen atoms that are bonded to the propane central carbon atom are also coordinated to the same Ni atom as the propane central carbon atom. The C–H bond distance (in Figure 5.3) between the central carbon atom and its hydrogen atoms is 0.110 nm compared to 0.112 nm when propane is in the gas phase.

The transition state, TS, between an adsorbed propane molecule and an adsorbed propyl radical, is shown in Figure 5.3b. An important feature of the TS is that both the propyl radical and the separated hydrogen atom remain configured to the same Ni atom in the slab (structure A_3 in Figure 5.2). The TS structure is neither symmetrical nor parallel to the Ni slab surface. A plane drawn through the three carbon atoms of the TS structure, Figure 5.3b, intersects the surface of the Ni(100) slab at an angle that is different from 90°. The carbon-hydrogen distance for the hydrogen being removed from the central propane carbon atom is shown at a distance of 0.170 nm in the TS. That is substantially larger than the 0.110 nm C-H distance in the adsorbed propane.

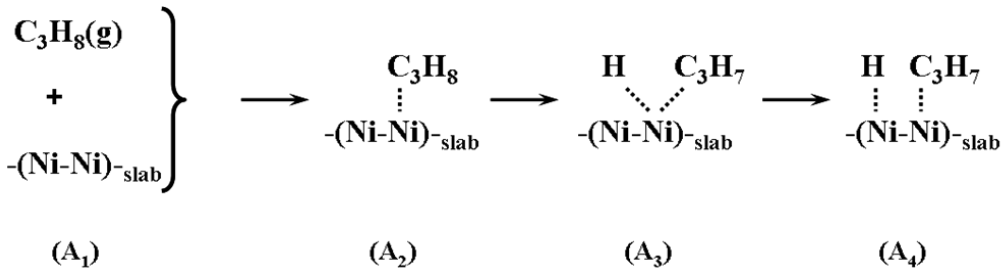

Figure 5.2: Propane adsorption and subsequent dehydrogenation to form a propyl radical on the surface of a Ni(100) slab (A_1, A_2, A_3 and A_4 identify the various entities)

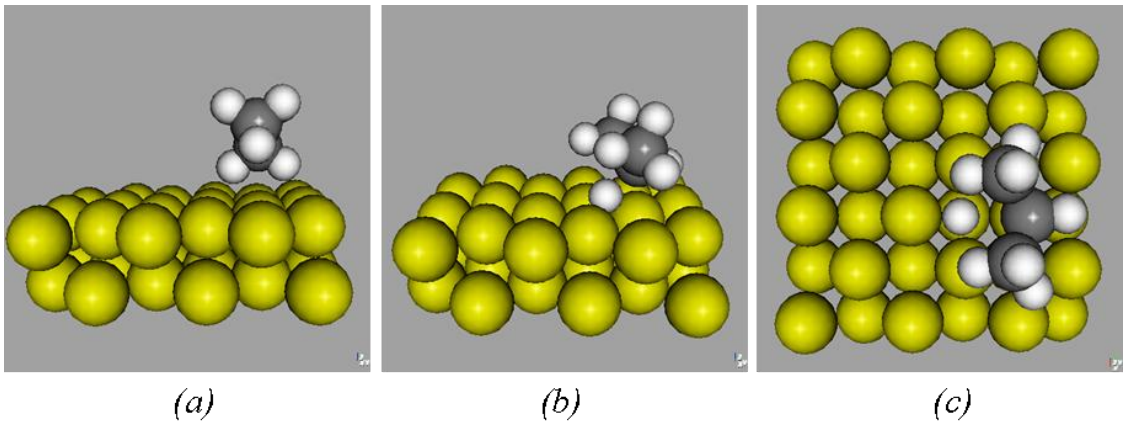

Figure 5.3: DFT optimized structures for (*a*) adsorbed C_3H_8 (front view), (*b*) TS of adsorbed C_3H_8 dehydrogenation to form C_3H_7 radical (front view bent), and (*c*) adsorbed C_3H_7 and H radicals (top view) Ni(100) slab.

Figure 5.4: shows energies for four of the species in Figure 5.2. The extent of the dehydrogenation reaction is indicted by the C–H bond distance between the propane central carbon atom and the hydrogen atom being removed. The energy change upon propane adsorption on the Ni(100) slab is 0.531 ev (51.2 kJ/mole). The barrier height between an adsorbed propane molecule and its TS to an adsorbed propyl radical is 0.734

eV (70.8 kJ/mole). The energy of reaction from an adsorbed propane molecule to an adsorbed propyl radical and adsorbed hydrogen radical is 0.163 eV (15.7 kJ/mole).

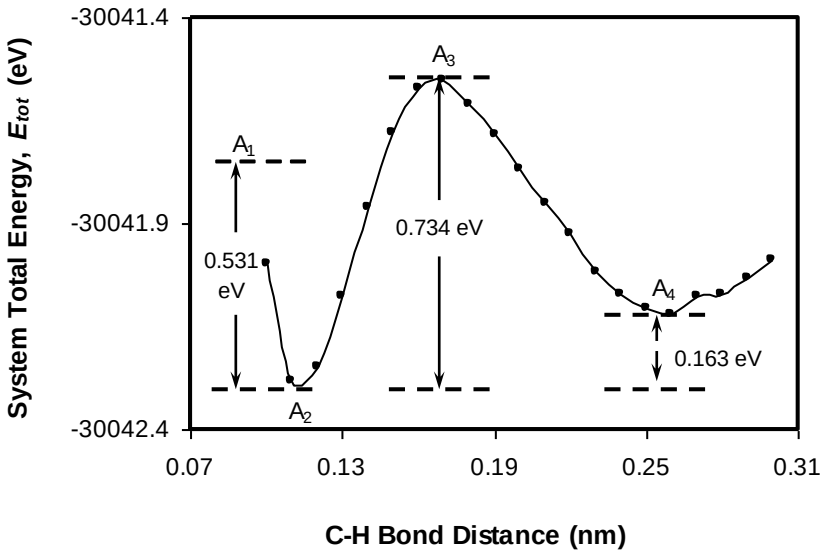

Figure 5.4: Energy plot (obtained using DFT calculated energies) for propane dehydrogenation to form propyl and hydrogen radicals on Ni(100) slab. A_1, A_2, A_3 and A_4 are the entities shown in Figure 5.2

A mechanism for the dissociation of water is shown in Figure 5.5. The structures of the water derived adsorbed species are shown in Figure 5.6. The top view of an adsorbed water molecule suggests that the three-fold nature, of the three atoms in the water molecule (one oxygen atom and two hydrogen atoms), appears to be coordinated on-top of a single Ni atom in the Ni(100) surface. The O–H bond distance in adsorbed water, 0.100 nm, is different than in gas phase water, 0.0945 nm.

The transition state (TS) from adsorbed water to the combination of an adsorbed hydroxyl radical and an hydrogen radical is shown in Figure 5.6b. The O–H bond

distance in the TS has increased to 0.160 nm which is a substantial change when compared to the 0.100 nm O–H bond distance in adsorbed water.

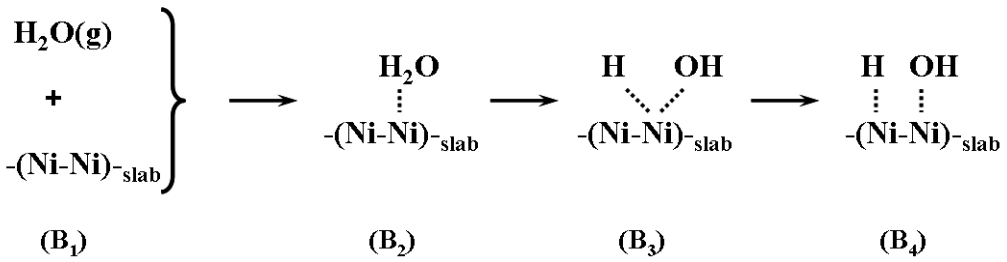

Figure 5.5: Adsorption and dissociation of water on the surface of Ni(100) slab. (B_1, B_2, B_3 and B_4 identify the various entities).

The energies of the four species in Figure 5.5 are shown in Figure 5.7, as a function of the dissociation reaction, as measured by the O–H bond distance. The energy change upon water adsorption on the Ni(100) surface is 0.798 ev (77.0 kJ/mole). The barrier height between an adsorbed water molecule and its TS to an adsorbed hydroxyl radical is 0.655 eV (63.2 kJ/mole). There are numerous reports in the literature on the dissociation of water on metals. For example a DFT study [36] of 6 different metals, Os, Ru, P, Ir, Rh, and Pt reported barrier heights in the range 0.343 to 1.25 eV. Another example is a study by Pozzo et al. [22] comparing the dissociation of water on Rh(111) and Ni(111) surfaces. They reported barrier heights of 0.92 and 0.89 for water to dissociation to OH and H on Rh(111) and Ni(111) respectively. The energy change during reaction of an adsorbed water molecule to form an adsorbed hydroxyl radical and an adsorbed hydrogen radical is 0.386 eV (37.2 kJ/mole). The barrier height for the dissociation of water (0.655 eV) (to form hydroxyl radicals and hydrogen radicals) is approximately 10% less than that for the dissociation of propane (to form of propyl radicals and hydrogen radicals). If

a comparison of these two different single barrier heights was the only consideration it would suggest that it might be easier to form hydroxyl radicals than propyl radicals, and that hydroxyl radicals might be more abundant on the Ni(100) surface than propyl radicals.

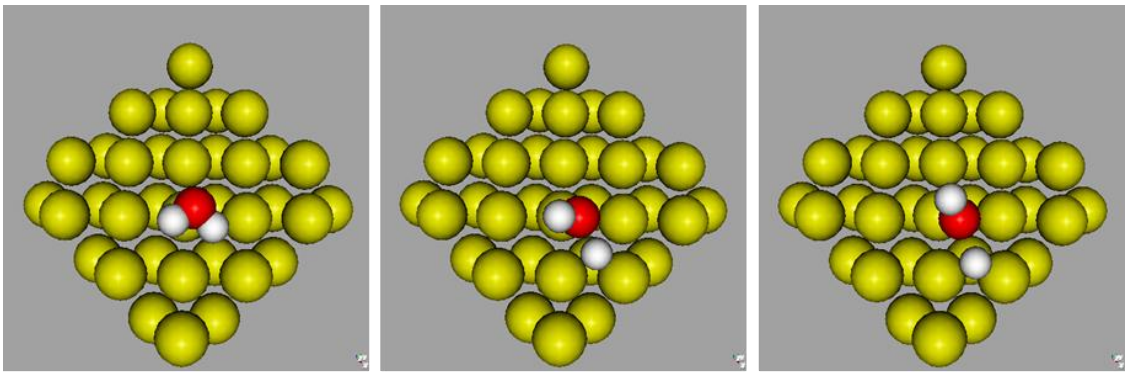

Figure 5.6: Water dissociation: top views of DFT optimized structures for (*a*) adsorbed H_2O (initial state), (*b*) TS: adsorbed OH and H radicals, and (*c*) dissociated OH and H radicals on Ni(100) slab (3×3×1 unit cell system)

A mechanism for the second dehydrogenation reaction, conversion of adsorbed propyl radicals to adsorbed allyl radicals, is shown in Figure 5.8. The structures of the adsorbed propyl radical and the TS from an adsorbed propyl radical to and adsorbed allyl radical are shown in Figure 5.9. The central carbon atom of the adsorbed propyl radical in Figure 5.9a is on-top of one of the Ni atoms in the Ni(100) slab. A plane drawn through the three carbon atoms of the propyl radical intersects the surface of the Ni(100) surface at an angle that is much different than 90°, indicating that the propyl radical is not situated symmetrically on the Ni(100) surface.

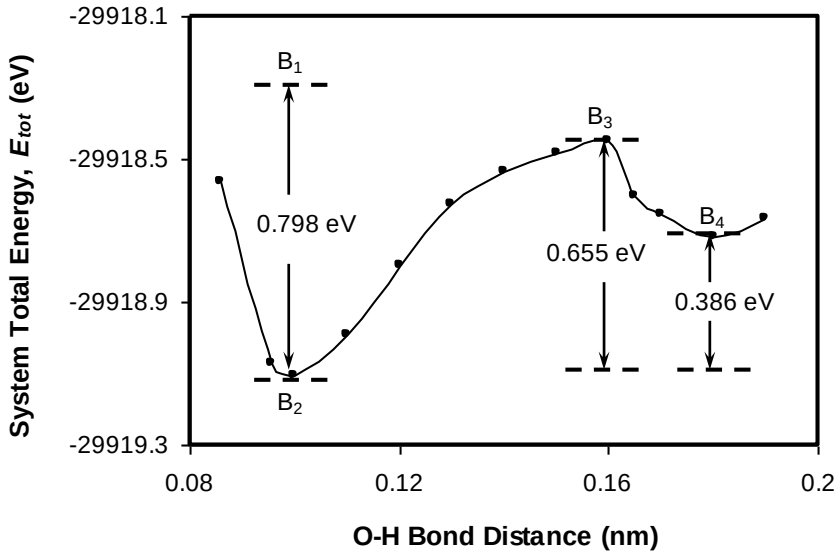

Figure 5.7: Energy plot (obtained using DFT calculated energies) for water dissociation to form hydroxyl and hydrogen radicals on Ni(100) slab. B_1, B_2, B_3 and B_4 are the energy levels for the species in reaction network shown in Fig 5.5.

The transition state (TS) from an adsorbed propyl radical to an adsorbed allyl radical is shown in Figure 5.9b. The central carbon atom of the allyl radical is on-top of a Ni atom in the surface. The hydrogen atom that was removed from the central carbon atom is bridge bonded with two Ni atoms that are adjacent to the Ni atom on which the allyl central carbon atom is on-top. The distance between the allyl radical central carbon atom and the separated hydrogen in the TS has increased to approximately 0.180 nm which is a substantial change compared to the C–H bond distance in an adsorbed propyl radical.

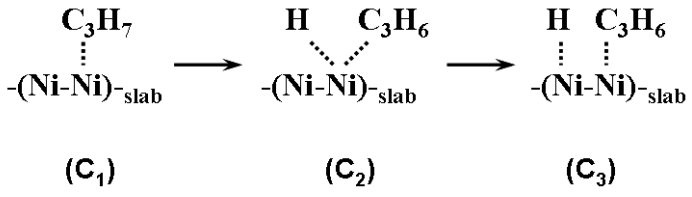

Figure 5.8: Dehydrogenation of propyl (*C3H7) radical to ally (*C3H6) radical on the surface of Ni(100) slab (C_1, C_2 and C_3 identify the various entities)

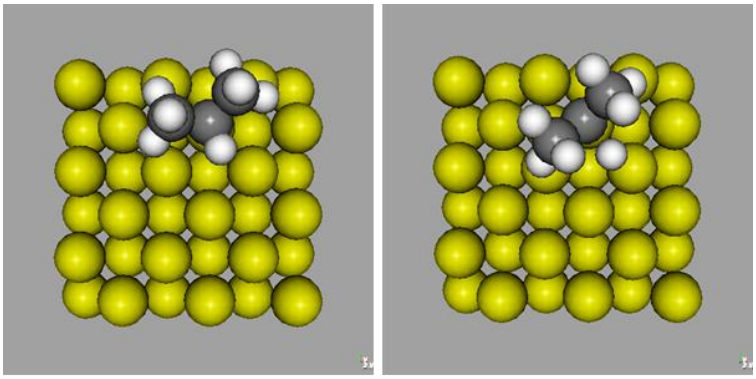

Figure 5.9: Propyl dehydrogenation (allyl radical formation): top views of DFT optimized structures for (*a*) initial state: adsorbed propyl (*C_3H_7), and (*b*) TS: adsorbed allyl (*C_3H_6) and hydrogen (*H) radicals on Ni(100) slab (3×3×1 unit cell system)

The energies of the three species in the transition from propyl to allyl, in Figure 5.8, are shown in Figure 5.10, as a function of the dehydrogenation reaction, as measured by the C–H bond distance. There is a difference in energy of approximately 16 eV between the combination of the propyl radical and slab represented in Figures 5.8 and 5.10 and the combination of propyl radical, hydrogen radical, and slab represented in Figures 5.2 and 5.4. The barrier height between an adsorbed propyl radical and the transition state, TS, to an adsorbed allyl radical and a hydrogen radical, is 1.22 eV (~118 kJ/mole). This barrier height for the formation of allyl radicals is approximately 20 % greater than that for the formation of propyl radicals.

A mechanism for the synthesis reaction, between an adsorbed propyl radical and an adsorbed hydroxyl radical to form propanol, is shown in Figure 5.11. The structures of the adsorbed propyl and hydroxyl species are shown in Figure 5.12a. The central carbon atom of the adsorbed propyl radical in Figure 5.9a is on-top of one of the Ni atoms in the

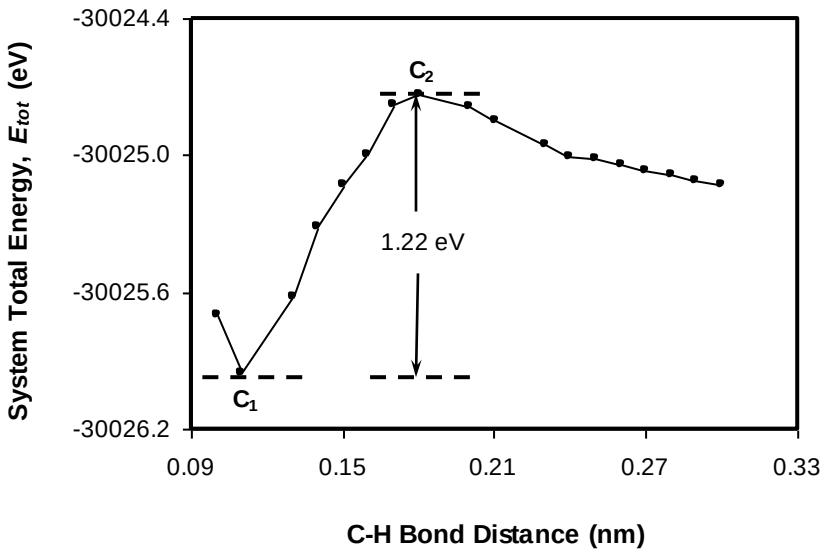

Figure 5.10: Energy plot (obtained using DFT calculated energies) for propyl dehydrogenation to form allyl and hydrogen radicals on Ni(100) slab, C_1 and C_2 are the energy levels for the entities in reaction network shown in Fig 5.8

Ni(100) surface. A plane drawn through the three carbon atoms of the propyl radical intersects the surface of the Ni(100) slab at an angle that is much different than 90°, indicating that the propyl radical is not situated symmetrically on the Ni(100) surface. The C–O bond distance between the central carbon atom in the propyl radical and the oxygen atom in the hydroxyl radical is 0.4 nm.

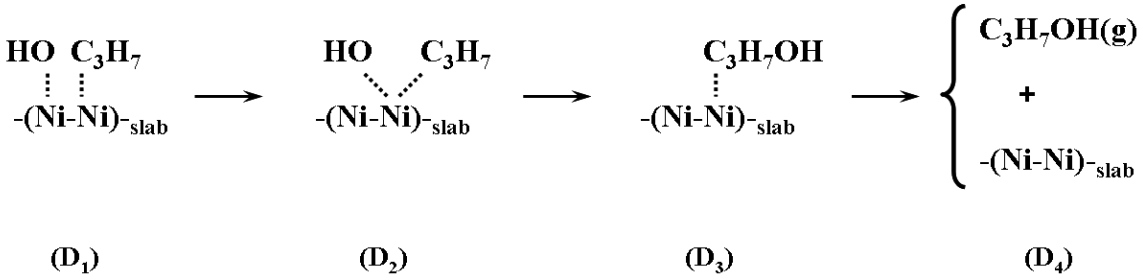

Figure 5.11: Formation of propanol from adsorbed hydroxyl and propyl radicals on the surface of Ni(100) slab. (D_1, D_2, D_3 and D_4 identify the various entities).

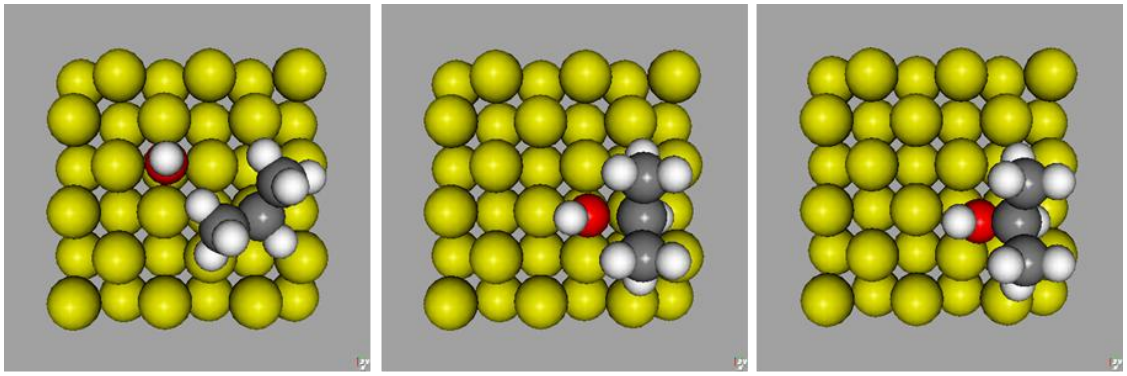

Figure 5.12: Propanol formation: top views of DFT optimized structures for (*a*) initial state: adsorbed propyl and hydroxyl radicals, (*b*) TS: adsorbed propyl and hydroxyl radicals, and (*c*) adsorbed propanol on Ni(100) slab.

The transition state (TS) during the reaction of an adsorbed propyl radical and an adsorbed hydroxyl radical to form an adsorbed propanol molecule is shown in Figure 5.12b. The C–O bond distance in the TS has decreased to 0.215 nm from its 0.4 nm value when the two species were in their most stable states. It should be noted that both the carbon atom in propyl radicals and the oxygen atom in the hydroxyl radicals are coordinated to the same Ni atom in the TS, prior to the synthesis reaction and the formation of a C–O bond. It appears they need to be adsorbed on the same atom in order to be geometrically close enough for the reaction to occur.

The energies of the four species (propyl, hydroxyl, adsorbed propanol, and propanol in the gas phase) are shown in Figure 5.13, as a function of the C–O distance. The energy of reaction between an adsorbed propyl radical and an adsorbed hydroxyl radical to form an adsorbed propanol molecule is 0.507 eV (48.9 kJ/mole). The barrier height is 1.59 eV (~153k J/mole) for the formation of the propanol transition state species (formed from an

adsorbed propyl radical and an adsorbed hydroxyl radical). In contrast the barrier height, is approximately 25% less (1.22 eV) for the formation of the allyl radical transition state species (discussed above) than that for the propanol TS species (1.59 eV). Furthermore, to desorb propanol from the Ni surface into the gas phase, an additional amount of energy, 0.819 eV (~79.0 J/mole), must be provided.

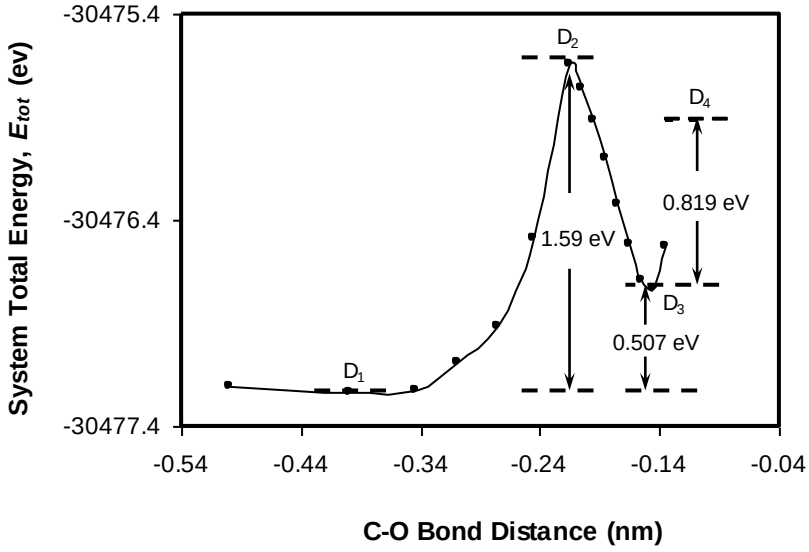

Figure 5.13: Energy plot (obtained using DFT calculated energies) for propanol formation from hydroxyl and propyl radicals on Ni(100) slab. D_1, D_2, D_3 and D_4 are the energy levels for the entities in reaction network shown in Fig 5.11

The Boltzmann factor, $exp(-E_{act}/RT)$, represents the probability that molecules have sufficient energy to attain the transition state, where E_{TS} is the barrier height for the reaction. It can be used to estimate the ratio of two reaction rates. The transformation of a propyl radical to an allyl radical [with barrier height $(E_{act})^{allyl}$] is the desired reaction because the species stays on the surface and therefore retains the possibility of eventually being converted to CO_2, the complete combustion product. The reaction of a propyl

radical with a hydroxyl radical to form propanol in the gas phase [with barrier height $(E_{act})^{propanol}$,] is the undesired reaction, because propanol is a partially combusted product that retains chemical energy that could have been converted to electrical energy by further electrochemical reaction to carbon dioxide.

Values for the barrier heights were obtained in the preceding computations. Allyl radicals were formed from propyl radicals in one reaction with $(E_{act})^{allyl} = 1.22$ eV. In contrast two reaction steps are used to transform propyl radicals to gas phase propanol molecules. First, a propyl radical reacts with a hydroxyl radical to form adsorbed propanol, $(E_{act})^{ads\text{-}C3H7OH} = 1.59$ eV, and then the adsorbed propanol is desorbed to form propanol in the gas phase , $(E_{des})^{gas\text{-}C3H7OH} = 0.82$ eV. Because two steps are required for one transformation and one step for the other, a comparison of two different single barrier heights will not describe the phenomenon. The combination $\exp[-(E_{act})^{propanol}/RT] = exp(-1.59/RT)*exp(-0.82/RT)$, giving $(E_{act})^{propanol} = 2.41$ eV represents the product of two phenomena: the fraction of adsorbed propyl radical vibrations that result in a transformation to adsorbed propanol, and the fraction of adsorbed propanol vibrations that result in the formation of the gas phase propanol. The ratio B of the two reaction rates is shown in Equation 5.7.

$$B = \frac{allyl}{propanol} = \frac{exp[-(E_{act})^{allyl}/RT]}{exp[-(E_{act})^{propanol}/RT]} \qquad (5.7)$$

The ratio, B in Eq 5.7, calculated at 150°C (423K) was 1.4×10^{14}. That result indicates

that propanol is an unlikely product. We are not aware of any experimental fuel cell results on the selectivity for CO_2 on a nickel anode. However, platinum is in the same column of the periodic table as nickel, and platinum is frequently used as a fuel cell electrode. These computed results for an Ni(100) surface are consistent with experimental results on platinum catalysts that found carbon dioxide as the predominant product. This study suggests that carbon dioxide may also be the predominant product on nickel and that the formation of substantial amounts of partially oxygenated products is unlikely.

5.4 Conclusion

The DFT results reported here indicate that propyl species adsorbed on a nickel(100) surface are much more likely to form an allyl species on the nickel(100) surface than to react with a surface hydroxyl species to form gas phase propanol. Forming species that stay on the surface is desirable. Species that stay on the surface can participate in subsequent reaction steps in propane electro-oxidation reaction, and therefore have the possibility of complete electrochemical reaction to CO_2. Forming species that can leave the surface prior to complete electrochemical conversion is undesirable, because some of the chemical energy in the original fuel is not converted to electrical energy.

5.5 References

[1] Liebhafsky, H. A.; Cairns, E. J. *Fuel Cells and Fuel Batteries: a Guide to Their Research and Development*; Wiley: New York, 1968.

[2] Bockris, J. O.; Srinivasan, S. *Fuel Cells: Their Electrochemistry* McGraw-Hill: New York, **1969**

[3] Cairns, E. J.: *Adv. Electrochem. Electrochem. Eng.* **1971**, *8*, 337-392.

[4] Gross, M.D.; Vohs, J.M.; Gorte, R.J. *J. Mater. Chem.* **2007**, *17*, 3071-3077

[5] Heo, P.; Ito, K.; Tomita, A.; Hibino, T. *Angew.Chem. Int. Ed.* **2008**, *47*, 7841-7844

[6] Bagotsky, V.S.; Vassiliev, Y.B.; Khazova, O.A. *J. Electroanal. Chem.* **1977**, *81*, 229-238

[7] Hsieh, S.Y.; Chen, K.M. *Electrochem. Sci. Technol.* **1977**, *124*, 1171-1174

[8] Sustersic, M.G.; Cordova, R.; Triaca, W.E.; Arvia, A.J. *Electrochem. Sci. Technol.* **1980,** *127*, 1242-1248

[9] Hahn, F.; Melendres, C.A. *Electrochim. Acta,* **2001**, *46*, 3525-3534

[10] Savadogo, O.; Rodriguez-Varela, F.J. *J. New Mater. Electrochem. Sys.* **2001,** *4*, 93-97

[11] Cheng, C.K.; Luo, J.L.; Chuang, K.T.; Sanger, A.R. *J. Phys. Chem. B,* **2005**, *109*, 13036-13042

[12] Rodriguez-Varela, F.J.; Savadogo, O. *J. New Mater. Electrochem. Sys.* **2006,** *9*, 127-137

[13] Al-Othman, A.; Tremblay, A.Y.; Pell, W.; Liu, Y.; Peppley, B.A.; Ternan, M. *J. Power Sources*, **2012**, *199*, 14-21.

[14] Wilson, M.F.; Mainwaring, P.R.; Brown, J.R.; Kriz, J.F. *Appl. Catal*. **1988**, *41*, 177 – 198.

[15] Tian, F, Anderson, A.B., *J. Chem. Phys*. C, **2011**, *115*, 4076-4088.

[16] Skulason, E., Tripkovic, V., Bjorketun, M.E., Gudmundsduttir, S., Karlberg, G., Rosseisl, J., Bligaard, T., Junsson, H., Norskov, J.K., *J. Phys. Chem. C*. **2010**, *114*, 18182-18197.

[17] Sha, Y., Yu, T.H., Merinov, B.V., Shirvanian, P., Goddard, W.A., *J. Phys. Chem. Lett*. **2011**, *2*, 572-576.

[18] Ferrin, P., Mavrikakis, M., *J. Am. Chem. Soc*. **2009**, *131*, 14381-14389.

[19] Sebastiani, M.; Site, L. D.; *J. Chem. Therory Comput.* **2005**, *1*, 78-82

[20] Meng, S.; Wang, E. G.; Gao, S. *Phys. Rev. B.* **2004**, *69*, 195404(1-13)

[21] Michaelides, A.; Renea, V. A.; de Andres, P. L.; King, D. A. *Phys. Rev. Lett.* **2003**, *90*, 216102(1-4)

[22] Pozzo, M.; Carlini, G.; Rosei, R.; Alfe, D. *J. Chem. Phys.* **2007**, *126*, 164706-164717

[23] Andersson, K.; Ketteler, G.; Bluhm, H.; Yamamoto, S.; Ogasawara, H.; Pettersson, L. G. M.; Salmeron, M.; Nilsson, A. *J. Am. Chem. Soc.* **2008**, *130*, 2793-2797

[24] Wang, G. C.; Tao, S. X.; Bu, X. H. *Journal of Catalysis* **2006,** *244*, 10-16

[25] Wroblowa, H.; Peirsma, B.J.; Bockris, J.O'M. *J. Electroanal. Chem*. **1963**, 6, 401-416

[26] Grubb, W.T.; Michalske, C.J. *J. Electrochem. Soc.* **1964**, *111*, 1015 – 1019

[27] Bertholet, S.; Gehain, E.; Hahn, F.; Leger, J. M.; Srinivasan, S.; Lamy, C. *Electrooxidation of Methane: PEMFC and in situ Electrochemical Spectroscopic Studies*, Abstracts, *194th Mtg, Electrochem. Soc.* Boston, Nov. **1998**, *98-2*, Abstract No. 1D90

[28] Rodriguez Varela, F.J.; Savadogo, O. *J. Electrochem. Soc.* **2005**, *152*, A1755-A1762

[29] Soler, J.M.; Artacho, E.; Gale, J.D.; Garcia, A.; Junquera, J.; Ordejon, P.; Sanchez-Portal, D. *J. Phys.: Condens. Matter*. **2002**, *14*, 2745-2779

[30] Perdew, J. M.; Burke, K. Ernzerhof, M. *Phys. Rev. Lett*. **1996**, *77*, 3865-3868

[31] Ford, C.; Nilekar, A.U.; Xu, Y.; Mavrikakis, M. Surf. Sci. **2010**, *604*, 1565-1575

[32] Jiang, T.; Mowbray, D.J.; Dobrin, S.; Falsig, H.; Hvolbaek, B.; Bligaard, T.; Norskov, J.K. *J. Phys. Chem. C* **2009**, *113*,10548-10553

[33] Hummelshoj, J.S.; Blomqvist, J.; Datta, S.; Vegge, T.; Rossmeisl, J.; Thygesen, K.S.; Luntz, A.C.; Jacobsen, K.W.; Norskov, J.K. *J. Chem. Phys.* **2010**, *132*, 071101

[34] Taylor, C.D.; Neurock, M.; Scully, J.R. *J. Electrochem. Soc.* **2011**, *158*, F36-44.

[35] Grabow, L.C.; Hvolbaek, B.; Noskov, J.K. *Top. Catal.* **2010**, *53*, 298-310.

[36] Koch, W.; Holthausen, M.C. *A Chemist's Guide to Density Functional Theory, 2nd ed.*, Wiley-VCH: Weinham, **2001**

[37] Kua, J., Goddard, W. A., *J. Am. Chem. Soc*. **1999**, *121*, 10928 – 10941.

CHAPTER 6

A DFT Investigation on Nickel Alloy Catalysts for Application in Direct Propane Fuel Cells

Shadi Vafaeyan, Alain St-Amant, Marten Ternan

Abstract

If direct hydrocarbon fuel cells (containing polymer electrode membranes) operate at temperatures greater than the boiling point of water it is possible to use non-precious metal catalysts. Nickel alloys were examined for both the propane dehydrogenation reaction and the water dissociation reaction by performing density functional theory calculations. The activation energies or barrier heights of the transition states were determined in an attempt to identify a catalyst having an improved performance. The adsorption energies of both propane and water adsorption decreased as the Fe content of Ni/Fe alloys increased. They both increased as the Cu content of Ni/Cu alloys increased. The activation energy for water dissociation decreased markedly as the energy of adsorption decreased. In contrast there was almost no change in the activation energy for propane dehydrogenation even though the adsorption energy changed substantially. The activation energy for water dissociation on Ni/Fe alloys was found to decrease as the charge on a transition state water molecule's oxygen atom decreased.

6.1 Introduction

In principle fuel cells can convert the chemical energy of a fuel into electrical energy more efficiently than competing technologies such as batteries or combustion processes. The use of hydrocarbon fuels might be even more efficient than the most frequently used fuels, hydrogen and methanol.

We have been investigating the use of hydrocarbons fuels (natural gas for urban areas and liquefied petroleum gas, LPG, for rural areas) that would react directly at the anode of the fuel cell. Direct hydrocarbon fuel cells, DHFCs, have several advantages over hydrogen or methanol fuel cells. The cost of delivering conventional electrical power in rural areas is about an order of magnitude greater than in urban areas, even though the price charged for electrical power is similar. Therefore in real terms, a greater capital cost for fuel cells can be justified for rural areas than for urban areas. For that reason we are investigating DHFCs that operate on propane, direct propane fuel cells, DPFCs. Despite their many advantages, DHFCs have one substantial drawback. They have much smaller current densities (reaction rates) than fuel cells using hydrogen or methanol.

There are three reviews [1-3] that describe the extensive research done on DHFC's during the 1960's. Because that research did not produce the breakthrough that was needed, interest in the topic diminished although work has continued to the present time [4-5]. Our group's strategy includes fuel cell reactor modeling using computational fluid dynamics, CFD [6-8], fuel cell catalyst modeling using density functional theory (DFT) [9], and experimental work with high temperature polymer-ion-conductor composite

electrolytes [10].

The reaction at the anode defines the essence of a DHFC. It is the electro-oxidation reaction of propane; our version of which is shown as Equation 6.1. Propane reacts with water on the anode surface, producing carbon dioxide, protons and electrons.

$$C_3H_8(g) + 6\ H_2O(g) \rightarrow 3\ CO_2(g) + 20\ H^+(ZrP) + 20\ e^-(Me) \qquad (6.1)$$

where ZrP represents a solid zirconium phosphate electrolyte phase, $Zr(HPO_4)_2 \cdot H_2O$, and Me represents the solid transition metal electro-catalyst. This is a multistage reaction network with a complex mechanism involving several intermediate reaction steps (dissociative chemisorption of propane, dissociative chemisorption of water, dehydrogenation, hydroxylation of adsorbed carbon species, and carbon-carbon bond cleavage) through which production of a number of intermediate by-products (such as propanol, propionaldehyde, propionic acid, ethanol, acetaldehyde, acetic acid, methanol, formaldehyde, formic acid, carbon monoxide, and carbon dioxide) is possible.

Polymer electrolyte membrane fuel cells, PEMFCs, are one of the more common types. They require precious metal catalysts because they operate near 80°C with an acidic electrolyte in the presence of water in the liquid phase. Pt, Ir, Au, and Pd are the only metals that are stable in this acidic environment at +0.8 to +1.0 V [11]. Our laboratory work has shown that a zirconium phosphate-glycerol electrolyte [12] can operate at temperatures above the boiling point of water (120 - 200°C). Corrosion should

be less severe in the absence of liquid phase water, so that non-precious metal electro-catalysts should be viable. We have also been investigating nickel metal as an anode catalyst. Nickel is relatively inexpensive and has been used successfully in alkaline fuel cell anodes. Some catalysts used in non-fuel cell applications are known to have large nickel contents (well in excessive of one mono-layer) that do not require careful dispersion of small metal particles [13].

Our research approach includes a search for improved non-precious anode catalysts. Better catalysts are those that have smaller activation energies and ideally are less expensive. Density functional theory was used to determine activation energies, the energy needed to overcome the transition state barrier, E_{act}.

A number of DFT studies on various fuel cell reactions have been reported in the literature. Some examples are: the oxygen electro-reduction reaction [14], the hydrogen electro-oxidation reaction in hydrogen fuel cells [15], the electro-reduction reaction in the presence of liquid water [16], and the methanol electro-oxidation reaction in methanol fuel cells [17]. The synergy between computational studies and experimental studies for fuel cells has been described recently [18].

The focus of this work has been on the use of metal-alloys as bi/multifunctional anodic catalysts capable of simultaneous reaction steps in the propane electro-oxidation process. There are many studies investigating multifunctional metal-alloys as electro-catalysts in fuel cells, including the following topics: an anode material for low

temperature fuel cells [19], carbon poisoning of cathode electro-catalyst alloys in SOFCs [20], the effect of the electro-catalyst on the oxygen reduction reaction [21-22], anodic methanol electro-oxidation reaction on clusters of 2nd and 3rd row group VIII transition metals and Pt-Ru alloys [23]. The latter is a study by Kua and Goddard [23], showing that methanol oxidation is most facile on Pt but that Pt has the least tolerance to CO and that Pt catalyzes methanol decomposition and Ru catalyzes water dissociation.

The objective of this work was to investigate non-precious metal alloys as possible multifunctional anodic catalysts by performing DFT computations. Nickel and iron are both 3d non precious metals. Ni is in the same group as Pt and Fe is in the same group as Ru (VIII). Various ratios of Ni/Fe alloys were examined for both the propane dehydrogenation reaction and the water dissociation reaction. Less emphasis was placed on Ni/Cu alloys. Copper is different than iron in that Cu has one more d-electron than Ni, while Fe has two fewer d-electrons than Ni.

6.2 Methodology and Computational Details

Quantum chemical computations were performed, employing SIESTA software [24], using Kohn-Sham density functional theory (DFT). The generalized gradient approximation method (GGA) was used as the exchange correlation functional type, with Becke, Lee, Yang, Parr (BLYP) parameterization. The default basis set was a double-ζ polarization set composed of a compact and a diffused orbital basis. The default value of 100 Rydberg (1300 eV) was used for the mesh cutoff energy. A 4×4×4 (4*4*4/2=32 k-points) Monkhorost-Pack [25] *k*-point mesh was used. The convergence as a function of

the number of *k*-points was carefully monitored. Increasing the k-point mesh from 32 k-points to 48 k-points changed the adsorption energies by an insignificant amount (~4×10^{-5} eV or ~8×10^{-3} kJ/mol). The atomic coordinates of the adsorbed species were allowed to relax to determine the geometry having the minimum energy. If the change in energy was less than 10^{-3} eV, and if the change in the maximum atomic force was less than 0.01 eV/Å, between successive calculations, then the convergence criteria were attained and the atomic geometry optimized.

The pseudopotentials for nickel and iron were generated using the ATOM program of SIESTA. The Perdew Burke Ernzerhof (PBE) [26] exchange correlation was used for the generation of the electronic configuration. The Improved Troullier-Martins (tm2) [27] method was used to generate the pseudopotential files for the two metals in their non-polarized ground state electron configurations. The pseudopotential input file for each metal required a particular core radius, r_c, to be specified. This was obtained by trial and error. If an initial r_c value was too small ($\leq$ 1.5 for metals used in this study), the pseudopotential could not be generated. After a trial r_c value slightly greater than the minimum acceptable value had been obtained, the software would generate an exact r_c value. That r_c value (3.34 bohr for nickel, 3.18 bohr for copper, and 3.64 bohr for iron) was then used to generate a valid pseudopotential. The pseudopotential output file was used for all the subsequent computations.

DFT calculations were performed on a system of periodically repeated entities, defined in terms of metal unit cells. Each entity consisted of one or two adsorbed species

(e.g. OH, C_3H_7, etc.) on the surface of a thin layer slab of the metal atoms. A metal two-layer thin film slab having a (100) surface was used in all calculations. The entities were a 4×4×10 arrangement for pure iron with a bcc crystal structure and two atoms per unit cell (4*4*2 = 32); and a 3×3×10 arrangement for fcc metal slabs (pure nickel, copper and metal alloys) with 4 atoms per crystal unit cell (3*3*4 =36). Nine of the 10 metal unit cells in the z-direction were empty and together they constituted the vacuum layer. In calculations with pure nickel or metal alloy slabs the adsorbed species of interest was located on a nickel atom in the top layer of the slab. Similarly in calculations with pure Fe or Cu atoms the adsorbed species of interest was located on an atom in the top layer of the slab. In the top layer of the Ni/Fe or Ni/Cu metal alloy slabs containing ~2.8% of Fe or Cu, a Fe or Cu atom replaced one of the Ni atoms adjacent to the Ni adsorption/reaction site. In the Ni/Fe and Ni/Cu metal alloy slabs having an ~22% Fe or Cu content, Fe or Cu atoms replaced the Ni atoms that were the eight nearest neighbours to the Ni adsorption/reaction site (4 in the bottom layer and 4 in the top layer).

The adsorption energies (E_{ads}) of the adsorbates (initially adsorbed reactants and subsequent adsorbed intermediate species) on the metal slabs were calculated according to Equation 6.2.

$$E_{ads} = (E_{adsorbate+slab})_{MIN} - E_{adsorbate(g)} - E_{slab} \quad (6.2)$$

where $E_{adsorbate+slab}$ is the total electronic energy for the absorbate plus metal slab and $(E_{adsorbate+slab})_{MIN}$ is the total electronic energy for the configuration of the adsorbate plus

metal slab that has the minimum energy, $E_{adsorbate(g)}$ is the electronic energy of the adsorbate molecule in the gas phase, E_{slab} is the electronic energy for a metal slab, and E_{ads} is the electronic energy for adsorption of the species on the surface of the metal slab (or heat of adsorption).

The activation energy (energy barrier), E_{act} for each reaction was obtained by calculating $E_{adsorbate+slab}$ as a function of the adsorbate-slab bond length. For each $E_{adsorbate+slab}$ calculation for a particular fixed bond length between the adsorbate and the slab, the value of the adsorbate-slab bond length was maintained constant, while all other bond lengths and all bond angles in the adsorbed species were relaxed to obtain the adsorbate configuration having the minimum energy for that particular adsorbate-slab bond length. Subsequently the resulting energies that had been calculated at each adsorbate-slab bond length were compared as a function their bond lengths. The configuration of the adsorbed species having the maximum energy, $(E_{adsorbate+slab})_{\mathrm{MAX}}$, was the transition state (TS). The activation energies (energy barriers) were obtained using Equation 6.3.

$$E_{act} = (E_{adsorbate+slab})_{MAX} - (E_{adsorbate+slab})_{MIN} \quad (6.3)$$

Variations in the electrical potential of the slabs were not considered (zero electric field).

6.3 Results and Discussions

Figure 6.1 shows the top view of the optimized structures of propane adsorbed on the

Ni/Fe alloy slabs. Propane is adsorbed in a similar manner on all of the Ni/Fe alloy slab surfaces. The three carbon atoms in propane are aligned with the parallel rows of the Ni metal atoms in the pure Ni slab, Fig 6.1a. As the Ni/Fe atomic ratio decreases the alignment of the propane molecule becomes somewhat tilted with respect to the parallel rows of the metal atoms, Fig. 6.1b -6.1d. The greatest tilt in alignment is on the surface of the pure Fe slab. Both Ni and Fe have four fold symmetry but their crystal structures are different. Ni has an fcc structure while Fe has a bcc structure. In the first three images in Figure 6.1, the slabs have an fcc structure where the Fe atoms have replaced Ni atoms in that structure.

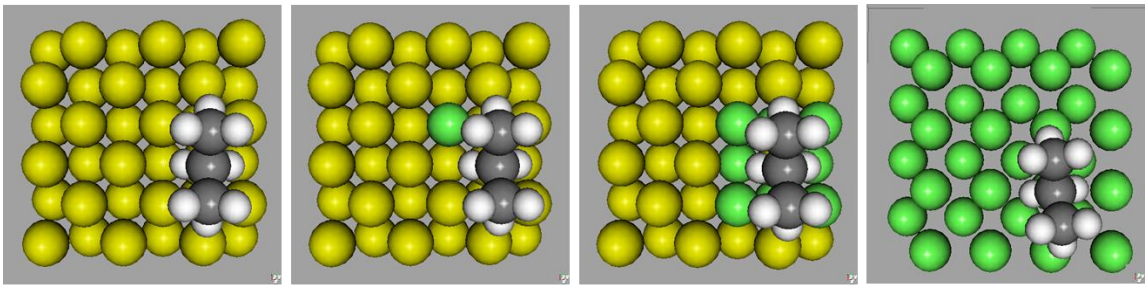

Figure 6.1: Propane adsorbed on the surface of Ni/Fe alloy anode slab (top view) with compositions of *(a)* 0% Fe (pure Ni slab), *(b)* 2.8% Fe, *(c)* 22.2% Fe, and *(d)* 100% Fe

The propane adsorption energies are plotted in Figure 6.2 as a function of the Fe content in the slab. As the Fe content of the slab increases, the energy of adsorption, $-E_{ads}$, goes through a minimum. The diamond shaped data points represent alloys having ordered structures that have been defined. The datum point at 2.8 % Fe is for a slab in which one of the Ni atoms has been replaced with a Fe atom that is adjacent to the Ni adsorption site, i.e. the Ni metal atom on which the central carbon atom of the propane molecule is adsorbed. Even the presence of one Fe atom adjacent to the Ni adsorption site

causes a small decrease in the adsorption energy. The datum point at 22.2 wt % Fe is for a slab in which the eight nearest neighbours to the Ni adsorption site have been replaced by Fe atoms. In this case the decrease in adsorption energy is much more pronounced.

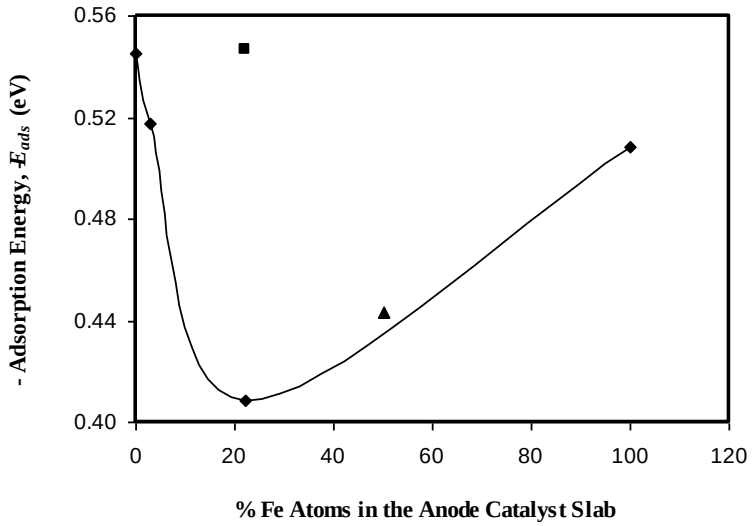

Figure 6.2: DFT calculated adsorption energies of propane on the surface of Ni/Fe alloy slabs with various compositions. The "♦" shaped data points represent slabs having ordered structures. The "▲" represents a slab containing 50% Ni and 50% Fe. The "■" represents a 22.2% Fe slab where the 8 Fe atoms have arbitrary locations and are further from the Ni adsorption site.

The square datum point represents a slab of 22.2 wt% Fe atom in which the 8 Fe atoms have arbitrary locations in the slab. In this case most of the Fe atoms are not close to the Ni adsorption site. The adsorption energy is similar to that of the pure Ni slab. This suggests that an Fe atom needs to be adjacent to the Ni adsorption site if it is to influence the adsorption energy.

The triangular datum point represents a slab in which one-half of the Ni atoms in each

layer were replaced by Fe atoms. However Fe locations were arbitrary. The ordered structures represented by the diamonds may be considered to be "designer" adsorption sites. In contrast the result for a 50/50 Ni/Fe alloy with arbitrary Fe atoms locations suggests a specific location may not be important as long as there is sufficient Fe in the slab. It also suggests that a specialized technique for preparing the alloy may not be necessary.

In Figure 6.3, replacing Ni atoms in the slab by Cu (with the same ratios as the Ni/Fe alloy slabs) causes a maximum in adsorption energy as opposed to the minimum observed in Figure 6.2. The opposite effect maybe related to the number of d electrons in the metal. Copper has one more d electron than nickel. In contrast, iron has two fewer d electrons than nickel.

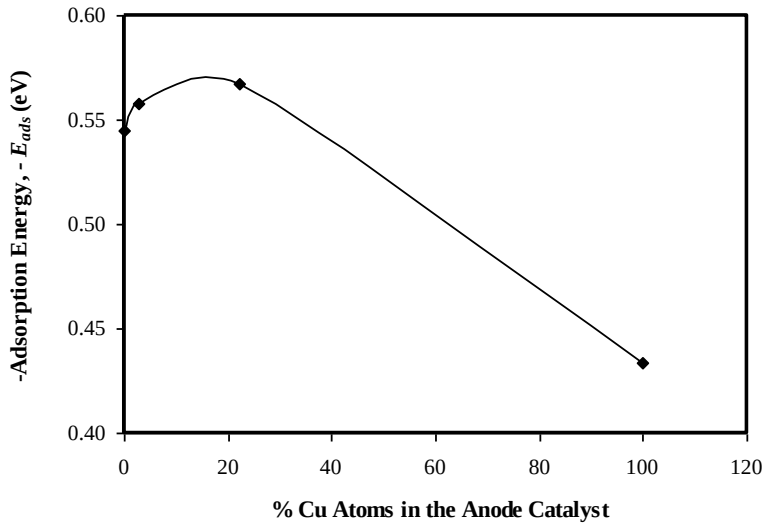

Figure 6.3: DFT calculated adsorption energies of propane on the surface of Ni/Cu alloy slab with various compositions (0%Cu, 2.8%Cu, 22.2%Cu and 100%Cu)

The adsorption of water on four different Ni/Fe alloy slabs is shown in Figure 6.4. A

slight change in orientation of the water molecule on the metal surface can be observed as the Fe content of the Ni/Fe alloy increases. The orientation of the water molecule on the Fe (100) surface is clearly different than on the Ni (100) surface.

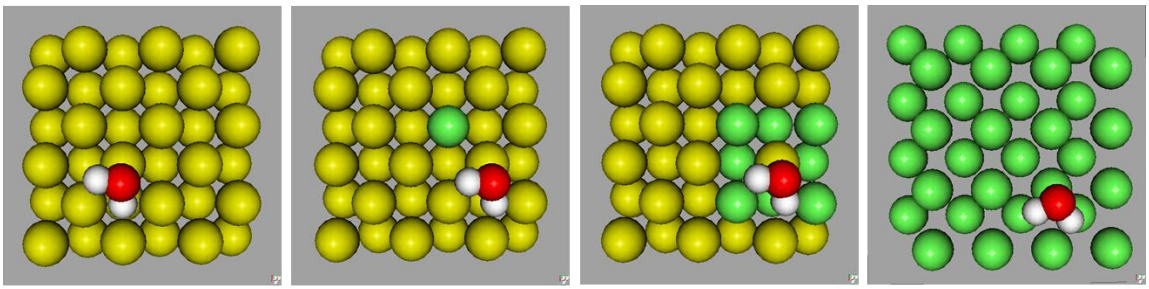

Figure 6.4: Water adsorbed on the surface of Ni/Fe alloy anode slab (top view) with compositions of *(a)* 0% Fe (pure Ni slab), *(b)* 2.8% Fe, *(c)* 22.2% Fe, and *(d)* 100% Fe

The water adsorption energies are plotted in Figure 6.5 as a function of the Fe content in the slab. As the Fe content of the slab increases, the energy of adsorption, $-E_{ads}$, goes through a minimum. The shape of the plot is similar the one for the adsorption of propane on Ni/Fe alloys.

The water adsorption energies are plotted in Figure 6.6 as a function of the Cu content in the slab. As the Cu content of the slab increases, the energy of adsorption, $-E_{ads}$, goes through a maximum. The shape of the plot is similar the one for the adsorption of propane on Ni/Cu alloys.

The energy of adsorption appears to be a function of alloy composition. Both the propane and water adsorption plots have the same general shape for both Ni/Fe and Ni/Cu alloys. Changing the alloy composition from Ni to Ni/Fe or Ni to Ni/Cu causes the

Same directional changes in energy of adsorption for both propane and water.

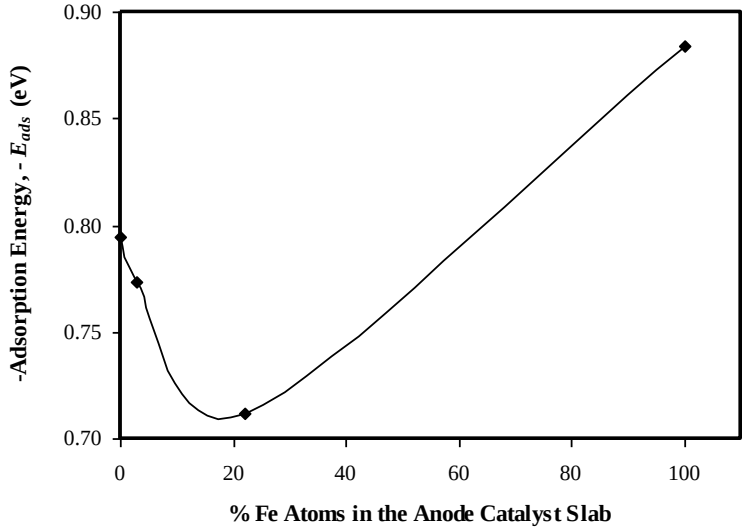

Figure 6.5: DFT calculated adsorption energies of water on the surface of NiFe alloy slab with various compositions (0%Fe, 2.8%Fe, 22.2%Fe and 100%Fe)

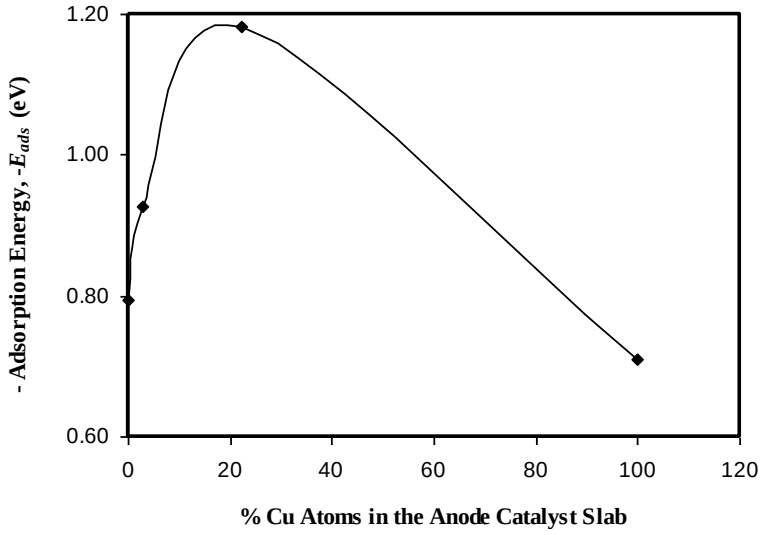

Figure 6.6: DFT calculated adsorption energies for water on the surface of Ni/Cu alloy slabs having various compositions (0%Cu, 2.8%Cu, 22.2%Cu and 100%Cu)

The activation energies for the propane dehydrogenation reaction on Ni/Fe alloy slabs (with the same compositions used above for investigating the adsorption energies) were

calculated using Eq. 6.3. In Figure 6.7 the energy plot for dehydrogenation of propane as a function of the C-H bond distance on propane central carbon, on the surface of Ni slab, is shown. This plot demonstrates the method used to determine the activation energies for propane dehydrogenation and water dissociation.

The results for activation energy (energy barrier) calculations for propane on slabs having different Ni/Fe compositions are shown as the energy plot in Figure 6.8. As the Fe content of the slab increases, the activation energy goes through a maximum. Since the smallest activation energies are obtained with either pure nickel or pure iron, it appears that Ni/Fe alloy catalysts are not helpful for propane dehydrogenation.

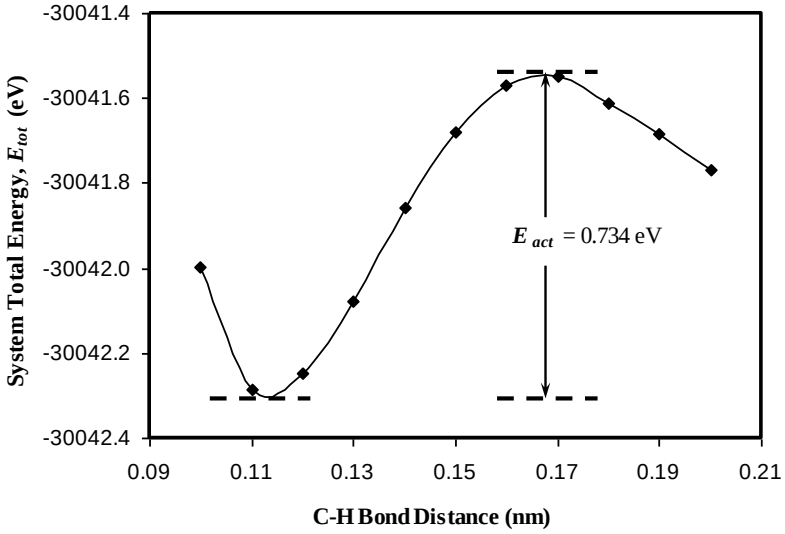

Figure 6.7: Energies of the adsorbate plus slab where the central carbon atom of the adsorbate had a defined C-H bond length. All the other bond lengths and all the bond angles in the adsorbate were permitted to relax

The activation energy for the water dissociation reaction is shown in Figure 6.9. There was a substantial decrease in activation energy as the Fe content in the Ni/Fe alloys

increased. This indicates that Ni/Fe alloy catalysts will be superior to the pure component catalysts for the water dissociation reaction. The combined data in Figures 6.8 and 6.9 suggest that an ideal catalyst might contain small domains of pure metal for propane dehydrogenation adjacent to small domains of Ni/Fe alloys for the water dissociation reaction.

Activation energies are plotted as a function of adsorption energies in Figure 6.10. For propane dehydrogenation there is almost no change in activation energy. However, for water dissociation the activation energy decreases substantially as the adsorption energy decreases. Small energies of adsorption may not always be desirable, since they can be associated with ease of desorption. However, water is different than propane in that no fuel content is lost when water is desorbed.

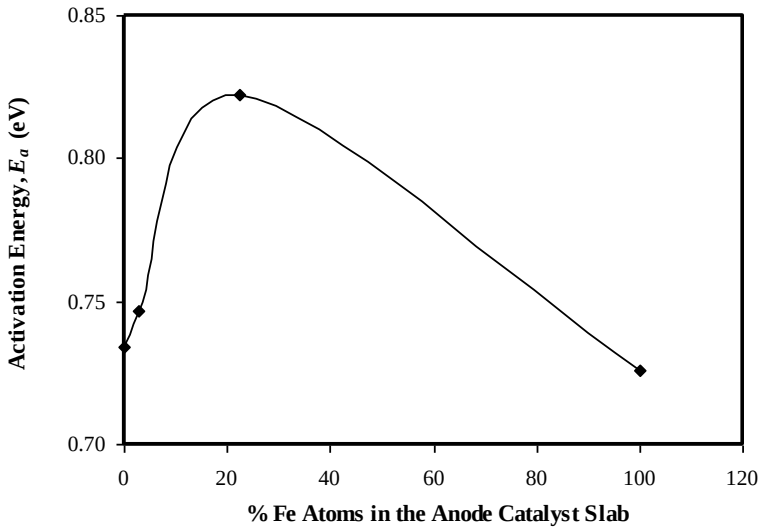

Figure 6.8: DFT calculated activation energy plot, E_{act} (eV), for the dehydrogenation of propane, $*C_3H_8 \rightarrow *C_3H_7 + *H$ (* indicates the species is adsorbed on the surface of the catalyst) for various compositions of Ni/Fe anode catalyst slabs (0%Fe, 2.8%Fe, 22.2%Fe and 100%Fe)

Mulliken charge population calculations were performed on the adsorbed water species in the transition states shown in Figure 6.11. The Mulliken charge population provided the charge (number of valence electrons) on the O atom in the adsorbed H_2O species at the transition state, q(O). In all cases it was slightly less than 6. It is to be noted that an isolated oxygen atom in vacuum, far removed from other materials has 6 valence electrons. The quantity "6 – q(O)" is proportional to charge transferred from the O atom in the adsorbed H_2O species transition state and is shown in Figure 6.11. The activation energy was correlated with this quantity. The smaller the charge on the O atom in the adsorbed H_2O species transition state, the smaller the activation energy will be. Therefore the correlation in Figure 6.11 indicates that it is desirable to transfer charge from the O atom of the adsorbed water species.

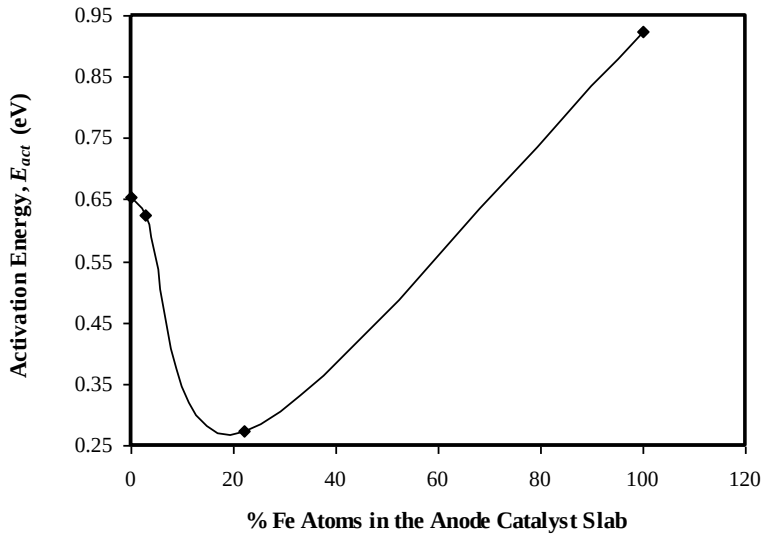

Figure 6.9: DFT calculated activation energy plot, E_{act} (eV), for water dissociation, $*H_2O \rightarrow *OH + *H$ on Ni/Fe anode catalysts of various surface compositions (0%Fe, 2.8%Fe, 22.2%Fe and 100%Fe)

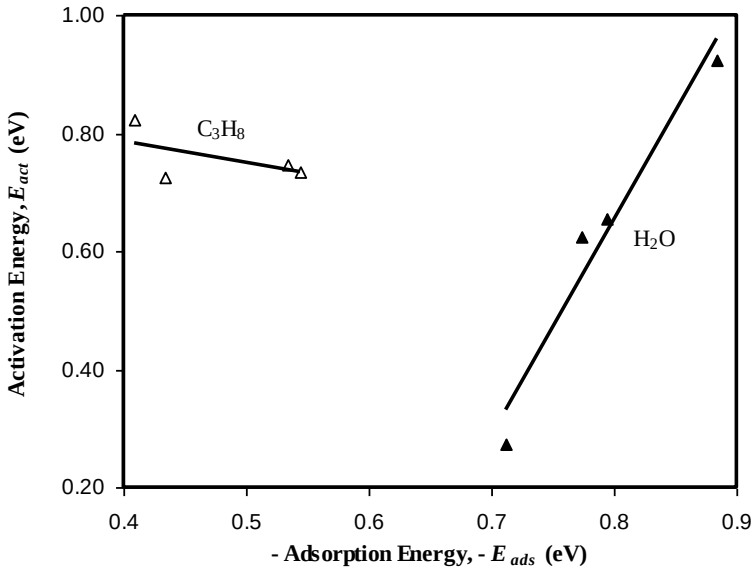

Figure 6.10: Activation energy, E_{act} (eV), versus adsorption energy, -E_{ads} (eV), for propane dehydrogenation, "▵" and for water dissociation, "▲"

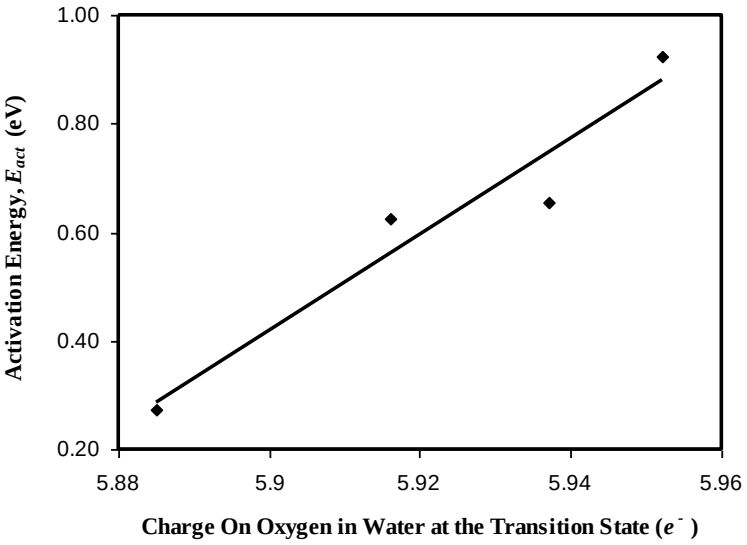

Figure 6.11: Activation energy of water dissociation, E_{act} (eV), versus change on oxygen of water at the transition state, on pure Ni and Fe, and two NiFe slabs (0%Fe, 2.8%Fe, 22.2%Fe and 100%Fe)

6.4 Conclusions

The objective in this work was to identify an improved catalyst for the anode of a DHFC. The improvement was to be identified by an increase in the exchange current density (catalytic reaction rate) that would be caused by a decrease in the activation energy or the barrier height of the reactions. For the water dissociation reaction, E_{act} decreased when the energy of adsorption, E_{ads}, decreased. E_{ads} decreased as the Fe content of Ni/Fe alloys increased. In contrast E_{ads} increased when the Cu content of Ni/Cu alloys increased. For the propane dehydrogenation reaction, E_{act}, was invariant with E_{ads}. Therefore Ni/Fe alloy catalysts have been identified as promising catalysts for the water dissociation reaction at the anode of a DPFC.

A Mulliken charge population analysis indicated that for water dissociation E_{act} was related to the charge on the oxygen atom of water molecules in their transition state configuration. E_{act} was found to decrease as more charge was transferred off of the oxygen atom of the water molecule in its transition state.

6.5 References

[1] Liebhafsky, H. A.; Cairns, E. J. *Fuel Cells and Fuel Batteries: a Guide to Their Research and Development*; Wiley: New York, **1968**.

[2] Bockris, J. O.; Srinivasan, S. *Fuel Cells: Their Electrochemistry* McGraw-Hill: New York, **1969**

[3] Cairns, E. J.: *Adv. Electrochem. Electrochem. Eng.* **1971**, *8*, 337-392.

[4] Heo, P.; Ito, K.; Tomita, A.; Hibino, T. *Angew. Chem. Int. Ed*. **2008**, *47*, 7841-7844.

[5] Murray, E. P.; Tsai, T.; Barnett, S. A. *Nature*, **1999**, *400*, 649-651.

[6] G. Psofogiannakis, Y. Bourgault, B.E. Conway, and M. Ternan, J. Appl. Electrochem. **2006**, *36*, 115-130.

[7] Khakdaman, H.; Bourgault, Y.; Ternan, *Ind. Eng. Chem. Res.* **2010**, *49*, 1079-1085.

[8] Khakdaman, H.; Bourgault, Y.; Ternan, M. *J. Power Sources* **2011**, *196*, 3186-3194.

[9] Psofogiannakis, G.; St-Amant, A.; Ternan, M. *J. Phys. Chem. B* **2006**, *110*, 24593-24605.

[10] Al-Othman, A.; Tremblay, A. Y.; Pell, W.; Letaief, S.; Burchell, T. J.; Peppley, B. A.; Ternan, M. *J. Power Sources* **2010**, *195*, 2520-2525

[11] Stolbov, S.,; Ortigoza, M.A.; *J. Phys. Chem. Lett.* **2012**, *3*, 463-467

[12] Al-Othman, A.; Tremblay, A.Y.; Pell, W.,; Liu, Y.; Peppley, B.A.; Ternan, M.; *J. Power Sources*, 2**012**, *199*, 14-21

[13] Wilson, M.F., Mainwaring, P.R., Brown, J.R., Kriz, J.F., *Appl. Catal*. **1988**, *41*, 177 – 198

[14] Tian, F, Anderson, A.B., *J. Chem. Phys*. C, **2011**, *115*, 4076-4088.

[15] Skulason, E., Tripkovic, V., Bjorketun, M.E., Gudmundsduttir, S., Karlberg, G., Rosseisl, J., Bligaard, T., Junsson, H., Norskov, J.K., *J. Phys. Chem. C*. **2010**, *114*, 18182-18197.

[16] Sha, Y., Yu, T.H., Merinov, B.V., Shirvanian, P., Goddard, W.A., *J. Phys. Chem. Lett*. **2011**, *2*, 572-576.

[17] Ferrin, P., Mavrikakis, M., *J. Am. Chem. Soc*. **2009**, *131*, 14381-14389.

[18] Zawodzinski, T., Wieckowski, A., Mukerjee, S., Neurock, M. *Electrochem. Soc. Interface*, **2007**, *16[2]*, 37-41.

[19] Christoffersen, E., Liu, P., Ruban, A., Skriver, H. L., and J. K. Nørskov, J. K.; *Journal of Catalysis*, **2001**, *199*, 123-131

[20] Nikolla, E., Schwank, J., Linic, S.; *Journal of Catalysis*, **2007**, *250*, 85-93

[21] Vukmirovic, M. B., Zhang, J., Sasaki, K., A.U. Nilekar, A. U., Uribe, F., Mavrikakis, M., Adzic, R. R.; *Electrochimica Acta*, **2007**, *52*, 2257-2263

[22] Nørskov,J. K., Rossmeisl, J., Logadottir, A., Lindqvist, L., Kitchin, J. R., Bligaard, T., Jonsson, H.; *J. Phys. Chem. B.*, **2004**, *108*, 17886-17892

[23] Kua, J., Goddard III, W. A.; *J.` Am. Chem. Soc.*, **1999**, *121*, 10928-10941

[24] Soler, J.M., Artacho, E., Gale, J.D., Garcia, A., Junquera, J., Ordejon, P., Sanchez-Portal, D. *J. Phys.: Condens. Matter*. **2002**, *14*, 2745-2779.

[25] Monkhorst, J. H.; Pack, J. D.; *Phys. Rev. B* **1976**, *13*, 5188

[26] Perdew, J. M., Burke, K., Ernzerhof, M. *Phys. Rev. Lett*. **1996**, *77*, 3865-3868

[27] Troullier, N.; Martins, J. L.; *Phys. Rev. B* **1991**, 43, 1993

CHAPTER 7

An Overview of the Thesis

Three DFT studies are reported on the performance of nickel based catalysts for use as the anode of a direct propane fuel cell. The first was a study of propane adsorption on 3d metals. The second was an examination of a partial reaction network in which propane and water react. The third was a study of nickel alloy catalysts.

The focus of the first study (Chapter 4) was to identify a non precious metal catalyst that could be used as the anode catalyst of a DPFC. The first step of any catalytic surface reaction is the adsorption of the reactant on the surface of the catalyst. If this does not happen no reaction will occur on the surface. One of the first steps in propane electro-oxidation process was the chemisorption of propane on the surface of 3d metals, Fe, Co, Ni, Cu and Zn. The adsorption energies of propane on the 3d metals exhibited the form of a volcano plot, with nickel having the highest adsorption energy at the peak of the volcano curve (Fig. 4.3). The DFT result reported in this work suggests there is a fundamental reason for the choice of Ni for alkaline fuel cell anodes. Also the adsorption energy values for propane, which is an alkane, were consistent with those for alkenes and alkynes in that they had magnitudes that were less than those in the literature data for light-weight hydrocarbons with double and triple bonds.

Two geometric factors related to metal crystal structure and geometry were observed

as a result of these propane adsorption studies. The metals studied were categorized into two groups: those with surfaces having 4-fold and those having 3-fold symmetry. Adsorbed propane had a different configuration on the surfaces of each symmetry type. On the 4-fold symmetry metals the two end carbons were elevated equally from the surface and were further from it compared to the central carbon atom. This indicates that the metal surface interacts more strongly with the propane central carbon atom than with the two end carbon atoms (Fig 4.1). In contrast, the central carbon atom and one of the end carbon atoms sat parallel to the surface of 3-fold symmetry metals and only one end carbon was elevated from the surface. This indicates that the 3-fold symmetry metals interact more strongly with both the central carbon atom and one of the end carbons of propane, than with the second end carbon atom that is elevated from the surface (Fig. 4.2). This geometric effect result was also supported by Mulliken charge analysis (Fig. 4.7)

The second geometric factor was the observation of an inverse relationship between the adsorption energy and the distance between the propane central carbon and the edge of the metal surface. Two parallel (same slope) linear lines were obtained; one for the 3-fold and one for the 4-fold symmetry surfaces (Fig. 4.8). Both of these lines showed that there was a large change in adsorption energy with slight variations in this distance. Nickel was the metal with the shortest distance between metal-surface edge and propane central carbon atom. That was consistent with Ni having the largest propane adsorption energy.

It was also observed that the bond distance between the propane central carbon and the hydrogen atom being removed was longer on the nickel (100) surface than on the other metal surfaces. The long carbon–hydrogen bond suggests that this configuration for the adsorbed propane species on nickel may be further away from the reverse reaction, desorption, than the configurations on any of the other metal surfaces. The combined criteria of (a) configuration of the adsorbed propane species and (b) heat of adsorption suggest that a nickel catalyst may be the best candidate for a comparatively inexpensive anode material that might replace comparatively expensive Pt in a DPFC.

The second study (Chapter 5) was an investigation of the nickel (100) surface as a catalyst for some of the early steps in the complex propane electro-oxidation network of reactions. Two important issues in the propane electro-oxidation process were addressed. The first was to establish that these reaction steps occurred readily on a nickel catalyst. The reactions studied were, water dissociation (Fig. 5.5-5.7) to form hydrogen radicals and hydroxyl radicals, dehydrogenation of propane to form propyl radicals (Fig. 5.2-5.4), dehydrogenation of propyl radicals to form ally radicals (Fig. 5.8-5.10), and propanol formation (Fig. 5.11-5.13) from the reaction between propyl and hydroxyl radicals. Second for the overall reaction to go towards completion, the reactants and intermediate products must remain adsorbed on the metal catalyst surface and not desorb as partially oxidized products. Based on these primary steps, the second concern was to identify whether or not CO_2 was going to be the predominant final product. If so reaction of propyl radicals to allyl radicals would have to be favourable compared to their reaction to propanol, a partially oxygenated species.

Based on the calculated DFT energy barriers, the dehydrogenation of propyl radicals to form allyl radicals (Fig. 5.9) was found to be more likely than formation of propanol gas (Fig. 5.13). The formation of an allyl radical from a propyl radical only requires one elementary reaction step. In contrast the formation of gas phase propanol requires three elementary reaction steps (water dissociation, propanol formation on the surface, and its desorption into the gas phase), and hence, significantly more energy. It is important to note that formation of propanol adsorbed on the surface is a difficult task. It has a large energy barrier, in addition, to form adsorbed propanol; the propyl and hydroxyl radicals must get close enough for a bond to form between them. The required close proximity is only possible if they become adsorbed on the same Ni atom. A comparison of the reactions indicated that there was only a slight possibility for gas phase propanol (a partially oxygenated by-product) to form. It was therefore concluded that CO_2 would likely be the predominant product.

The third study (Chapter 6) was an investigation of alternative alloy metal catalysts as possible materials for the anode of DPFC. A second metal, either iron or copper was introduced into the Ni slab. The earlier chapters of this thesis indicated that greater adsorption energies were desired in order to keep species on the surface. On this bases, in chapter 5, the adsorption energies of propane and water on the alloy slabs were examined, however the main criterion was to identify alloy compositions that permit reactions to occur with smaller activation energies (energy barriers). In addition, the effect of adsorption energies of propane and water on the alloy slabs, on the transition state energies of water dissociation and propane dehydrogenation was examined.

The adsorption of both water and propane was examined using Ni/Fe alloy slabs. It was found that both the water and propane adsorption energies decreased as more Fe atoms were introduced into the Ni slab, provided the Fe atoms were near the region of the Ni adsorption site (Figures 6.2 & 6.5). The progression examined was: one Fe atom replacing a Ni atom adjacent to the Ni adsorption site, and all eight nearest neighbours around a Ni adsorption site being replaced by Fe atoms (Figures 6.1 and 6.2). Both water and propane reactants adsorbed more strongly on the surfaces of the Ni and Fe pure metal slabs than on the Ni/Fe alloy slabs with Fe atoms near the region of the Ni adsorption site.

Copper content in Ni/Cu slabs (with the same number of Ni atoms being replaced as in the Ni/Fe slabs), generally had an effect on the water and propane adsorption energies that was opposite to that in Ni/Fe alloys. Both the water and propane adsorption energies decreased with increasing Fe content for Ni/Fe slabs. They increased with increasing Cu content for Cu/Fe slabs (Figures 6.3 & 6.6).

The effect of alloying the Ni slab with Fe on the activation energies was examined for two reactions, water dissociation and propane dehydrogenation (to a propyl radical). The same compositions of the Ni/Fe slabs used to examine the adsorption energy were used for determining activation energies. Increasing the Fe content caused the propane dehydrogenation activation energies to increase. In contrast, increasing the Fe content caused the activation energies for the water dissociation reaction to decrease. Therefore in Ni slabs, Fe was a promoter for the water dissociation reaction (Fig. 6.9) and an inhab-

itor for the propane dehydrogenation reaction (Fig. 6.8).

The above findings suggest that a tri-metal catalyst (composed of Ni, Fe and Cu) may merit investigation. Cu and Fe had opposite effects on both water and propane adsorption energies. The activation energies showed that Ni/Fe alloys promoted the water dissociation reaction and inhibited the propane dehydrogenation reaction. If Cu also had the opposite effect to Fe, both on the water and propane activation energies, a tri-metallic catalyst might be warranted. In that case Fe would promote the water dissociation reaction and Cu would promote the dehydrogenation reaction.

CHAPTER 8

Conclusions

This research was conducted using DFT computations to identify non-precious metal catalysts that might be candidates for use as the anode of DPFCs. The following lists contain: the main conclusions from the three studies that were performed, a list of original contributions to knowledge, and a list of some suggestions for future research.

8.1 Main Conclusions

8.1.1 Chapter 4:

From among the 3d metals investigated, nickel was identified as a promising non-precious metal candidate that might replace platinum in a fuel cell where liquid water is not present and hence corrosion is not a major issue. Among the 3d metals studied propane was adsorbed (chemisorption) most strongly on Ni. A volcano plot was obtained when propane adsorption energies on 3d metals were plotted against the number of 3d electrons in a metal. Two geometric effects were identified. First, two distinct molecular configurations of the adsorbed propane were observed; one on 4-fold symmetry metals and another on 3-fold symmetry metals. This observation was supported by Mulliken charge analyses on both systems. Second, an inverse relationship was found between the adsorption energy and the distance from the adsorbed propane's central carbon atom to the edge of the metal surface for 3d metals. For propane adsorbed on a metal surface, the central carbon atom's C-H bond length varied with the distance from the centre of the carbon atom to the centre of the metal atom on the surface of the metal slab. The Ni surf-

ace had the longest C-H bond length.

8.1.2 Chapter 5:

On a nickel surface, the dehydrogenation of adsorbed propyl radicals to form adsorbed allyl radicals was found to be more likely than the competing reaction of propyl radicals with hydroxyl radicals to form gas phase propanol. This suggested that on a nickel surface most of the reaction intermediates might stay on the surface so that CO_2 might be the predominant product rather than partially oxidized species such as alcohols, aldehydes, carboxylic acids, and CO.

8.1.3 Chapter 6:

The effect of alloying the anode catalyst was examined. Two different bimetallic slabs of Ni/Fe and Ni/Cu (35 atoms Ni / 1 atom Me and 28 atoms Ni / 8 atoms Me, where Me = Fe, Cu) were used. In each of the four cases nickel was the main catalyst and the slab had the Ni fcc structure. In each case some of Ni atoms in the slab were replaced with Fe or Cu atoms. The Ni/Fe and Ni/Cu slabs were used to investigate the adsorption of water and propane on metal surfaces. In addition, propane dehydrogenation and water dissociation reactions were investigated on the Ni/Fe slabs. Increasing the Fe content in Ni/Fe alloys decreased the adsorption energy for both water and propane. In contrast, increasing the Cu content in Ni/Cu alloys increased the adsorption energies for both water and propane. In Ni/Fe slabs, Fe was an inhibitor for propane dehydrogenation and a promoter for water dissociation reactions.

8.2 Contributions to Knowledge

The following is a list of the original contributions to knowledge made during the course of this research.

1. This was the first study of propane adsorption on metal surfaces. Neither experimental nor computational studies were reported in the literature previously.
2. This was the first explanation of volcano plots in terms of two specific geometric factors: (a) distance of an adsorbed species from the edge of a metal surface, and (b) symmetry of the solid surface atoms.
3. 2(a) A linear correlation of heat of adsorption with the distance between the central carbon atom of the adsorbed propane and the metal-surface edge was found.
4. 2(b) 3d metals having 3-fold symmetry were found to have a different correlation line than 3d metals having 4-fold symmetry, although both lines had the same slope.
5. The molecular configuration of adsorbed propane was found to be different on 4-fold symmetry metals than on 3-fold symmetry metals.
6. Among the group 3d metals (Fe, Co, Ni, Cu, and Zn) studied, the Ni surface was found to have the adsorbed propane with the longest C–H bond attached to its central carbon atom.
7. Propyl radicals adsorbed on Ni surfaces were found to be more likely to form allyl radicals than gas phase propanol.
8. This was the first DFT investigation of alloys as possible anode catalysts for the electro-oxidation of propane in DPFCs.

9. This was the first study to show that increasing the Fe content of a Ni slab would decrease the heat of adsorption for both water and propane.
10. This was the first study to show that increasing the Cu content of a Ni slab would increase the heat of adsorption for both water and propane.
11. This was the first study to show that Fe promoted the water dissociation reaction and inhibited the propane dehydrogenation reaction.

8.3 Recommendations for Future Work

Propane has several advantages as an alternative fuel to hydrogen. Since the main deficiency of DPFCs is their slow anodic kinetics, research on the anode catalyst and the anodic electro-oxidation reaction will be necessary if those advantages are to be realized. The following are some recommendations for future work that became apparent during this project.

1. DFT computations should be made to determine the activation energies for the reaction of all of the other intermediates in the overall propane electro-oxidation network.
2. Rate constants should be calculated to determine the rate limiting step in the overall reaction network.
3. The activation energies should be determined for the water dissociation and propane dehydrogenation reactions using Ni/Cu alloys (same compositions as used in this research).
4. Ni/Me alloys (where Me is an alternative 3d metal, Ni is the base catalyst in the slab, and an Ni atom is the reaction site) should be examined to determine their

suitability as catalysts for the intermediate reaction steps in the propane electro-oxidation reaction (propane Bagotzky like mechanism, Appendix A).

5. Different compositions of Fe/Ni alloys (where Fe is the base catalyst, the slab would have bcc crystal structure, with an Fe atom as the reaction site, and with an Ni atom as the reaction site) should be examined to determine their suitability as catalysts for the propane electro-oxidation reaction steps.
6. Membrane electrode assemblies with anodes having some of the catalyst compositions identified in this work should be prepared and tested in a fuel cell test station.

CHAPTER 9

Supplementary Materials

This section covers supplementary materials in excess of the additional materials that were suggested by the examiners during my oral examination on September 13, 2012.

9.1 Experimental Research on Hydrocarbon (Propane) Fuel Cells

9.1.1 Experimental Findings Reviewed by Elton J. Cairns in 1971

An extensive review of experimental studies on hydrocarbon fuel cells, by Elton J. Cairns in 1971 [1], highlights significant findings about this type of fuel cells. Some of these findings that are related to our work (with specific concentration on propane studies in most cases) are outlined below.

1. As a result of several adsorption studies comparing the adsorption of methane, ethane and propane on Pt surfaces in different acidic media, and with the aid of rate constant calculation in a Langmuir-type equation, it was determined that propane adsorbed much rapidly on Pt (from HF) than ethane does (from HClO4) [1].
2. Electro-oxidation of hydrocarbons in DHFC resulted in the formation of three types of intermediate byproducts, called type I, type II, and type III (in different amounts depending on the hydrocarbon being oxidized). Type I or O-type species (e.g. *CHO) are single-carbon, partially oxygenated species of approximate CHO

composition that oxidized near 0.7V, and are not catholically desorbable. Type II or CH-α species (e.g. $*C_3H_7$) are partially dehydrogenated carbon species that oxidized over a much wider range of potentials compared to Type I, centering around 1.2V and are catholically desorbable. Type III or CH-β intermediates (e.g. $*C_2H_2$) with multiple (double/triple) C-C bonds that are slowly oxidized at high potentials, strongly adsorbed on the surface and are not cathodically desorbed [1].

3. A comparison between propane, methane and ethane oxidation on Pt in acidic media (electrolyte) showed that propane forms more type II than does ethane, and the amount of type I materials formed are similar for all three molecules. The rate studies on formation of Type I and II material from propane oxidation on Pt in acidic HF media at 90ºC clearly showed that type I byproducts started to appear on Pt surface after a significant portion of the electrode surface was already covered by type II. These led to the conclusion that since type I species contains one carbon and are partially oxidized; they are produced (along with protons and electrons) from reaction of type II species and water. Clearly the higher potentials were needed for oxidation of type II species compared to type I, and therefore hydrocarbons that form type I species are more readily converted to CO_2 and H^+ via the electrochemical reaction [1].
4. The cathodically desorbed products in DPFC are propane, plus small amounts of methane and ethane. The maximum methane/ethane ratio in the desorbed gas at 100ºC in 85% H_3PO_4 was 0.5. For platinum black in H_2SO_4 at room temperature, about 10% of the desorbed gas is methane and ethane, the remainder Propane. These results show that there is a significant amount of carbon-carbon bond

cleavage during propane oxidation even at room temperature. Smaller hydrocarbon products then proceed to CO_2 production. There is no evidence for the formation of higher hydrocarbons such as C_4H_{10} or C_6H_{14}, hence no oligomerization i.e. C-poisoning [1].

5. Methane is adsorbed only on Pt among all platinoid elements and is adsorbed slowly by a dissociative mode to yield surface species that are partially oxidized (200 $\mu C/cm^2$ required for further oxidation to CO_2). These surface species can be oxidized completely to CO_2 and H^+ at potentials near 0.7V. Ethane adsorption is much more rapid and extensive than methane on Pt black under the same conditions. The rate of Ethane adsorption increases with increasing temperature. Significant amounts of ethane are adsorbed at an appreciable rate only in the presence of a strong acid electrolyte. The adsorption is dissociative with some adsorbed H being formed in the process. There is evidence of the presence of methane among cathodically desorbed products, indicating C-C bond cleavage either during adsorption or during its residence on the catalyst surface. Methane then proceeds to CO_2 production based on previous findings [1].
6. It was found that the rate of oxidation of the hydrocarbon is affected by the surface coverage. The maximum current density was found to occur at a very low surface coverage of type I intermediates and potentials in the range of 0.5-0.6V for C_1-C_4 alkenes at 80-120ºC on 75% H_3PO_4 on Pt black. The overall conclusion on the electrochemical oxidation rate of alkanes was: over the low-potential range of interest for hydrocarbon fuel cells, the electrochemical consumption of alkanes is limited by the electrochemical oxidation of type I intermediates involving a

two-electron rate determining step associated with formation of a C-O bond to yield CO_2 [1].

7. A common reaction mechanism for alkanes alkenes and alkynes was identified. Production of type II intermediates was proposed to be the common first step and the major class of species for all three classes of hydrocarbons. Due to their weaker bonding to the platinum surface, or the lack of multiple (double or triple) C-C bonds, alkanes were found to more readily (compared to alkenes and alkynes) further oxidize to type I species. This surface species is then readily oxidized to CO_2 and this electrochemical reaction is the rate determining step for the steady-state anodic oxidation of alkanes at low potentials. There are two alternative paths for the consumption of type II species: the relatively direct oxidation to CO_2 without accumulation of type I intermediates on the electrode surface, and the further dehydrogenation to form type III intermediates which in turn either accumulates (at low potentials) on the surface, or are oxidized to CO_2 (at high potentials). Based on the rate constants for these three possible reaction path ways for further oxidation of type II byproducts, it was determined that for alkanes (propane in particular) the next step is formation of type I (single-carbon) species, followed by their further oxidation to CO_2 [1].
8. Propane was reported to be economically oxidized on platinum in 5*N* H_2SO_4 at 25ºC to produce CO_2 at 90-100% faradic rate (rate of movement of charged species across the electrolyte) [1].
9. In a study of very large number of organic fuels, as possible directly fed fuels, including C_2H_2, C_2H_4, C_3H_8 on Pd/C and Pt/C catalysts in different electrolytes,

propane gave the best performance in H_2SO_4 [1].

10. It was observed that methane (which adsorbs relatively slowly and to a small extent on the catalyst surface) supports lower maximum current densities than ethane and propane (with propane supporting the highest current densities) [1].
11. Among several normal alkanes, the maximum steady-state rate of hydrocarbon oxidation in fuel cells was observed to be somewhere in the range of ethane to butane in strong acid electrolytes, with propane near the maximum [1].
12. Overall, propane evidently showed the best behavior in terms of rapid adsorption, C-C bond cleavage and further reaction with water to form type I intermediates (following the first oxidation reaction step where type II species are formed), accompanied by a small accumulation of refractory type III species. The alkenes and alkynes either do not form type I or they form it only very slowly, so that the overall rate of oxidation in acid electrolyte is significantly smaller than that of corresponding alkanes (particularly propane). In addition alkenes and alkynes do not undergo C-C bond cleavage to form C_1 species as readily as alkanes and therefore they have tendency to form polymerized higher molecular weight carbon species [1].
13. In studies of electro-catalyst effect on the rate of oxidation of hydrocarbons, Pt showed to be the best catalyst among a number of other anode catalyst candidates. In strong acid electrolytes, Pt showed performances of orders of magnitude better than any other paltinoid element [1].
14. Two approaches taken towards improving the Pt catalyst as the anodic catalyst. First, higher area Pt blacks were prepared by carefully reducing the catalyst (PtO_2,

H_2O). This led to an electro-catalyst capable of supporting as much as 3.5 times current density obtained by the same loading of commercial Pt black for various alkane fuels, particularly for propane. This increased improvement was still insufficient for any economical applications. For example in a propane fuel cell, the cost of this material for the anode was about $1800/kW which was a few orders of magnitude too high for civilian applications. The second approach was to support Pt on corrosion-resistant, electronically conducting material such as graphite, activated carbon black, and a number of other materials. This approach was known to be more effective than the first one. For example for a propane fuel cell, specific currents of 8-5mA/mg of Pt have been achieved. The platinum cost was $220/kW (with a Pt cost of $4/g) at a specific current of 50mA/mg. This is much closer to practical value (but still too high). The cost figures for the electro-catalyst were lowest when propane (as oppose to other hydrocarbons) was used as the fuel [1].

9.1.2 Experimental Research Reviewed by Bockris & Srinivasan in 1969

Bockris & Srinivasan also did a thorough review on studies prior to 1969 [2], of fuel cells and their electrochemistry. The followings comments are based on their review and their remarks of the work that pertains to DHFCs.

They reviewed the work done on hydrocarbon fuel cells under two categories of approaches: an approach from a study of intermediates, and an approach from a study of electrode kinetic parameters. Most researchers working with the first approach, studied

anodic hydrocarbon oxidation based on the intermediate byproducts involved. These researchers found that saturated hydrocarbons (SHCs) will react on the surface of Pt catalysts in high concentrations of H_3PO_4. Different intermediates are produced through several possible parallel reaction pathways all leading to CO_2 production as the final product of complete oxidation of SHCs. The path in which the fastest oxidation of an intermediate occurs controls the rate of the reaction. Based on measured kinetics by this group, it was determined that best SHCs adsorption on the surface of the catalyst happens at about 0.2V and SHCs desorb almost completely below a potential of 0.55V [2].

An extensive amount of research was done using the second approach [2]. However progress on obtaining the mechanism at potentials below 1.0V was not significant. Based on a study of oxidation of propane, *n*-hexane, cyclohexane and 2,2-dimethyl butane in concentrated phosphoric acid (electrolyte) solution at 80 to 150ºC led to the following results. Based on their current-time measurements at fixed potentials, they calculated the surface coverage by the intermediate byproducts to be about 0.1 (10%) regardless of the hydrocarbon used. Furthermore the steady-state rates of oxidation of theses fuels to CO_2 were studied at a fixed potential as a function of the fuel pressure, the activity of water and the potential difference across the double layer. Water activity is a measure of energy status of the water in the system (e. g. as the membrane adsorbs water, its ability to hold a charge (charged species, H^+) increases), defined as the vapor pressure of a liquid (fuel cell membrane in this case) by that of pure water at the same temperature, $a_w=P/P_0$. At a constant potential across the double layer (overpotential of zero) the rate of hydrocarbon oxidation to CO_2 was found to be the highest for propane. At potentials greater than 0.7V

a large inhibition effect was observed. The propane oxidation rate (at 80-130ºC in phosphoric acid) was decreased with increasing current densities. Considering this criterion and the energy of the reaction it was determined that the more likely oxidation mechanism for SHCs is (with RC being the hydrocarbon): [RH ↔ *R + H^+ + e^-], followed by [*R → organic radicals] [2]. They concluded that the chemical decomposition of the radical is the rate limiting step for SHC and the rate determining steps for the alternative reaction pathways are also chemical reactions. This group also determined that a great inhibition effect on the oxidation rate comes is caused by the coverage of the surface by anions (from phosphoric acid) adsorption on the surface. The main conclusion from this study was that the rate determining step for saturated hydrocarbons is a chemical reaction which is a step or two further from the initial adsorption. As a result of their review Bockris & Sirinivasan [2] stated that the electro-oxidation mechanism of many hydrocarbons to CO_2 is relatively simple, and is often a 100% one-path oxidation with simple parameters.

The performance of single fuel cells with straight chain paraffins form propane to octane as the fuel, and 95% phosphoric acid electrolyte at 150ºC was determined based on their polarization curve. The cell performance was decreased as the number of carbon atoms in the chain increased. In another study the same investigation was done for C_1-C_8 (methane to octane) straight chain hydrocarbons. This was done at a cell potential of 0.3V, by plotting the current density versus the number of C atoms in the hydrocarbon. An initial increase of current density with increasing the C numbers was observed up to C_3-C_4 (maximum), and then it started to decrease very rapidly with further increase in

number of carbons ($\leq C_5$) in the hydrocarbon. For methane this was related to the fact that is considered to be highly inert by chemists. As for higher hydrocarbons with higher carbon number, the rapid decrease in current density was associated with the decreases in their solubilities and their diffusion coefficients in the electrolyte. A comparison between straight chain hydrocarbons and other hydrocarbons (branched, cyclic etc.) showed that conversion to CO_2 for straight chain hydrocarbons in acidic media at 150ºC is 100% versus 80% in most cases for other hydrocarbons [2].

Because of propane's high reactivity, it is used in most hydrocarbon fuel cell studies as the fuel. It was shown that Pt is the superior anodic catalyst for oxidation of propane compared to other metals (including some noble metals) by at least two orders of magnitude. One of the disadvantages of DPFC was said to be formation of methane (less electroreactive than propane) due to cracking of the propane on the surface. In order to attain a high DPFC performance, this problem is addressed by suppressing the formation of methane under load, at which the *H atoms (formed due to cracking) are removed by ionization easily and hence the methane formation is prevented [2].

Summarizing their findings on DHFCs, Bockris & Srinivasan [2] stated and suggested the followings. DHFCs generate a maximum power in the region of 0.1 W/cm^2 at temperatures of about 150ºC. The best catalysts are Pt or alloys of Pt (not sufficiently effective as Pt). For these cells to be practical a power density of at least 5 times higher than that reported at that time was required. The main objection to DHFCs is the high cost per kilowatt, and this is mainly due to the requirement of a large loading of Pt

catalysts for efficient and practical cell performance. They suggested however that this objection could be addressed, either by use of electrodes with catalyst localization (since for generation of practical power outputs, most of the current is generated in a small region of the electrode), or by pumping the electrolyte through the electrode. They suggested that either option was expected to reduce the required catalyst loading by 10^2 times (it would also ahelp with preserving the limited Pt resources). The possibility of using other catalysts (excluding metals) was also suggested as a solution. The desirability of hydrocarbon fuel cells is ultimately due to their potential for producing low cost power. Further extensive research is required to make this objective a reality [2].

9.1.3 More Recent Experimental Research on Direct Propane Fuel cells

Since 1960's there have been relatively few investigations on direct hydrocarbon fuel cells, and even fewer on direct propane fuel cells. A summary of these investigations done on DPFCs is provided below.

In 2001 Savadogo & Varela [3] did a study on low-temperature (95ºC) direct propane PEMFC with a low-cost PBI (polybenzimidazole) modified membrane. They made a comparison of the fuel cell performance, first, using three different membranes and second, using three different anode catalyst. The membranes used were H_2SO_4 doped PBI, Nafion 117 modified with silicotungstic acid and non-modified Nafion 117, in all three cases Pt/CrO_3 was used as the anode catalysts. Among the three membranes examined, at the same temperature and at the same potential, the H_2SO_4 doped PBI membrane exhibited the highest current density, followed by the modified Nafion 117. In

comparison the non-modified Nafion 117 performed poorly and exhibited a current density of about 1/3 of that for the H_2SO_4 doped PBI membrane. Their investigation of different anode catalysts was done with Pt/C, Pt-CrO_3/C and Pt-Ru/C. Among these three catalysts, Pt-CrO_3 displayed the maximum power density, followed by Pt-Ru/C with a similar power density. However, the Pt/C based anode catalyst exhibited a power density of about 40% of that for Pt-CrO_3/C [3].

Cheng et al. [4] developed a DPFC with a H_3PO_4-doped PBI membrane and Pt/C anode catalyst that operated at temperatures up to 250ºC. Cheng et al. were able to improve the performance of their DPFC by improving the conditions in the cell. They examined the acid doped PBI membrane under the anhydrous conditions and found that DPFC produced unsustainable current densities. Under these conditions stable intermediates covered the Pt/C catalyst surface blocking the reaction sites and preventing further reactions of the intermediate species towards complete oxidation. They improved the performance (higher current densities) by lightly humidifying the feed stream at 25ºC. This resulted in sustainable and higher current densities compared to DPFC under the anhydrous conditions. The role of water in the reaction sequence was to assist in forming surface bound oxygen-containing C_3 intermediates which then led to C_1 oxygen species and finally to CO and CO_2 as the only carbon-containing products [4].

The effect of the anode catalyst on the behavior of a low-temperature (80ºC) DPFC was investigated by Varela & Savadogo [5]. They used four different anode catalysts, commercial Pt/C and PtRu/C, and labratory-prepared PtOx/C and Pt/C+CrO_3 in the

DPFC (with a Nafion 117 membrane). This investigation was done with different propane/oxygen (PR) ratios. Regardless of the catalyst used the PR=2 resulted in the maximum power density. As for the catalysts, the DPFC with PtOx/C as the anode catalyst displayed the best behavior for the direct catalytic electro-oxidation of propane under most of the operating gas PR ratios [5].

9.2 Propane Adsorption on the Surface of Platinum

A DFT study of propane adsorption on the surface Pt(III) and PtSn alloys was done by Nykänen & Honkala [6] where they obtained and displayed the adsorption energy of propane on these surfaces. They used a GPAW code for their periodic DFT calculations and two different XC functionals, RPBE and vdW-DF. They performed theses calculations on two different propane fractional surface coverages (0.25 and 0.125). They found that in most cases (with different catalysts) propane adsorbed more strongly when the coverage is 25%, this was true regardless of the XC functional used. The maximum adsorption energy for propane was obtained on the surface of Pt3Sn/Pt(111) alloy, at a coverage of 12.5%, when the vdW-DF functional was used in the calculations. With the exception of this case, in general among all alloy catalysts used, Pt(111) was found to be the best catalyst for propane adsorption, using a vdW-DF functional in the calculation, regardless of surface coverage. On the other hand, with RPBE functional Pt3Sn/Pt(111) alloy exhibited the highest energy adsorption energy at a 25% coverage, and in general alloys exhibited better adsorption energies compared to Pt(111) at both surface coverages [6].

The adsorption energies of -0.34 to -0.37 eV for propane on Pt(111) (using a vdW-DF functional) obtained in the above study are of the same order of magnitude and in line with the adsorption energies of -0.37 to -0.55 eV obtained in this research for propane on 3d metals (Fe, Co, Ni, Cu and Zn). Precise agreement of adsorption energies in this research with the ones for Pt(111) in the above study were not expected due to different factors used in the two studies, including different catalysts, surface indices ('100' in this research vs '111'), and different functionals.

9.3 Selectivity of Anode Catalyst with respect to Intermediate Byproducts towards Complete Hydrocarbon Electro-oxidation to CO_2 in DHFC

Complete conversion of a hydrocarbon fuel to CO_2, the total oxidized product, is far more desirable than the formation of partially oxidized products such as alcohols, aldehydes, carboxylic acids, and CO. Several experiments with a platinum anode have shown that CO_2 was the predominant product formed at specific operating conditions. The only product reported was CO_2 when the hydrocarbon fuel was (a) ethylene being fed to a sulfuric acid fuel cell [7], (b) propane being fed to a phosphoric acid fuel cell [8], and (c) methane being fed to a PEMFC [9]. CO_2 was the predominant product when propane was fed to a PEMFC [10]. In contrast when a PEMFC, with a platinum-ruthenium (Pt-Ru) anode, was being fed methane, all of the possible partial oxidation products, CH_3OH, CH_2O, COOH, CO, and CO_2 were formed [4]. Furthermore when a PEMFC with a platinum anode was being fed propane, the major product was CO_2 at cell potentials less than 0.1 V, and CO when the cell potential was greater than 0.4 V.

In the study (described preiously) of an acid-doped PBI electrolyte in a DPFC fuel cell, Cheng et al [4] observed that on a Pt/C catalyst and under slightly humidified anode conditions the electro-oxidation of propane will progress to completion with the only two carbon-containing products being CO and CO_2. They suggested that these species are formed either by direct reaction of propane with adsorbed water (which leads to formation of surface bound oxygen-containing C_3 and then C_1 hydrocarbon species, and then to CO and CO_2), or by adjacent Pt-OH species (derived from reaction of water with Pt sites) to form oxygen-containing C_3 intermediates at the anode surface, from which CO and CO_2 were subsequently derived. At temperatures of about 250ºC, the Pt surface poisoning was also prevented, such that Pt-CO sites are cleaned up due to the reaction of *CO with *OH on the adjacent Pt-OH sites, once again leading to CO and CO_2 production.

Berthelot et al [9] used different catalysts for the anodic oxidation of methane in a direct methane fuel cell. They used cyclic voltammetry and measurements of stationary U-I curves (potential-current) to evaluate the electrochemical characteristics of PEMFC (with methane directly fed to the anode i.e. DMFC). They also were able to detect reaction products close to the surface of the anode using *in situ* electrochemical-FTIR techniques and identify the adsorbed species and the partially or completely oxidized species using signal-averaging techniques. They found that when supported Pt was used as the anode the only product that was identified was CO_2, as opposed to using Pt-Ru anode where along with CO_2 other oxidized byproducts C3OH, HCHO and HCOOH were identified in the product stream [9].

These results are consistent with the findings in our study of Ni selectivity with respect to desired and undesired byproducts in the propane electro-oxidation process presented in Chapter 5. Our DFT calculated activation energies for the dehydrogenation of an adsorbed allyl radical were compared with those for propanol gas production. The adsorbed allyl radical (a desired byproduct that remains on the surface and can react to produce CO_2 as the predominant product of propane complete oxidation) was more likely to be produced than the undesired propanol gas byproduct which does not participate in propane oxidation process any further.

9.4 Bifunctionality of Alloy Electro-catalysts

There is extensive literature on bifunctionality of alloy catalysts where each component enhances a partial intermediate or full reaction on its surface, thereby improving the overall electrocatalytic reaction in different fuel cells. Topics of investigations done in this context include: an anode material for low temperature fuel cells [11], carbon poisoning of cathode electro-catalyst alloys in SOFCs [12], the effect of the electro-catalyst on the oxygen reduction reaction [13-14], an anodic methanol electro-oxidation reaction on clusters of 2^{nd} and 3^{rd} row group VIII transition metals and Pt-Ru alloys [15], a kinetic study of methanol oxidation on PtRu [16], and an impedance study of rate determining step for methanol oxidation on Pt and PtRu on high surface area carbon support [17]. The results of three latter studies are briefly discussed below.

Kua & Goddard [15] used DFT calculations (with a BLYP functional) to study the behavior of a number of transition metals including Pt, Ru, and Pt-Ru alloy as the anode

catalyst in direct methanol fuel cells. Their results showed that Pt was the best catalyst among single-metal catalysts for methanol oxidation, but it had a very poor CO tolerance which resulted in poisoning of the surface. They regarded the *Co on Pt as a thermodynamic sink. With respect to water dissociation Pt and Ru produced opposite results, where Pt exhibited the largest barrier height and Ru the smallest. On the other hand Pt-Ru caused a much faster methanol oxidation compared to Pt and Ru. This was due to the bifuctionality of this catalyst, where Pt is responsible for methanol dehydrogenation and Ru for water dissociation. In addition the *OH radical on Ru sites react with *CO on Pt sites to form CO2, thereby cleaning the Pt reaction sites, and preventing the occurrence of a thermodynamic sink [15].

In their kinetic study of a PtRu/C alloy as the anode of a DMFC, Gojković et al confirmed the bifunctionality of this alloy catalyst. Their investigation of PtRu/C was done based on XRD and cyclic voltammetry, and formal kinetic analysis. Their cyclic voltammetry of PtRu/C related the amount of Ru in the sample to its ability to absorb OH. The presence of both metals in the alloy and their fcc crystal structure was confirmed by their XRD analysis. They found kinetic parameters for methanol electro-oxidation that proved that the reaction follows bifunctional mechanism. On the same basis the formation of methanol residues adsorbed on Pt sites and OH radicals adsorbed on Ru sites were suggested as the rate determining steps [16].

Azevedo et al. [17] also studied methanol oxidation on Pt/C and PtRu/C as anodes of DMFC using cyclic voltammetry and electrochemical impedance spectroscopy. They

determined the behavior of the electrocatalysts by comparing the oxidation currents at different regions of potential and rate constants for the rate determining step. Through a Langmuir-Hinshelwood type mechanism analysis, they found that the rate limiting step is the reaction between *CO (on Ru) and *OH (on Ru or Pt). At potentials below 0.6V, according to the bifunctional mechanism Pt-Ru/C exhibited a better performance compared to Pt/C with respect to the rate limiting reaction step. Above this potential both catalysts were shown to be effective for methanol oxidations [17].

Our findings for propane electro-oxidation (in the presence of water vapor) on Ni-Fe alloy catalysts presented in chapter 6 are consistent with the findings on Pt-Ru catalysts for methanol electro-oxidation at the anode of DMFCs. Our NiFe alloys behaved in the same manner for both water dissociation and propane dehydrogenation reactions as PtRu did for water dissociation and reactions at the anode of DMFCs. Like Ru, Fe promoted the water dissociation reaction, and Ni promoted the propane dehydrogenation reaction as Pt did for methanol dehydrogenation. This very similar behavior was expected and can be justified since Fe is in the same group as Ru and Ni is in the same group as Pt.

9.5 SIESTA and the Basis Sets it Uses

The SIESTA software that was used as a tool to perform the DFT calculations in this work uses atom-centered (localized) numerical basis functions (a thorough description of localized and non-localized is provided section 2.2.3.). These are localized finite-support atomic basis functions that are composed of a spherical harmonic and a radial function that becomes zero beyond a radius r_c. The DFT method used in SIESTA is a self-

consistent method that uses standard norm-conserving atomic orbital basis set that includes multiple- ζ and polarization orbitals. The basis function and the electron density are projected on a real-space grid in order to calculate Hartree and exchange correlation potentials and matrix elements with a number of operations that scales linearly with the size of the system. A modified energy functional is used in SIESTA whose minimization produces orthogonal wave functions and the same energy and density as the Kohn-Sham energy functional, without the need for explicit orthagonalization. Using localized electron wave functions allows the computation time and memory required to minimize the energy also scale linearly with the size of the system [18-21].

Based on the system used and the user's choice, basis sets from a minimal single- ζ, (SZ) appropriate for semiquantative simulation, to higher- ζ plus polarization for more complicated systems can be used. SIESTA uses the double- ζ plus polarization (DZP) as the "standard" basis (the default used by SIESTA), because it usually represents a good balance between well converged results and a reasonable computational cost. Variationally optimized highly efficient basis sets (more efficient than SZ and DZP) were obtained by Soler et al. [21].

In one of their studies on the SIESTA method, Soler et al. [21] presented their energy calculation results for silicon as the basis for their comparison of a PW DFT method using non-localized basis sets, and a SIESTA DFT method using localized atomic orbital (LCAO) basis sets. They showed that SZ bases are comparable to PW (bases) with cutoffs that are typically used in molecular dynamic simulations, while DZP sets are

comparable to PW (bases) with cutoffs used in geometry relaxations and energy comparisons. Furthermore they showed that in terms of the number of basis orbitals, LCAO is more efficient than PW by a factor of 10-20 [21]. They stated that based on their findings, SIESTA is considerably faster than PW calculation of a similar quality [21].

9.6 C_3H_8/Me_{slab} Coordination Geometry Selected

In this research all the systems were coordinated by placing the central carbon of propane on a Ni atom in the surface of the slab as the reaction site. The Ni reaction site was chosen such that it was not on the edge of the surface to prevent propane from hanging into (or spill over to) the adjacent cell. The selection of the propane central carbon as the reacting site on propane was based on the stability of the propyl radicals. The order for alkyl radical stability is $1^o < 2^o < 3^o$ [22]. The 2-propyl radical (2^o radical, R-C$^{\bullet}$-R) is a more stable radical than a 1-propyl radical (1^o radical) [22]. More energy (420 kJ/mol) is required to dehydrogenate propane from either of its end carbons (to produce a hydrogen radical and a 1-propyl radical) than from its central carbon atom (413 kJ/mol, to make a hydrogen radical and a 2-propyl radical). The 1-propyl radical to has a higher energy and hence is less stable than the 2-propyl radical [22].

Initially the central carbon atom of propane was selected for placement on the Ni reaction site. Then the system was defined using a z-matrix input format (details in section 2.3.2, p. 46) based on bond distances, bond angles and dihedrals angles for propane adsorbed on the metal slab surface and a set of fractionals for the metal atoms in

the slab. All the coordinates in the system then were allowed to relax for our adsorption energy studies and all but one of the coordinates were allowed to relax for the activation energy calculations (described in section 5.2, p. 106). The system then was optimized by the program to have the minimum total energy (with a convergence criterion of 10^{-3} eV). It was clear that this optimization was done very systematically and carefully by the program, since the geometries for propane on a 3-fold symmetry surface (propane/Co_{slab}) was evidently different than that of propane on a 4-fold symmetry surface (propane/Ni_{slab}).

9.7 Spin Polarization

Spin polarized calculations were performed for propane adsorption on Ni to examine the effect on the adsorption energy. The total system energies for the two spin-polarized systems of Ni slab and propane/Ni_{slab} (propane adsorbed on Ni slab) were calculated. The adsorption energy for a spin-polarized Propane/Ni_{slab} was -0.509 eV which is lower than our original Eads for propane/Ni_{slab} (of the spin-unpolarized system) by 0.036 eV (3.47 kJ/mol). This variation is well within the target accuracy of 0.1 eV for DFT calculations on transition metals [23]. Because this difference is small it can be concluded that the observed trend in Fig. 4.3 (volcano plot) is qualitatively correct, if the difference stays within the same range for the other 3d transition metals studied in Chapter 4.

9.8 True Transition (TS) State Energy versus TS Energies in this Work

The true transition state structure scan be determined by searching for the first-order saddle point (a point which is both stationary and a point of inflection (not a local

extremum)) on the potential energy surface. Finding such saddle point requires vibrational frequency calculations using quantum mechanical methods. This calculation was not performed for any of the systems studied in this research. However, in order to find the transition state energies in this work we used the fixed bond length method (described in section 5.2, p. 106). The transition states energies obtained are an upper bound to the true saddle point transition states as shown in Figure 9.1.

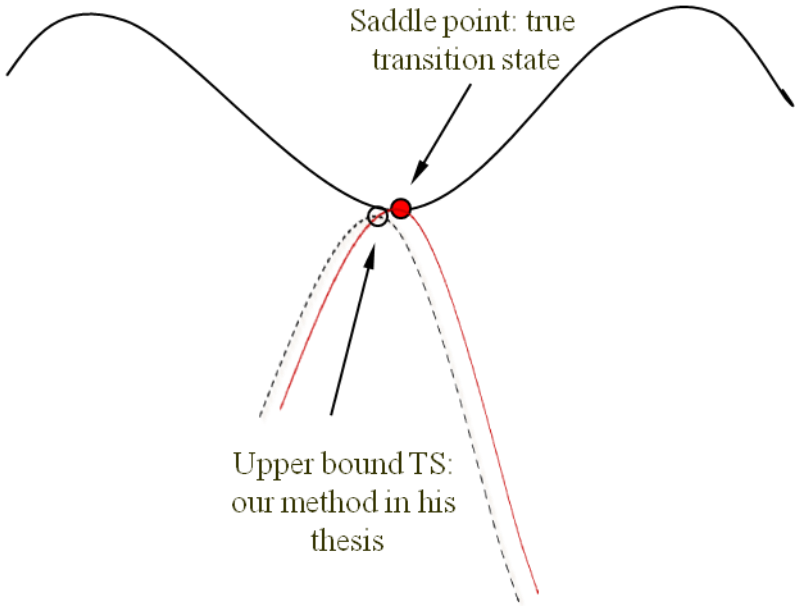

Figure 9.1: Saddle point transition state compared to an upper bound transition state

9.9 Validation of the Generated Ni Pseudopotentail by Comparing LC-based Energetics

The pseudopotentials in this work were custom generated, using a method in the ATOM program of SIESTA (see section 2.3.1, P. 36). The method uses an improved Troullier-Martins (tm2) generation scheme [24], and a PBE (Perdew, Burke and

Ernzerhof [25]) functional (see section 2.3.1, P. 36 for more details). To confirm the validity of our pseudopotential generation method and our generated pseudopotentials, energy calculations were performed for a single Ni unit cell using various lattice constants and our custom generated Ni pseudopotential. The lattice constant (LC) that resulted in the minimum total energy for the unit cell was 0.370 nm (Fig. 9.2) that results in an error of 4.87% when compared to the experimental LC for Ni (0.352) measured by XRD [26]. This error is smaller than the 6% error that is reported for the PBE functional by Perdew et al. [27].

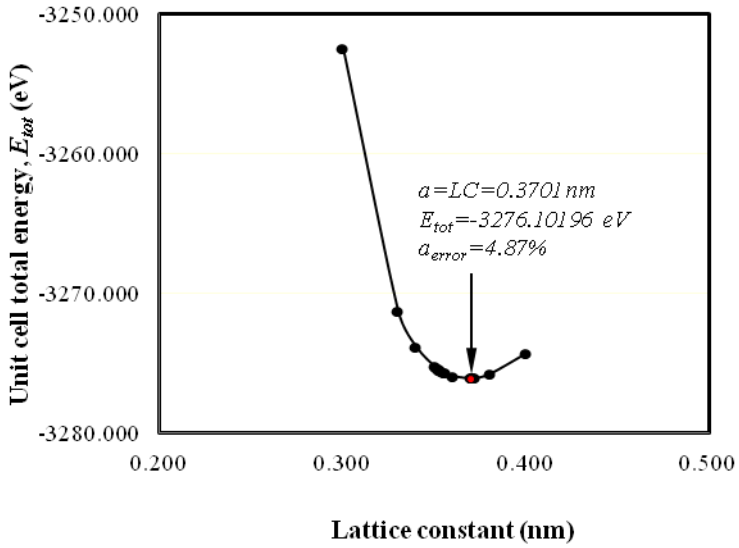

Figure 9.2: Plot of unit cell total energy, -E_{tot} (eV) versus lattice constant (nm)

9.10 Global-minimum E_{ads}: Surface Scan Energy Calculations

A set of adsorption energies for propane on the surface of an arbitrary ordered NiFe slab with 4 Fe atoms in the top layer and 4 Fe atom in the bottom layer (22%Fe), were calculated by changing the Ni reaction site for propane on the surface. Fig. 9.3a shows the picture of propane adsorbed on the $Ni_{1rxn\text{-}site}$ reaction site. In this picture in addition to

the surface Fe atoms, the Fe atoms in the bottom layer can be seen as well. The $Ni_{1rxn\text{-}site}$ is the reaction site chosen for all of the calculations in this research. Fig. 9.3b presents a drawing of the surface layer showing the various Ni sites where propane was placed during the surface energy scan process. Table 9.1 provides the adsorption energies for propane on each Ni shown in Fig. 9.3b. In Fig. 9.3 the yellow atoms represent Ni atoms and the green atoms represent Fe atoms. The Ni atoms on the edge were not considered as reaction sites in our surface energy scan, since if propane was placed on any of these atoms it will hang (spill) into the adjacent cell. There is at least one Fe atom adjacent to the Ni reaction site in each case.

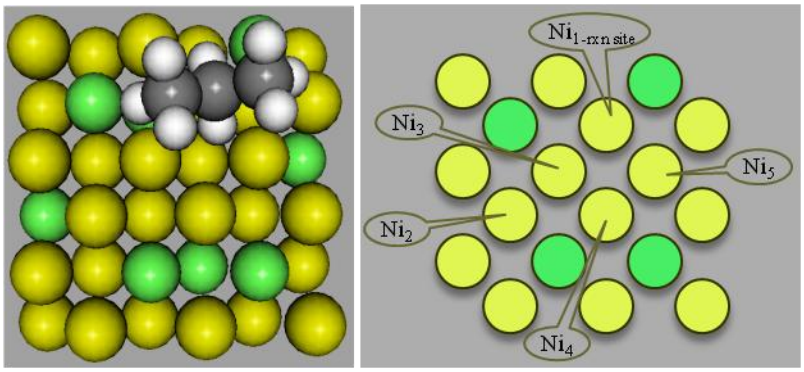

(a) (b)

Figure 9.3: (a) The optimized structure of propane adsorbed on the surface of an arbitrarily ordered NiFe alloy slab with 4 Fe atoms in the surface and 4 Fe atoms in bottom layers (total of 8 Fe atoms, 22% Fe slab)

Table 9.1: Surface energy scan results, where each $Ni_{i(i=1\text{-}5)}$ represents the site on which propane was placed in order to obtain the corresponding adsorption energy (E_{ads})

Reaction site	Ni_1	Ni_2	Ni_3	Ni_4	Ni_5
$-E_{ads}$ (eV)	0.547	0.472	0.523	0.516	0.571

Evidently the adsorption energies differ based on the Ni site on which propane is pla-

ced. The presence of additional (to the surface adjacent Fe atoms) Fe atoms close to the reaction site in the bottom surface seems to have an effect on the adsorption energies. The purpose of these additional calculations was to obtain global minimum adsorption energy by examining all the possible Ni reaction sites. This minimum adsorption energy, -0.472 eV corresponds to propane adsorbed on Ni_2 reaction site.

9.11 References

[1] Cairns, E. J.: *Adv. Electrochem. Electrochem. Eng.* **1971**, *8,* 337-392Gross, M.D.; Vohs, J.M.; Gorte, R.J. *J. Mater. Chem.* **2007**, *17,* 3071-3077

[2] Bockris, J. O.; Srinivasan, S. *Fuel Cells: Their Electrochemistry* McGraw-Hill: New York, **1969**

[3] Savadogo, O.; Rodriguez-Varela, F.J. *J. New Mater. Electrochem. Sys.* **2001,** *4*, 93-97

[4] Cheng, C.K.; Luo, J.L.; Chuang, K.T.; Sanger, A.R. *J. Phys. Chem. B,* **2005**, *109*, 13036-13042

[5] Rodriguez-Varela, F.J.; Savadogo, O. *J. New Mater. Electrochem. Sys.* **2006,** *9*, 127-137

[6] Nykänen, L.; Honkala, K.; *J. Phys. Chem. C*, **2011**, *115,* 9576-9586

[7] Wroblowa, H.; Peirsma, B.J.; Bockris, J.O'M. *J. Electroanal. Chem.* **1963**, 6, 401-416

[8] Grubb, W.T.; Michalske, C.J. *J. Electrochem. Soc.* **1964**, *111*, 1015 – 1019

[9] Bertholet, S.; Gehain, E.; Hahn, F.; Leger, J. M.; Srinivasan, S.; Lamy, C. *Electrooxidation of Methane: PEMFC and in situ Electrochemical*

Spectroscopic Studies, Abstracts, *194th Mtg, Electrochem. Soc.* Boston, Nov. **1998**, *98-2*, Abstract No. 1D90

[10] Rodriguez Varela, F.J.; Savadogo, O. *J. Electrochem. Soc.* **2005**, *152*, A1755-A1762

[11] Christoffersen, E., Liu, P., Ruban, A., Skriver, H. L., and J. K. Nørskov, J. K.; *Journal of Catalysis*, **2001**, *199*, 123-131

[12] Nikolla, E., Schwank, J., Linic, S.; *Journal of Catalysis*, **2007**, *250*, 85-93

[13] Vukmirovic, M. B., Zhang, J., Sasaki, K., A.U. Nilekar, A. U., Uribe, F., Mavrikakis, M., Adzic, R. R.; *Electrochimica Acta*, **2007**, *52*, 2257-2263

[14] Nørskov,J. K., Rossmeisl, J., Logadottir, A., Lindqvist, L., Kitchin, J. R., Bligaard, T., Jonsson, H.; *J. Phys. Chem. B.*, **2004**, *108*, 17886-17892

[15] Kua, J., Goddard III, W. A.; *J.` Am. Chem. Soc.*, **1999**, *121*, 10928-10941

[16] Gojković, S. Lj.; Vidaković, T. R.; Đurović, D. R.; *Electrochemica Acta*, **2003**, *48*, 3607-3614

[17] Azevedo, D. C.; Lizcano-Valbuena, W. H.; Gonzalez, E. R.; *J New Mat. Electroc. Sys*., **2004**, *7*, 191-196

[18] Ordejon,P., Sanchez-Portal, D., Garcia, A., Artacho, E., Junquera, J., Soler, J. M; *Riken Review* **2000**, *29*, 42

[19] Junquera, J., Paz, O., Sanchez-Portal, D., Artacho, A.; *Physical Review B* **2001**, *64*, 235111

[20] Artacho, E., Gale, J. D., Garcia, A., Junquera, J., Martin, R. M., Ordejon, P., Sanchez-Portal, D., Soler, J. M.; *SIESTA 2.0.2*, Fundacion General University, Madrid, **2008** (http://www.uam.es/siesta)

[21] Soler, J. M., Artacho, E., Gale, J. D., Garcia, A., Junquera, J., Ordejon, P., Sanchez-Portal, D.; *J. Phys.: Cond. Matt.* **2002**, *14*, 2745

[22] Mehta, B.; Mehta, M.; *Organic Chemistry, Eastern Economy Edirion*, Prentice-Hall of India Pvt.Ltd, **2005**

[23] Koch, W.; Holthausen, M.C. *A Chemist's Guide to Density Functional Theory, 2nd ed.,* Wiley-VCH: Weinham, **2001**

[24] Troullier, N.; Martins, J. L.; *Phys. Rev. B* **1991**, *43*, 1993

[25] Perdew, J. M.; Burke, K. Ernzerhof, M. *Phys. Rev. Lett*. **1996**, *77*, 3865-3868

[26] Haynes, W. M. *CRC Handbook of Chemistry and Physics*, 91st ed.: CRC Press: **2010**

[27] Perdew J. P.; Ruzsinszky, A.; Csonka, G. I.; Vydrov, O. A.; Scuseria, G. E.; Constantin,, L. A.; Zhou, X.; Burke, K.; *Phys. Rev. Lett.* **2008**, *100*,136406

Appendix

Appendix A: Bagotzky-like Mechanism for Propane Electro-Oxidation at the Anode of DPFC